Spectroscopic Investigation of Chlorophyll Model Systems in a Myoglobin Matrix

Inaugural-Dissertation
zur
Erlangung des Doktorgrades der
Mathematisch-Naturwissenschaftlichen Fakultät
der Heinrich-Heine-Universität Düsseldorf

vorgelegt von
Prasanna Venkatesh Rangadurai
aus Chennai (Madras), India

Düsseldorf, November 2011

Aus dem Max-Planck-Institut für Bioanorganische Chemie,
Mülheim an der Ruhr

Gedruckt mit der Genehmigung der Mathematisch-Naturwissenschaftlichen
Fakultät der Heinrich-Heine-Universität Düsseldorf

Referent: Prof. Dr. Wolfgang Lubitz
Koreferent: Prof. Dr. Rainer Weinkauf
Tag der mündlichen Prüfung: 17.11.2011

In each century since the beginning of the world wonderful things have been discovered. In the last century more amazing things were found out than in any century before. In this century hundreds of things still more astounding will be brought to light. At first people refuse to believe that a strange new thing can be done, then they begin to hope it can be done, then they see that it is done- then it is done and the entire world wonders why it was not done centuries ago. One of the new things people began to find out in the last century was thoughts-just mere thoughts-are as powerful as electric batteries - as good for one as sunlight is, or as bad for one as a poison. To let a sad thought or a bad one get into your mind is as dangerous as letting a scarlet fever germ get into your body.

■ The secret garden

Acknowledgements

For providing me with a wonderful opportunity and a challenging project, I would like to thanks Prof. Wolfgang Lubitz. His constant encouragement and scientific support were most valuable.

I would like to thank Dr. Maurice van Gastel for introducing me to the triplets, EPR and DFT calculations and taking me through these years. He has been a great source of knowledge and support.

For introducing me to crystallography and for the invaluable single crystal data, I thank Dr. Hideaki Ogata.

Furthermore, Dr. Alexey Silakov, Dr. Maria-Eirini Pandelia and Dr. Jens Niklas have been real pillars of support and borne my doubts at crucial times. Dr. Alexey Silakov is most thanked for his support with the single crystal EPR measurements and simulations.

Dr. Anton Savitsky is much thanked for his help with the W band measurements of the single crystals and Dr. Olaf Rüdiger is especially thanked for the electrochemical experiments on reconstituted myoglobin.

Dr. Markus Knipp, Dr. Alexander Marchanka, Dr. Shipra Prakash, Dr. Özlen Erdem, Dr. Leysan Khuzeeva and Dr. Kasim Ocakoglu are thanked for their various discussions and support.

No experimental work can be easy without technical support. I would like to thank Gudrun Klihm, Frank Reikowski, Christoph Laurich, Michael Reus and Horst Selbach for their support during my EPR measurements, electrochemistry, synthesis and HPLC.

Last but not the least I would like to thank my family and friends for their unconditional support and encouragement.

Abstract

Photosynthesis is one of the oldest reactions occurring in nature and much work has been done to understand the process in detail. Studies have been carried out on the system as a whole and also the various components like the photosystem I, photosystem II, cytrochromes, antenna pigments and chlorophylls have been analyzed individually to understand their function. Since the processes are light induced and generate unpaired electrons, EPR spectroscopy has been one of the main tools of analysis. Previously, EPR and ENDOR have been utilized to study the electronic structure of the photosystems and the chlorophyll a molecule.

The triplet formation in the photosystems is carefully avoided since the triplets lead to production of singlet oxygen which can prove fatal to the photosynthetic membrane. Hence, any triplets formed are immediately quenched by the carotenoids present in the system. However, the triplet state contains all the necessary electronic information of the frontier orbitals and will help in better understanding of the electron transfer processes. Since the triplets are quenched in the native system, it becomes essential to isolate the individual components and study them.

In this work, four model systems were synthesised in order to understand their triplet electronic configuration and compared with the native systems. The four model systems were further inserted into a myoglobin matrix to study the influence of a surrounding protein environment. EPR and ENDOR experiments have been carried out on the model systems in and outside myoglobin. DFT calculations have been employed to support the experimental data. The native myoglobin contains a heme cofactor which can be easily replaced by the structurally similar model systems. Myoglobin from various sources has been utilized to make reconstituted myoglobin and pilot single crystal EPR measurements have been performed on Zinc protoporphyrin IX-Mb single crystals in an attempt to study the orientation of the zero field splitting tensors.

Zusammenfassung

Die Photosynthese ist eine der ältesten Reaktionen in der Natur und als solche ist sie schon lange Gegenstand der Forschung, mit dem Ziel, diesen Prozess im Detail nachvollziehen zu können. Untersuchungen sowohl des photosynthetischen Apparates als Ganzes, als auch der verschiedenen daran beteiligten Komponenten wie Photosystem I, Photosystem II, Cytochrome, Antennenpigmente und Chlorophyllmoleküle wurden durchgeführt, um ihre jeweilige Funktion zu verstehen. Da bei den lichtinduzierten Prozessen ungepaarte Elektronen entstehen, ist die EPR-Spektroskopie dabei eine der bevorzugten Untersuchungsmethoden. So wurden EPR und ENDOR verwendet, um die elektronische Struktur von Komponenten der Photosysteme und von Chlorophyll a zu charakterisieren.

Reaktionen innerhalb der Photosysteme, die zur Bildung von Triplettzuständen führen, werden minimiert, da diese Singulett-Sauerstoffmoleküle erzeugen, die wiederum die photosynthetische Membran schädigen und letztendlich zerstören können. So werden Tripletts umgehend von Carotinoiden des Reaktionszentrums gequenched. Der Triplettzustand enthält jedoch alle charakteristischen Informationen der Grenzorbitale und kann dadurch einen wichtigen Beitrag zum besseren Verständnis der Eletronentransferprozesse leisten. Da die Tripletts im nativen System gequencht werden, ist die Isolierung der einzelnen Komponenten eine zwingende Voraussetzung für ihre Untersuchung.

In dieser Arbeit wurden vier Modellsysteme synthetisiert, um die Elektronenkonfiguration ihrer Triplettzustände zu verstehen, und mit den nativen Systemen verglichen. Des Weiteren wurden die vier Modellsysteme in eine Myoglobin-Matrix eingebracht, um den Einfluss einer Proteinumgebung auf sie zu studieren. EPR- und ENDOR-Experimente wurden mit den Modellsystemen sowohl außerhalb als auch innerhalb der Myoglobin-Umgebung durchgeführt. DFT-Rechungen wurden durchgeführt, um die Analyse der experimentellen Daten zu unterstützen. Natives Myoglobin enthält einen Häm-Kofaktor, der durch die strukturell ähnlichen Modellsysteme ersetzt werden kann. Myoglobin von verschiedenen Organismen wurde verwendet, um das so rekonstituierte Protein herzustellen. Erste Einzelkristall-EPR-Messungen wurden mit Einzelkristallen von Zink-Protoporphyrin IX-Mb durchgeführt

als Versuch, die räumliche Orientierung des Tensors der Nullfeldaufspaltung zu bestimmen.

TABLE OF CONTENTS

CHAPTER 3: INTRODUCTION TO ELECTRON PARAMAGNETIC RESONANCE

CHAPTER 4: CRYSTALLIZATION

LIST OF ABBREVIATIONS

A,Ai	- Hyperfine tensor, principal values
Aiso	- Isotropic hyperfine value
ApoMb	- Apo myoglobin
B_0,B_1	- Static external magnetic field, microwave field
CD	- Circular dichroism
Chl a	- Chlorophyll a
CV	- Cyclic voltammogram
CW	- Continuous wave
D, E	- Zero field splitting parameters
DFT	- Density function theory
E/A	- Emission/absorption
ENDOR	- Electron nuclear double resonance
EPR	- Electron paramagnetic resonance
ET	- Electron transfer
FID	- Free induction decay
FSE	- Field swept echo
g, gi	- g-tensor, principal values
hfc	- Hyperfine coupling
HOMO	- Highest occupied molecular orbital
HPLC	- High performance liquid chromatography
ISC	- Intersystem crossing
LUMO	- Lowest unoccupied molecular orbital
MALDI	- Matrix assisted laser deionisation ionisation
Mb	- Myoglobin
NMR	- Nuclear paramagnetic resonance
PDB	- Protein data bank

PPIX	- Protoporphyrin IX
RP	- Radical pair
S_i	- Singlet sublevels
T_i	- Triplet sublevels
UV-Vis	- Ultra violet – Visible
X, Q, W	- EPR frequency bands
ZFS	- Zero field splitting
Zn	- Zinc

CHAPTER 1. INTRODUCTION

1.1 Introduction to photosynthesis

Photosynthesis is the process of converting light energy from the sun into chemical energy and it is the most important process of energy conversion found in nature. In simple words photosynthesis can be described as the process that converts carbon dioxide into organic compounds like sugar. Photosynthesis occurs in plants, algae and many types of bacteria and involves the utilization of CO_2 and H_2O for the production of sugar (carbohydrates) and O_2. There are also some species that perform photosynthesis without using water but by using reduced sulphur compounds or simple organic compounds as source of electrons. This is called the anaerobic photosynthesis. The oxygenic photosynthesis involves the production of molecular oxygen as a by-product and it is the single most important process that is responsible for the oxygenation of the atmosphere.

Photosynthesis can be represented with a simple equation,

$$6CO_2 + 12\ H_2O \rightarrow^{*} C_6H_{12}O_6 + 6O_2 + 6H_2O$$

* In the presence of sunlight

Organisms active in oxygenic photosynthesis possess two types of photosystems, called photosystem I and photosystem II (Figure 1.1). H_2O is used as the electron donor and molecular oxygen is generated as the by-product. Over billions of years oxygen has accumulated in the atmosphere, and thus provided a basis of all higher life on earth. The catalytic mechanisms of photosynthesis are numerous and complicated. The first step is the absorption of light by chlorophylls (Chls), followed by energy transfer to the reaction center (RC) and subsequent electron transfer. The energy of light is used for generation of an electrochemical potential across the photosynthetic membrane. Photosystem II (PS II) transfers the electrons from water to a quinone and evolves O_2. Photoystem I (PS I) creates reduced intermediates that are used for the production of nicotinamide adenine dinucleotide phosphate (NADPH).

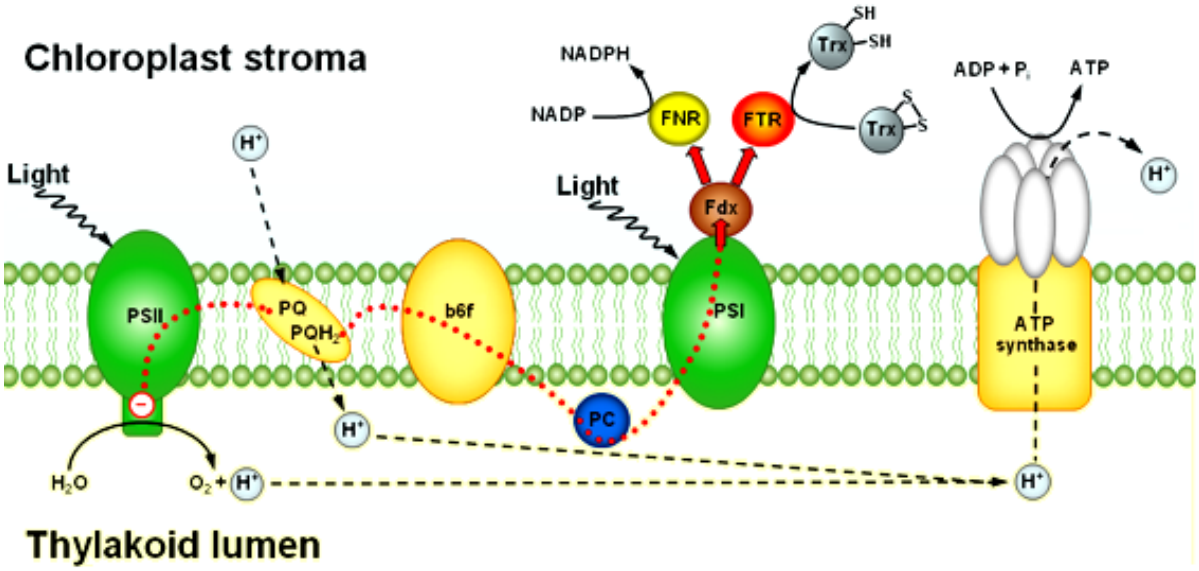

Figure 1.1 Light-dependent electron and proton transport in the thylakoid membrane and associated reactions. Electrons released in the oxidation of H_2O are transferred in the light through photosystem I (PSI), plastoquinone (PQ), the cytochrome b6f complex, plastocyanin (PC), and photosystem II to ferredoxin (Fdx). Reduced Fdx reduces either thioredoxins (Trx) via ferredoxin:thioredoxin reductase (FTR) or NADP via ferredoxin:NADP reductase (FNR). Protons released into the thylakoid lumen in the oxidation of H_2O and by PQ are used for the synthesis of ATP (Figure modified from Meyer et al., 2009)

The catalytic cycle is driven by light energy. Hence it is called the light reaction of photosynthesis and its main purpose is to provide protons and high energy electrons which are essential to create the ATP and NADPH. These molecules are further utilized in the light independent or the dark reaction of photosynthesis for fixation of CO_2.

1.1.1 The photosynthetic light reactions, PSII and PSI

The light reaction of photosynthesis begins with the absorption of light by chlorophyll and the accessory pigments. The accessory pigments are compounds that work in conjugation with chlorophyll a and help to absorb light and dissipate excess light energy. Chlorophyll b, c and d (chlorophyll c and d are found in certain algae) and carotenoids are examples of accessory pigments.

Photosystem II (PS II) is a multi subunit complex embedded in the thylakoid membranes of higher plants, algae and cyanobacteria. It uses light energy to catalyze a series of electron transfer reactions resulting in the splitting of water into molecular oxygen, protons and electrons.

The light energy used to drive the PS II reaction is captured by a large number of chlorophyll (Chl) a and b and carotenoid (β-carotene, lutein, neoxanthin and violoxanthin) molecules associated with light harvesting antenna proteins. Excitation energy is passed along an excitonically linked network of Chl molecules to P_{680}. The P_{680} is considered to be the reaction center in PS II and is named so because of its absorption maximum at 680 nm.

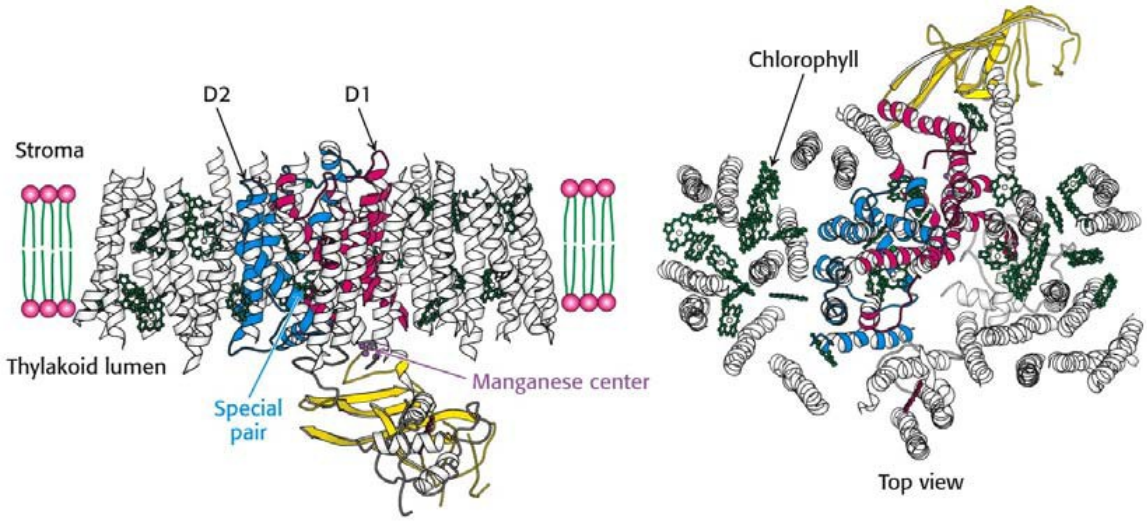

Figure 1.2 Representation of PS II

At the heart of PSII is the photochemically active reaction center (RC), which consists of the D1 and D2 proteins [1, 2, 3]. In higher plants and green algae well over 20 subunits are associated with PSII *in vivo* and have been identified. A detailed description can be found in references [4, 5, 6].

The two largest PSII subunits, the chlorophyll binding proteins, CP47 (PsbB) and CP43 (PsbC) are closely associated with the reaction center and form an antenna within the core complex. Their complete characterization can be found in references [7, 8]. One of the functions of CP47 is to transfer excitation energy from the Chl a/b binding proteins to the PS II reaction center, in the case of higher plants and green algae, and from phycobilisomes in the case of cyanobacteria and red algae [9, 10, 11, 12]. CP47 binds a number of cofactors including Chl a, β-Car and Lut, but does not bind Pheo or Chl b [13, 14]. CP47 has been estimated to contain 10-25 molecules of Chl a [13, 15, 16, 17]. The CP43 is also structurally similar to the CP47 and binds nearly 15 chlorophyll molecules [18, 19] and functions the same as CP47.

The structure of PS II from the cyanobacteria *Synechococcuc elongates* was first determined by Zouni [111] with a resolution of 3.8Å and later at higher resolutions by Kamiya [118], B.Loll [119] and Guskov [112]. PS II binds at least 99 cofactors – 35 chlorophyll a molecules, 12 β carotenoids, two pheophytins, three plastoquinones, two hemes, bicarbonate, 25 lipids, the $Mn_4Ca_1O_xCl_{1-2}(HCO_3)_y$ cluster, one Fe^{2+} and one putative Ca^{2+} ion per monomer [112].

The unique feature of PS II is the oxygen evolving complex (OEC), which contains four Mn ions (Mn4 cluster), one calcium ion and one chlorine ion as essential cofactors [113]. Water is the source of electrons for the OEC and it can exist in four oxidation states when excited by light. The electrons obtained in the PS II from the water oxidation are transferred to the PSI (Figure 1.1) via the cytochrome b6f and plastocyanin. This electron flow between the photosystems creates a transmembrane proton gradient which is used to generate ATP in the ATP synthase enzyme.

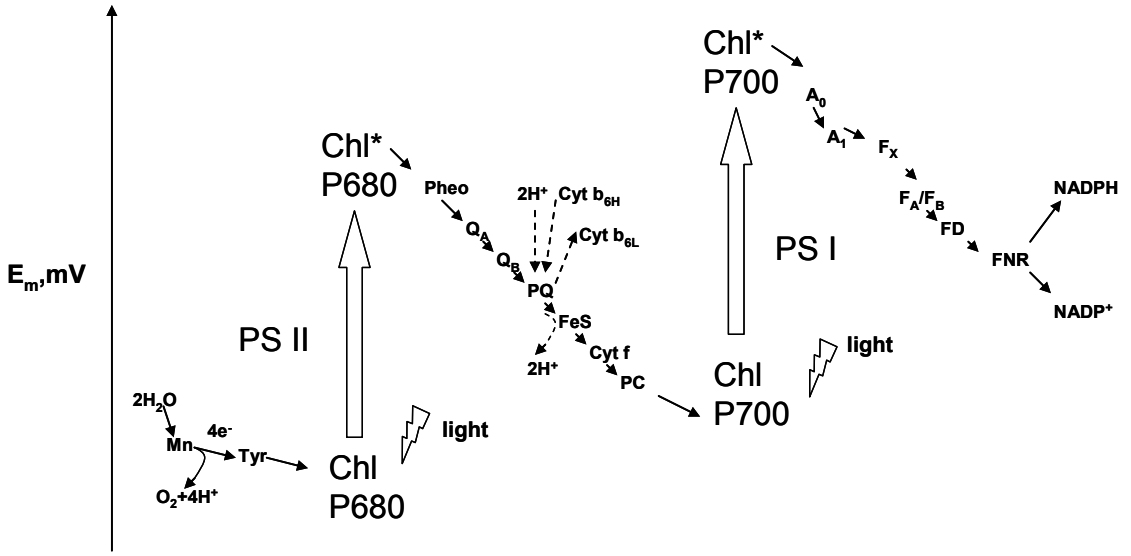

Figure 1.3 Representation of the Z-scheme in cyanobacterial organisms

In oxygenic photosynthetic organisms, the photosystem I (PSI) works in cooperation with the PS II (Z-scheme, Figure 1.3). PS I is a membrane bound protein that enables the light driven electron transfer from reduced plactocyanin to ferridoxin or flavodoxin [20].The PSI can exist as monomers or trimers. X ray structure at 2.5A [21] shows 12 protein subunits which contain 126 cofactors – 96 chlorophyll a molecules, 22 carotenoids, two phylloquinones (phQ), three iron sulfur clusters, four lipids, nearly 200 water molecules and probably a Ca^{2+} ion (see Figure 1.4).

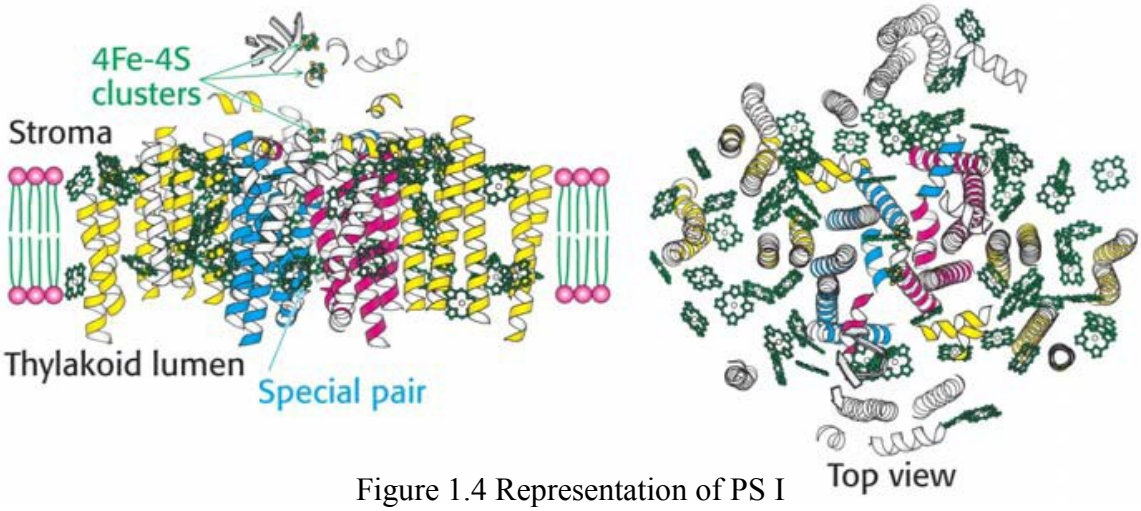

Figure 1.4 Representation of PS I

Two large subunits PsaA/PsaB bind 90 chlorophylls and 22 carotenoid molecules that function to absorb light. Light is absorbed by the chlorophyll molecules of the light harvesting complex (LHC) and the core antenna [22]. This energy is then transferred to the reaction center, P_{700} chlorophyll dimer [23, 24].The primary electron acceptor is A_0, a monomeric chlorophyll. After A_0, the electron is transferred to A_1, a phylloquinone, and subsequently to the three FeS clusters F_X, F_A, and F_B. From the terminal cluster F_B, the electron is transferred to ferredoxin, which subsequently leaves the docking site. After the cycle is complete, $P_{700}^{\bullet+}$ has to be reduced to allow a repetition of electron transfer. A docking site for the soluble electron carriers is located on the lumenal side close to P_{700}. Ferredoxin may also participate in the cyclic transportation of electrons back to the cytochrome b6 complex [25].

1.1.2 Antenna pigments in the photosynthetic reaction centers

The antenna pigments are responsible for absorption of light. The chlorophylls (Chl) are the most important amongst them. Pelletier and Caventou in 1818 were the fist to describe the green pigment in plants as chlorophylls. In 1906, Chl a and Chl b were separated by means of powdered sugar column chromatography [26] and later, bacteriochlorophylls were also identified [27].

Hans Fischer in 1940 elucidated the structure of Chl a. Chlorophylls are a part of the class of chemicals called porphyrins. They can be referred to as dihydroporphyrins (ring IV is partially saturated) having an unique cyclopentane ring (ring V). The structure of chlorophyll is shown in Figure 1.5 and it is a planar molecule containing a cyclic tetrapyrrole (porphyrin) “head” and a phytyl “tail”. The phytyl is a 20-C long straight chain alcohol containing a double bond. The central metal atom in the porphyrin ring of the chlorophylls is magnesium.

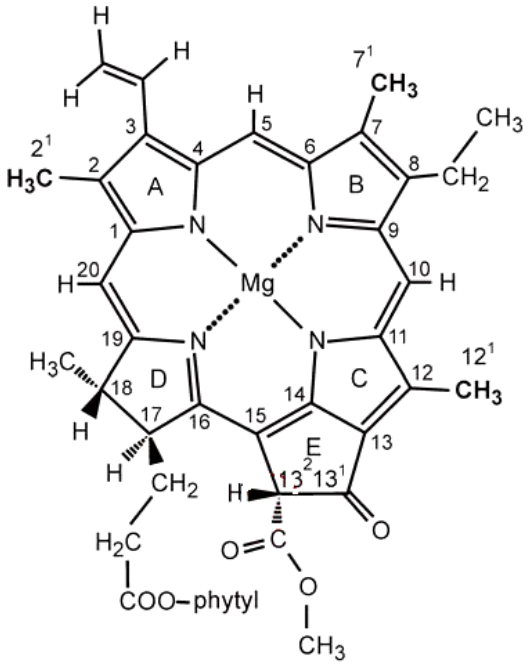

Figure 1.5 Structure of chlorophyll a

Each antenna pigment is capable of absorbing photons at characteristic wavelengths. The absorption spectra of the pigments correspond to the action spectrum of photosynthesis (Figure 1.6a). The chlorophylls absorb blue and red and carotenoids absorb blue-green light. Green and yellow are not effectively absorbed and hence this reflected light passes though the leaves giving rise to the green color of the leaves.

When the chlorophyll molecule absorbs light, its electronic structure is excited from the ground state S_0 (unexcited singlet) into an excited state S_n*. Depending on the wavelength of excitation, the system can occur in different excited singlet states (Figure 1.6b). The lifetime of the chlorophyll molecule in the excited singlet state is very short and the molecule returns to its original state S_0 via several pathways [28] that can be illustrated with a Jablonski diagram.

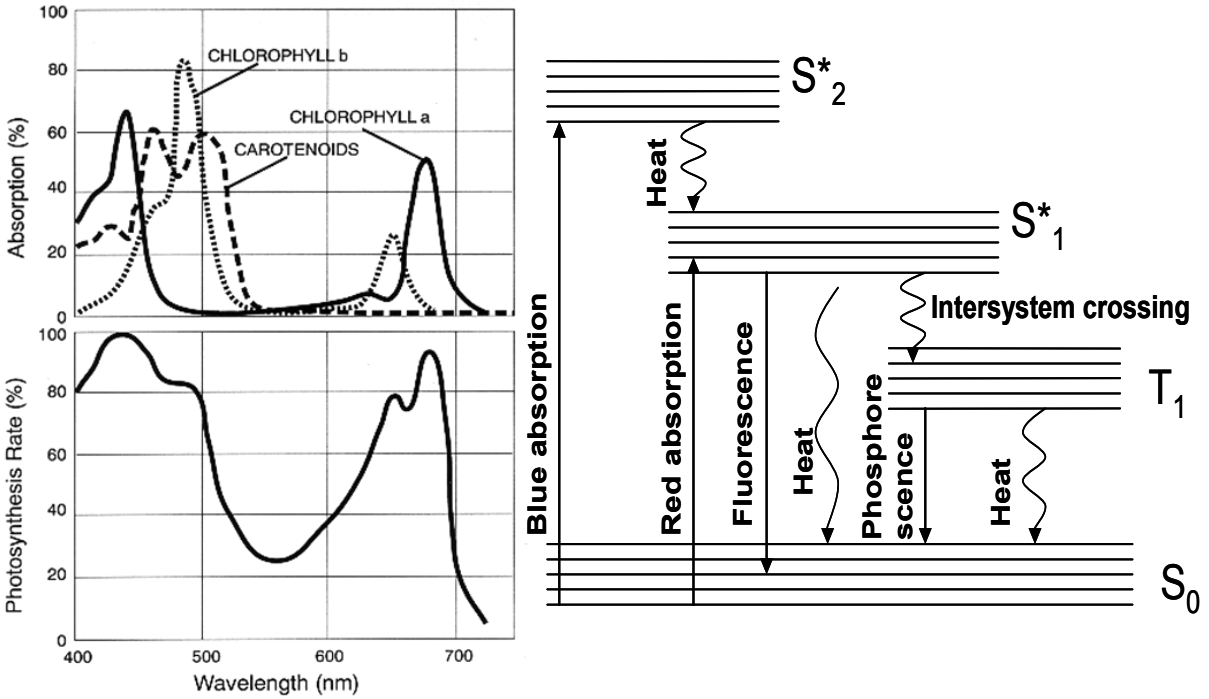

Figure 1.6 (a) Absorption spectra of various pigments and action spectrum of photosynthesis [28] (b) Jablonski diagram of excitation decay

The absorption spectrum of chlorophyll a is characterized by a strong Soret band at 430 nm and a relatively strong Qy band at 670 nm. The weak band at 580 nm is the Qx transition. The intense absorption in the visible region is important for the light harvesting functionality by Chl a and this is why it forms majority of the antenna complexes.

The carotenoids absorb blue light in the 450-570 nm range and they have two main functions: light harvesting and protection from photooxidation damage [29].The triplet state of chlorophyll is highly dangerous and is the major concern for photooxidation damage. The carotenoid molecules with their extensive π electron conjugation can take over the triplet state energy from the chlorophyll molecule, dissipate them as heat and thus prevent the formation of the destructive singlet oxygen [29].

$^1Car + {}^3Chl^* \rightarrow {}^3Car^* + {}^1Chl$ (triplet quenching)

$^3O_2 + {}^3Chl \rightarrow {}^1O_2 + {}^1Chl$ (singlet oxygen formation)

The carotenoids also protect the cell from damage by ultra violet radiation [30]. Because of their ability to quench oxygen radicals, the carotenoids are good anti oxidants and prevent the cell from oxidative breakage.

1.2 The Myoglobin

Myoglobin is a typical globular protein, and is found in many animal cells. Like hemoglobin, it combines reversibly with molecular oxygen; but whereas the role of hemoglobin is to transport oxygen in the blood stream, that of myoglobin is to store it temporarily within the cells (a function particularly important in diving animals such as whales, seals and penguins, the dark red tissues of which contain large amounts of myoglobin). Unlike the hemoglobin, the myoglobin contains only one iron porphyrin cofactor called the heme and consists of 153 amino acids. The molecular weight of myoglobin is 18,000 Daltons making it a small protein [31, 32].

The molecule consists of approximately 1200 atoms (excluding hydrogen). Nearly 70% of the main chain is folded into eight right handed alpha helices and the rest of the chain forms loops between the alpha helices devoid of symmetry. Four of the helices are terminated with a proline residue. The five membered ring of the proline residue does not fit within a straight stretch of the alpha helix and therefore disrupts the helix [33].

1.2.1 The structure of myoglobin

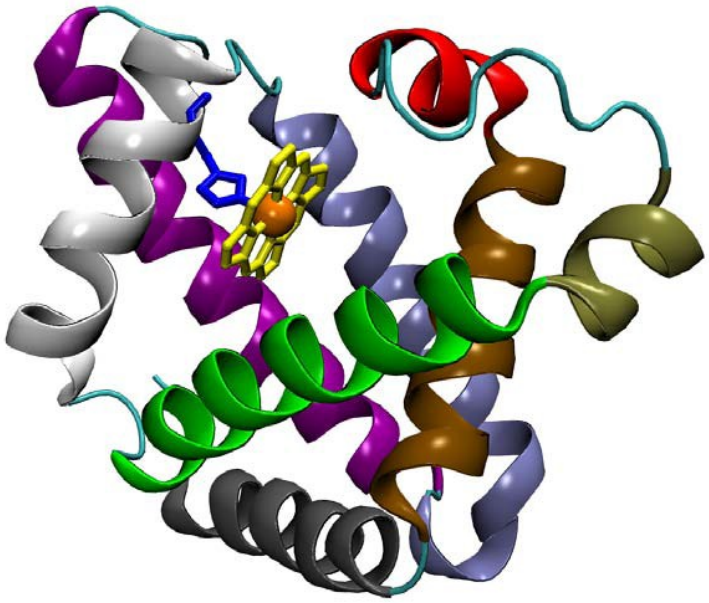

Figure 1.7 Structure of sperm whale myoglobin, [PDB: 1MBC]

Myoglobin is a water soluble globular protein comprising of 153 amino acids. The tertiary structure is composed of eight α-helices joined by short non-helical regions. Figure 1.7 is the structure of myoglobin from sperm whale (*Physeter catodon*).The helices are distinguished by color. The heme group is shown in licorice representation bound to the histidine. The heme iron, drawn as an orange van der Waals sphere, is the binding site for ligands, such as O_2, CO and NO.

The inside and outside surfaces of the protein are well defined. Almost every non-polar residue like leucine, valine, methionine and phenylalanine are present in the interior. The two histidines are the only polar residues found in the interior that play an integral role in the binding of oxygen to heme. The exterior contains polar residues like aspartate, glutamate, lysine and arginine along with some non polar residues [34].

The heme gives the capacity to myoglobin to bind to oxygen. It is a nonpolypeptide prosthetic group consisting of protoporphyrin and a central iron atom. The heme is also responsible for the characteristic crimson colour. The heme consists of an organic protoporphyrin and an iron. The protoporphyrin is made up of four pyrrole rings linked by methene bridges to form a tetrapyrrole ring and the iron atom in the centre binds to the four nitrogens. Iron can still bind to two more atoms in its fifth and sixth coordination positions. The heme is located in a crevice in myoglobin. The highly polar propionate side chains of the heme are on the surface of the molecule. At physiological pH, these carboxylic groups are ionised. The rest of the heme is inside the molecule, where is is surrounded by non polar residues except the two histidines. The iron atom of the heme is directly bonded to the proximal histidine residue which occupies the fifth coordination position. The iron atom is 0.3 Å out of the plane of porphyrin, on the same side where it is bonded to the proximal histidine. The oxygen binding site is at the sixth coordination. The second histidine residue, the distal histidine, is near the heme, but not bound to it [35].

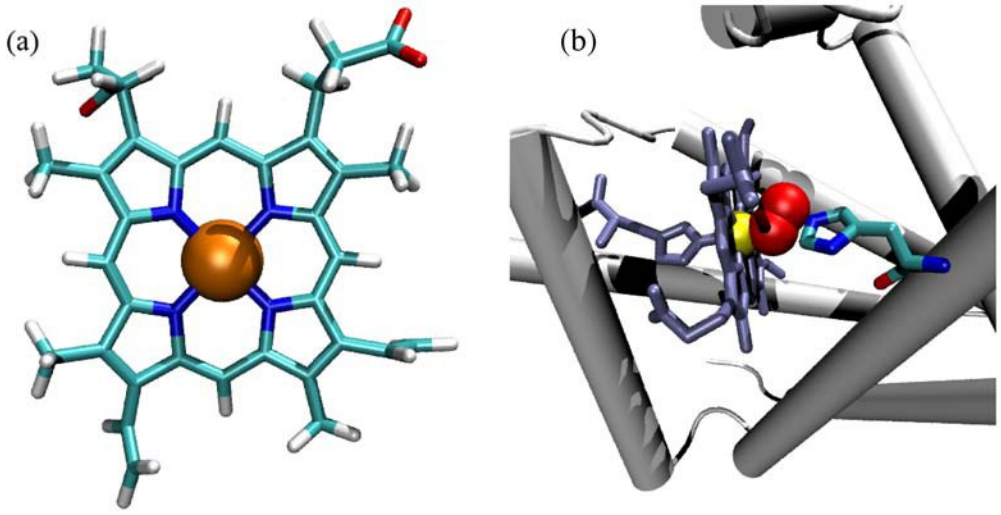

Figure 1.8 The heme group (a) and its binding environment in myoglobin (b). In (b), bound oxygen (O_2) is colored in red and the distal histidine, which influences the binding affinity, is shown colored by atom type; hydrogen atoms are not shown. The proximal histidine, which tethers the heme to the protein, is shown in the same shade of blue as the heme itself in (b).

1.2.2 Oxygen binding to heme

Figure 1.8(b) illustrates the binding of oxygen to the heme in the ligand cavity. The function of myoglobin is to serve as a temporary storage of oxygen and requires that the heme environment is conducive not only to binding of oxygen, but also doing it reversibly. For this, the myoglobin molecule serves a two-fold purpose of modulating the heme environment to facilitate oxygenation as well as ensuring that the heme iron remains in a ferrous state. Oxidized heme groups lose the ability to bind O_2. The oxidation goes through an intermediate in which O_2 is sandwiched between two hemes and a free heme gets readily oxidized in blood. The myoglobin structure prevents this oxidation by sterically preventing a heme-O_2-heme complex.

To protect the heme, the protein is densely packed. However, the protein must also allow the binding of oxygen to heme. Myoglobin does this by dynamically opening cavities close to O_2 and allowing O_2 to travel near the heme. The complete dynamics of oxygen binding to heme can be found in the following references [34, 36].

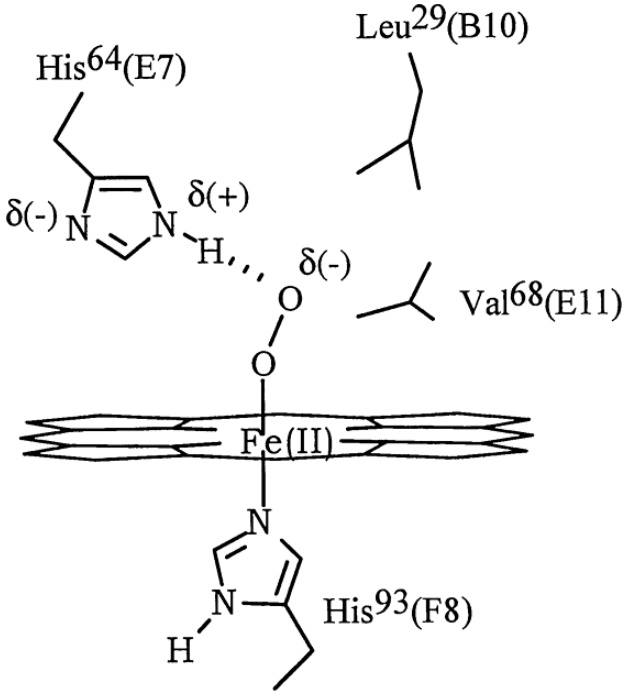

Figure 1.9 Representation of oxygen binding to Heme in myoglobin biding pocket [36].

1.3 Aim of this work

The aim of this work is to understand the orientation of ZFS tensors and the electron spin density distribution in the triplet state of chlorophyll model systems. Since the triplet states are paramagnetic, EPR spectroscopy has been the main tool to probe them [37, 38]. Standard EPR techniques often do not provide the necessary resolution required to understand the electronic structure. Pulsed EPR at 34 GHz and multiple resonance techniques like ENDOR have been employed to achieve a better understanding and resolution [39, 40].

The native photosynthetic system contains several subunits and cofactors and it is very difficult to selectively study the triplet state of chlorophyll. Previous work has been done on triplet states of reaction centres and chlorophyll a [41, 42, 43] and bacteriochlorophylls [44]. Instead, here, we have chosen to investigate the model systems, zinc protpporphyrin IX, zinc chlorophyllide, zinc pyrochlorophyllide and zinc chlorin e_6 and compare them with the native systems. This has also provided additional opportunity to study the influence of a protein matrix (in this case, myoglobin) on the ZFS parameters of the model systems. Single crystal EPR has been already studied on PS II systems [110]. It is not easy to crystallize the chlorophyll model systems in an organic solvent and doing so would also prove ineffective to study their electronic structure due to π stacking. Hence much focus has been on crystallization of reconstituted myoglobin in order to perform single crystal EPR and ENDOR experiments.

The interpretation of EPR data is not always straightforward. In order to get a complete picture of the systems investigated, we have extended the study using theoretical methods such as density function theory.

1.4 The model systems

Zinc protoporphyrin IX, zinc chlorophyllide, zinc pyrochlorophyllide and zinc chlorin e_6 are the model systems under investigation in this thesis. All the four cofactors are structurally similar to the porphyrin of chlorophyll and the native heme present in myoglobin. The cofactors do not posses the phytyl chain that is present in the chlorophyll. The removal of the phytyl enables the cofactors to replace the heme from myoglobin.

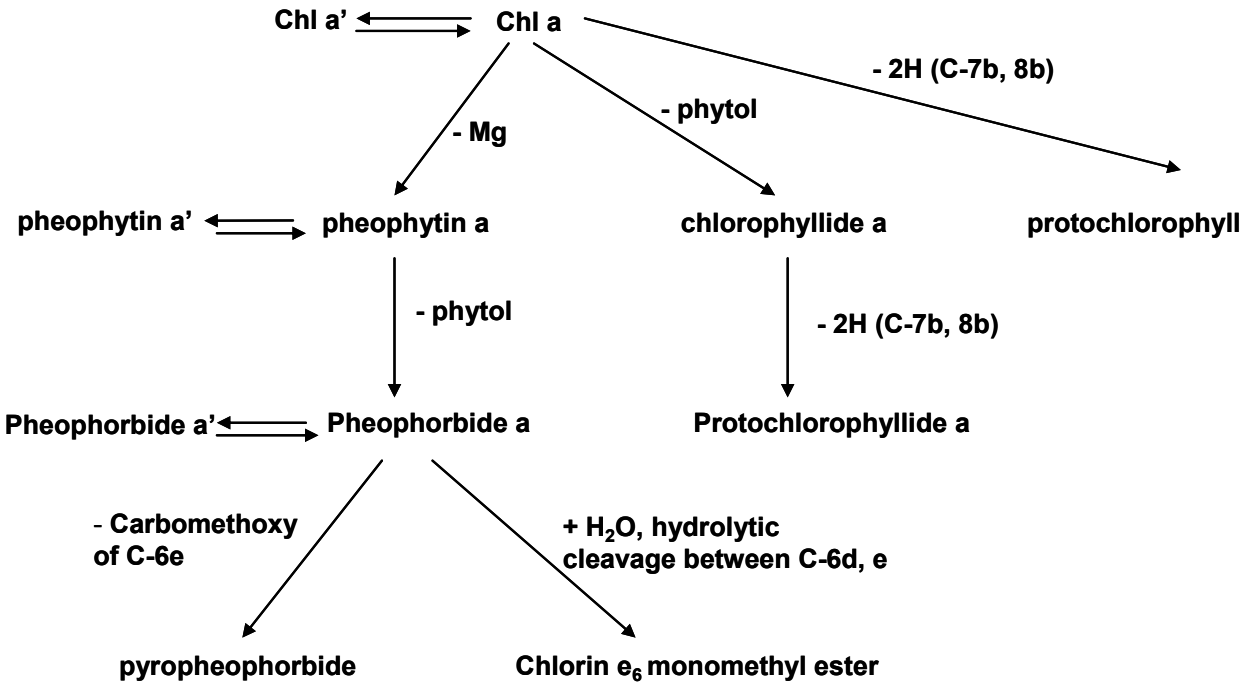

Figure 1.10. Formation of chlorophyll derivatives [*The chlorophylls, 45*].

Figure 1.10 represents the formation and nomenclature of the chlorophyll derivatives. In recent times, the nomenclature has been revised to avoid confusion. The term pheophorbide has been replaced by chlorophyllide and the name of the central metal is mentioned before the derivative, e.g. – zinc chlorophyllide contains the central metal zinc.

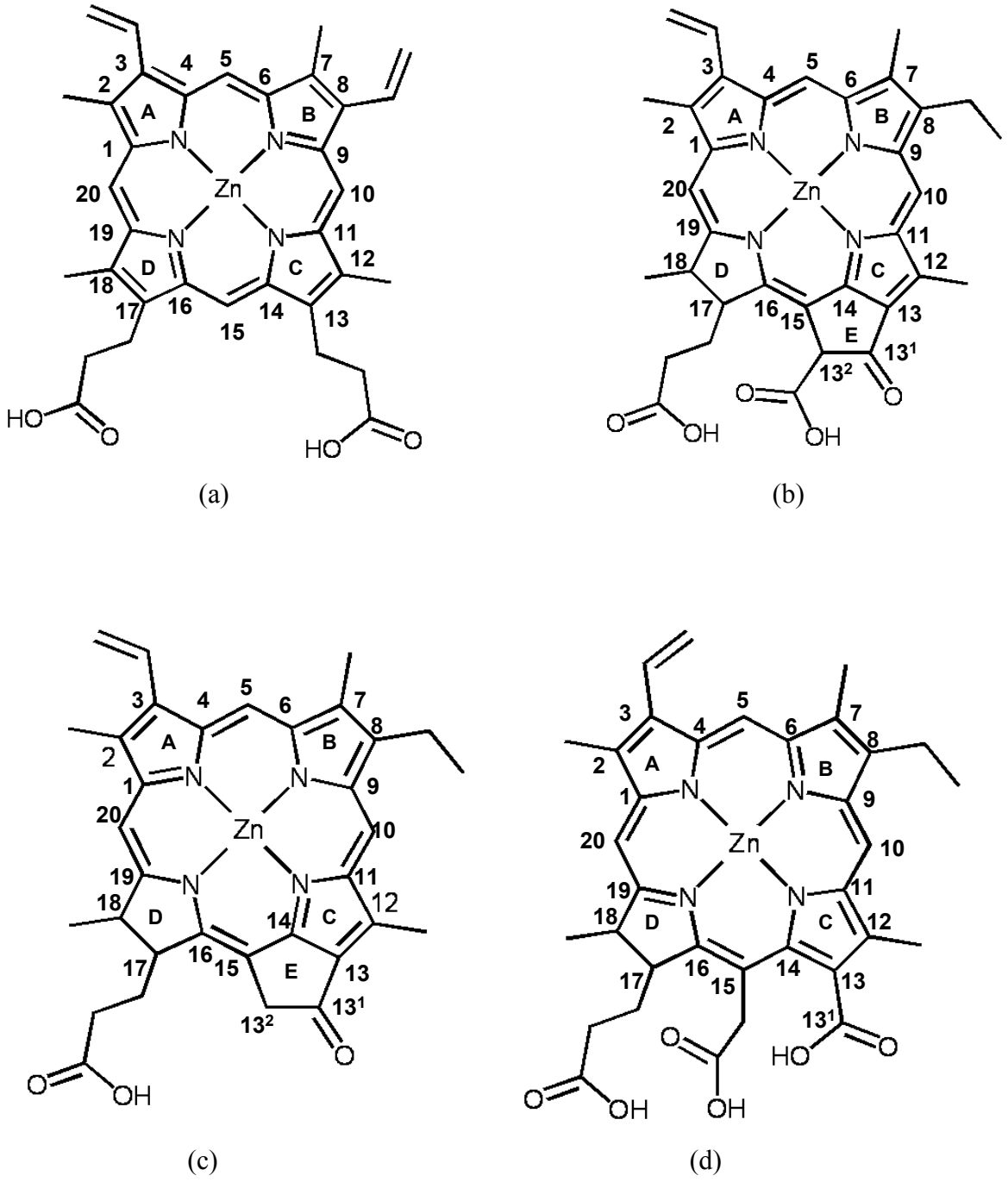

Figure 1.11 Structure and nomenclature of (a) zinc proptoporphyrin IX (b) zinc chlorophyllide (c) zinc pyrochlorophyllide (d) zinc chlorin e_6

The structure and nomenclature of the model systems are shown in Figure 1.11 (a)-(d). Their synthesis and characterization is explained in Chapter 2, Materials and methods.

The central metal Mg in the chlorophyll molecule is easily removed by weak and strong acids. It is very difficult to introduce Mg again into the porphyrin ring. Attempts to reintroduce Mg using Grignard reagents have resulted in ring modifications and poor yields [46, 47]. However, zinc can be readily introduced into the porphyrin ring just by warming a solution of the chlorin and the acetate of the metal (zinc acetate) [48]. The reintroduced zinc is quite stable and can be removed only by strong acids. Zinc is in its +2 oxidation state (d^{10}) and EPR silent. This allows the probe of the porphyrin triplet state without interference from the central metal. Other metals like Iron and Cobalt have also been successfully introduced into the porphyrin ring [48], but are not EPR silent.

CHAPTER 2: Materials and methods

2.1 Synthesis of chlorophyll model systems

2.1.1 Extraction and purification of chlorophyll a

Chlorophyll from fresh spinach: Chlorophyll was extracted from fresh spinach leaves by the method described by Iriyama [49]. Dioxane is used in the first step for selective precipitation of chlorophyll from the crude methanol extracts. All solvents purchased from Sigma were reagent grade and further purified by standard methods to remove trace contaminants. Fresh commercially available spinach leaves were used and all procedures were carried out at +4^{o} C under dim green light.

Spinach leaves (100g) were washed in cold water and shredded in a blender with 500ml cold methanol. The content of the blender was filtered through a cotton pad to separate the filtrate. The filtrate was then centrifuged at 1000*g for 5 minutes to remove any other insoluble material. The supernatant was decanted into a beaker and mixed with one-seventh its volume of freshly distilled dioxane. Then 80ml of milli-Q water was added dropwise with stirring, until high turbidity developed. This was allowed to stand in ice for one hour to allow sedimentation. The sediment was collected by centrifugation at 10000*g for 5 minutes. The crude mass of chlorophyll obtained was dissolved in approximately 150ml of methanol:dioxane (7:1, v/v) and precipitated again by drop wise addition of 25ml milli-Q water. The last procedure was repeated 2 times and the final product was subjected to HPLC for further separation of chl a from the crude extract. The sample was dried and stored at -30^{o} C until HPLC.

Chlorophyll from dry spinach: Chlorophyll from dry spinach was extracted by the method described by Schwartz[50] with some modifications. Fresh commercially available spinach leaves were used and all experiments were carried out at +4 ^{o}C and under dim green light.

Spinach leaves were dried for 2-3 days at 30-40 ^{o}C until they could crumble in the hands. They were milled and stored at -30 ^{o}C. The dry leaves were washed twice in a blender with 500ml petroleum ether to remove the carotenoids and waxes. They were then extracted twice using 400ml of methanol:petroleum ether (3:1, v/v). The combined extract was then transferred to a separatory funnel and washed with 250ml of saturated

aqueous NaCl. The layers are separated and the aqueous layer is further extracted with 200ml petroleum ether. The ether extracts were combined and washed again with 100ml saturated aqueous NaCl. The ether extract was filtered in a clean fritted funnel and dried. This residue was dissolved in 50ml acetone and left overnight at -20 ^{o}C. The acetone fraction was filtered with a fritted funnel and solvent was evaporated using a rotary evaporator. The dry sample was stored at -30 ^{o}C until HPLC purification.

HPLC of chlorophyll: The chlorophyll extracted from spinach is rich in chlorophyll a, but also contains other pigments like chlorophyll a`, chlorophyll b, carotenoids. These were removed by high performance liquid chromatography [51]. The sample preparation and HPLC was done under dim green light and the samples were prepared quickly to reduce degeneration of chlorophyll a. All solvents were bubbled with argon before use.

The preparative HPLC apparatus consisted of a Model Abimed 306 high-pressure pump (Gilson), a Model SPD-10AV-VP variable wavelength diode array detector (Shimadzu) fixed at 430 nm, and a Model 7125 sample injector equipped with a 2 ml loop. The stainless steel column (250 mm X 21 mm i.d.) was packed with a 7-uL silica gel (Nucleosil 100-7, C18, Macherey-Nagel). The chlorophyll sample was dissolved in a 2 mL mixture of dichloromethane/methanol (1:7, v/v). A maximum of 50 mg of the sample was dissolved in this mixture and injected. Elution was done isocratically with the same solvent. Chlorophyll a fraction was determined by its characteristic absorption spectrum and collected.

Analytical HPLC was performed to determine the purity of chlorophyll a. The analytical HPLC apparatus consists of a Model Abimed 306 high pressure pumb (Gilson), a Model SPD-M10AV variable wavelength diode array detector (Shimadzu) set at 430 nm and a Model 7125 sample injector equipped with a 20uL loop. The stainless steel column (150 mm X 4.6 mm i.d.) was packed with a 3 um silica gel (Nucleosil 100-3, C18, Macherey-Nagel). The solvent and conditions are the same as mentioned for the preparative HPLC. Chlorophyll from both the extraction procedures yielded chlorophyll a with 96-98 % purity. The collected chlorophyll a was dried immediately in a rotary evaporator and stored at -30 C until further use.

The chlorophyll model systems, zinc chlorophyllide and zinc pyrochlorophyllide have been synthesised and characterized by well established procedures. The starting material for these model systems was Chlorophyll a which was extracted and purified from spinach as described above. The concentration of chlorophyll was determined by the method of Porra [103]. Chlorin e_6 was purchased from Frontier Scientific and was metallated with zinc by procedure described by [45]. Zinc protoporphyrin IX was purchased from Sigma Aldrich and used without further purification.

2.1.2 Synthesis of zinc chlorophyllide from chlorophyll a:

All the procedures are carried out in dim green light and the solvents employed are reagent grade. To the dry and HPLC pure chlorophyll a (25mg), 3 ml of trifluoroacetic acid was added and stirred under argon for 90 minutes. This step removes the central metal Mg and also hydrolyses the phytyl ester tail from chlorophyll a. After stirring, the solvent was removed using an oil pump with liquid nitrogen in the cold trap. The obtained chlorophyllide is pure and need not be subject to further purification.

Insertion of zinc:

This chlorophyllide was dissolved in 15 ml of acetic acid and zinc acetate corresponding to 200 times the molar ratio of chlorophyllide was added. 100 mg of sodium acetate and 20 mg of sodium ascorbate were also added. This was stirred under argon for 60 minutes. Twice the volume of toluene was added to bring down the boiling point of acetic acid and this mixture was removed using an oil pump with a liquid nitrogen cold trap.

Extraction of zinc chlorophyllide:

The residue obtained after removing the solvent was dissolved in a water-ether mixture and allowed to stand in a separatory funnel. The ether layer contains the zinc chlorophyllide and the aqueous layer contains unreacted zinc acetate. The ether layer was removed and washed twice with water. Traces of water from the ether were removed using sodium sulphate and then the ether was removed using a rotary evaporator.

Purification of zinc chlorophyllide:

Zinc chlorophyllide was purified by HPLC. The HPLC set up was the same as described before.

UV/Vis (Diethylether): 667 nm (0.58), 609 nm (0.08), 561 nm (0.03), 533 nm (0.10), 504nm (0.12), 466 nm (0.04), 407 nm (1.00)

NMR data for Zn chlorophyllide:

^{1}H-NMR (ppm), 400 MHz, Pyridine-d_5, δ = 1.67 (t, 3H, CH_3-8^2), 1.72 (d, 3H, CH_3-18^1), 2.54 (m, 1H, CH_2-17^1b), 2.68 (m, 1H, CH_2-17^2b), 2.84 (m, 1H, CH_2-17^2a), 2.96 (m, 1H, CH_2-17^1a), 3.26 (s, 3H, CH_3-7^1), 3.37 (s, 3H, CH_3-2^1), 3.72 (s, 3H, CH_3-12^1), 3.77 (q, 2H, CH_2-8^1), 3.84 (s, 3H, CH_3-13^4), 4.49 (m, 1H, CH-17), 4.57 (dq, 1H, CH-18), 6.08, 6.31 (per d, 2H, CH2-3^2), 6.78 (s, 1H, CH-13^2), 8.27 (dd, 1H, CH-3^1), 8.67 (s, 1H, CH-20), 9.74 (s, 1H, CH-5), 9.93 (s, 1H, CH-10).

2.1.3 Synthesis of zinc pyrochlorophyllide:

All the procedures were carried out under dim green light and reagent grade solvents were employed. To the dry and HPLC pure chlorophyll a (50mg), 150 ml of 2,4,6 trimethyl pyridine was added and refluxed at 170 C under argon for 6 hours. The solvent was removed using an oil pump set with a liquid nitrogen cold trap. The residue was dissolved in a water-ether mixture and allowed to stand in a separatory funnel. The ether layer was removed and washed twice with water and the ether was evaporated in a rotary evaporator.

Zinc was inserted into this pyrochlorophyllide by following the same procedure mentioned for metallation of chlorophyllide and then the zinc pyrochlorophyllide was subject to HPLC purification.

UV/Vis of pyrochlorophyllide (Diethylether):

667 nm (0.50), 609 nm (0.07), 534 nm (0.09), 505 nm (0.11), 409nm (1.00)

UV/Vis of zinc pyrochlorophyllide (Diethylether):

655 nm (0.52), 610 nm (0.05), 427 nm (0.85), 405 nm (0.40), 319 nm (0.15)

NMR data of zinc pyrochlorophyllide:

^{1}H-NMR (ppm), 400MHz, $CDCl_3$: 10.00 (s, 1H, H-10), 9.76 (s, 1H, H-5), 8.74 (s, 1H, H-20), 8.31 (dd, 1H, CH-3^1), 6.33, 6.10 (per d, 1H, CH_2-3^2), 5.42, 5.20 (per d, 1H, CH_2-13^2), 4.53 (dq, 1H, H-18), 4.35 (m, 1H, H-17), 3.84 (q, CH_2-8^1), 3.83 3.62, 3.59, 3.43 (per s, 3H, CH_3-12^1, CH_3-7^1, O CH_3, CH_3-2^1), 2.8-2.45 (m, 4H, CH2-17^1, CH2-17^2), 1.80 (d, 3H, CH_3-18^1), 1.73 (t, 3H, CH_3-8^2).

2.1.4 Synthesis of zinc chlorin:

Chlorin is purchased from Frontier Scientific and then metallated with zinc. Chlorin was dissolved in 25 mm glycin buffer, pH 10.0. Zinc acetate in ratio of 1:1 with respect to chlorin was added and stirred for 90 minutes under argon in +4 C. The mixture was centrifuged at 3000*g and +4 C for 10 minutes to precipitate any unreacted zinc acetate. The supernatant was subjected to HPLC to separate zinc chlorin from any unreacted chlorin.

UV-Vis of Zn chlorin in MES buffer: 412 nm (1.00), 520 nm (0.03), 593 nm (0.04), 633 nm (0.22)

2.2 Extraction and purification of myoglobin from dolphin meat

Myoglobin was extracted from Porpoise (*Phocoena phocoena)*, Atlantic white sided dolphin (*Lagenorhynchus acutus*) and Bottle nose dolphin (*Tursiops truncatus*). The meat (sans bones and skin) was shipped from a Marine research facility, Netherlands and was from dolphins that had been washed ashore dead. They were frozen and stored at -30 ^{o}C. The protein was extracted by the procedure described by [52]. 50g of the meat was thawed overnight and cut into small pieces and blended in a commercial blender for 20 minutes with 70% ammonium sulphate solution (prepared in 20mM phosphate buffer). A soaking interval of 5 minutes was provided after every 5 minutes of blending. The contents were then centrifuged at 11750*g at +4 ^{o}C for 20 minutes. The supernatant was filtered through a Whatman filter paper and subjected to dialysis against milli-Q water at +4^{o}C for 48 hours. The water was changed every 8 hours. The ionic strength of the

dialyzed myoglobin was set to 0.1 with KCl and 50% of molar excess of potassiumferricyanide was added. This myoglobin was let to stir at +4 ^{o}C and then centrifuged at 400*g for 15 minutes. The supernatant was loaded into a Sephadex CM 25 column which was equilibrated at pH 6.0 with 20mM phosphate buffer. The column was first developed with 20mM phosphate buffer, pH 6.0 until the excess potassium ferricyanide was eluted. Then a pH gradient of 6.0 and 8.0 was applied and finally elution was done with 20mM phosphate buffer, pH 8.0. The myoglobin was concentrated and stored as frozen solution at -30^{o}C until further use.

The protein in the supernatants of the homogenates of the muscle prepared in 70% saturated ammonium sulphate is composed of more than 90% myoglobin. Only a small fraction of non heme proteins and hemoglobin contaminate the myoglobin and this contamination is removed with the CM Sephadex column. Hence, the myoglobin obtained is highly pure and is indicated by single band migration in SDS PAGE and sharp peaks in the MALDI spectra.

The concentration of the protein was calculated with the extinction coefficients at wavelength 409 nm already reported by Hapner at al.

2.3 Preparation of reconstituted myoglobin

Apo myoglobin was prepared by procedure described by Tele [53]. The myoglobin was dissolved in milli-Q water and pH was carefully adjusted to 1.5 using 0.1N HCl. This was transferred to a separation funnel and shaken with cold 2-butanone. The organic phase was removed and the aqueous phase was further washed twice with 2-butanone. Apo myoglobin in the aqueous phase was dialysed against 50 mm phosphate buffer, pH 7.0 containing 50 mg/L sodium bicarbonate and 0.1 mm EDTA for 8 hours and further against milli-Q water for 8 hours.

The cofactor was dissolved in minimum pyridine (200µl) and added drop wise into a solution of apo myoglobin in 50 mm phosphate buffer, pH 8.0. It was stirred for 1 hour at 4^{o}C and under dim green light. This solution was filtered through a Whatman filter paper and purified using a pre prepared PD-10 column with 20mM phosphate buffer, pH 7.0. The reconstituted myoglobin was characterised by established UV-Vis absorption spectra reported by Boxer [54]. Samples meant for crystallization were

utilized immediately while those for EPR studies were stored frozen in tubes at -30^{o}C until further use.

UV Vis data of reconstituted myoglobins

1. **Zn protoporphyrin IX – myoglobin :** 595 nm (0.01), 553 nm (0.02), 428 nm (0.52), 350 nm (0.09)

2. **Zn chlorophyllide – myoglobin :** 661 nm (0.76), 622 nm (0.15), 437 nm (1.00), 418 nm (0.64), 388 nm (0.37), 337 nm (0.32)

3. **Zn pyrochlorophyllide – myoglobin :** 660 nm (0.64), 620 nm (0.13), 437 nm (1.00), 415 nm (0.55), 392 nm (0.33), 333 nm (0.28)

4. **Zn chlorin – myoglobin :** 634 nm (0.12), 593 nm (0.04), 523 nm (0.05), 418 nm (0.41)

2.4 EPR/ENDOR

All sample preparation for EPR/ENDOR was carried out under green light. The cofactors were dissolved in pyridine and immediately frozen inside EPR sample tubes with liquid nitrogen. Samples in pyridine needed no additional chemicals for glass formation during freezing. However for samples in DMSO, MES buffer and myoglobin, 30% Glycerol was added to enable formation of transparent glass. This is important for the in situ excitation by a laser. The samples with organic solvents were prepared in an oxygen free environment (under Argon).

Electron Spin Echo (ESE) detected EPR and ENDOR spectra were recorded on a Bruker Q-band Elexsys E580 FT pulse EPR spectrometer equipped with a home-built EPR/ENDOR resonator, and an Oxford CF935 helium gas-flow cryostat. Samples were excited with an Opotek OPO laser at variable wavelength, pumped by a Vibrant Nd:YAG laser at 10 Hz repetition rate. Excitation at 532 nm was performed with 10 mJ/pulse. The EPR and ENDOR measurements were carried out at 10 K and the microwave frequency was around 34 GHz (± 0.004 GHz) depending on the sample.

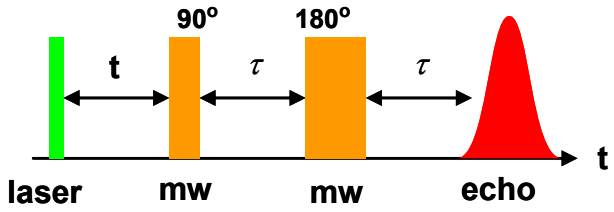

(A)

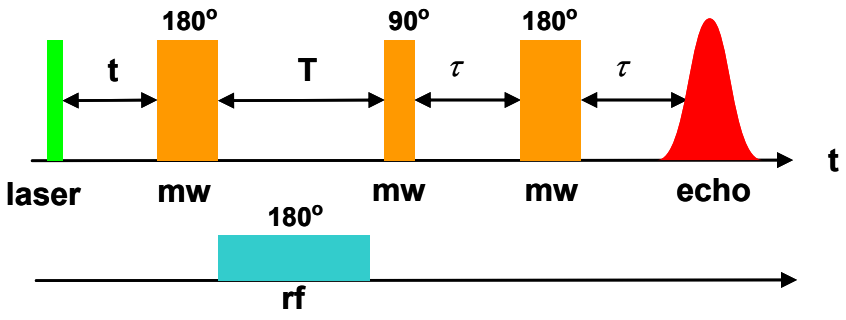

(B)

Figure 2.1 (A) DAF ESE sequence (B) DAF Davies ENDOR sequence

The delay after flash (DAF) ESR sequence is shown in Figure 2.1 (A). It consists of a laser flash and followed by two microwave pulses and detection of Hahn echo. Pulses of lengths 40 ns and 80 ns were used and in some cases 20 ns and 40 ns were used respectively. The delay between the pulses was 500 ns and microwave power was 20 mW.

A pulsed ENDOR scheme is represented in Figure 2.1 (B). A weak selective microwave pulse was used for preparation (pulse length 300 ns, t = 1μs) and a standard Hahn echo scheme was used for detection (pulse sequence $\pi/2$ - π with pulse lengths 150 and 300 ns, τ = 440 ns). The detection pulses were applied 2 μs after the end of the radio frequency π pulse of 20μs length. The accumulation time was typically 20 minutes for an EPR spectrum and 6-12 hours for an ENDOR spectrum depending upon the sample and magnetic field position.

2.5 DFT calculations

DFT calculations on chlorophyll model system triplet states were performed with the ab initio, DFT and semi empirical SCF MO package ORCA [55-58]. The BP86 functional, TZVP [59] basis set and TZV/C [60] auxiliary basis set were used to perform the calculations. The convergence criteria for the SCF procedure were 10^{-7} Hartree for the change in total energy and 10^{-4} for the DIIS error. The model geometry of chlorophyll model systems was derived from the structure of porphyrin taken from PDB entry 1YMB. The central metal was replaced with zinc and suitable changes were made in the side chains. All protons and methyl groups were geometry optimized using the program Gaussian [61] to improve the calculation of the hyperfine couplings. Calculations were performed with and without an axial ligand (pyridine). In all the cases, the axial ligand was found passive to the electron spin density distribution in the HOMO-1, HOMO, LUMO and LUMO+1 orbitals. The results presented here are without the axial ligand.

The hyperfine coupling constants for the methyl groups and β protons in the triplet calculations were calculated by response theory using a spin-unrestricted Kohn-Sham formalism (UKS) [62]. The accuracy of such calculations for reproduction of hyperfine coupling constants is typically 25% [62]. The three proton hyperfine coupling

tensors of the methyl groups were averaged and diagonalized to obtain mean hyperfine coupling constants for a rotating methyl group. In order to accurately take into account spin-polarization effects, isotropic hyperfine coupling constants for the methine protons have been calculated using spin-unpolarized orbitals from an additional calculation of the singlet ground state, followed by artificial promotion of an electron from HOMO to LUMO without performing additional SCF iterations.

2.6 Simulations

The EPR spectra of the spin-polarized triplet state of the chlorophyll model systems were simulated using a home written program (by E. Reijerse) in Matlab^{TM} [63] environment, which calculates the two positions of the triplet state transitions in the first order approximation for the zero field splitting (ZFS). It is assumed that the T_0 state is populated exclusively and that g and ZFS-tensors are collinear.

CHAPTER 3: INTRODUCTION TO ELECTRON SPIN RESONANCE

3.1 Introduction to the spin systems

Systems with $S > 0$ will experience a quantization of spin states when placed in an applied magnetic field and exhibit discrete spin states according to the multiplicity rule $2S + 1$ [2]. Thus for a system with one unpaired electron ($S = 1/2$), the multiplicity is a doublet [2(1/2) + 1 = 2], i. e., there are two spin states, α and β, with spin quantum numbers (M_S) equal to +1/2 and -1/2, respectively. The interaction between the spin and the field is described by the Zeeman effect — the energy separation of the two spin states increases with the increase of the applied magnetic field according to the equation

$$E = g_e \beta_e M_S B_0 \qquad (1)$$

where g_e is the electronic g-factor, β_e is the Bohr magneton, M_S is the spin quantum number and B_0 is the applied field. In the absence of an applied field the α or β spin states of the electron are degenerate as shown in Figure 3.1. Application of an applied field lifts the degeneracy of the two spin states. The α spin state, whose magnetic moment opposes the applied field, rises in energy while the β spin state, whose magnetic moment is aligned with the applied field, decreases in energy as the strength of the applied field increases. When a frequency of energy which matches the energy separation between the two spin states is applied absorption occurs which causes a transition between the two spin states. The selection rule $\Delta M_S = \pm 1$, $\Delta M_I = 0$ governs the transition. (M_I is the nuclear spin quantum number.) This absorption is detected and is the basis of the EPR experiment as shown in Figure 3.1. EPR spectra are usually shown as the first derivative of the absorption curves. The following discussion assumes the EPR experiment is performed by fixing the applied frequency and sweeping the field.

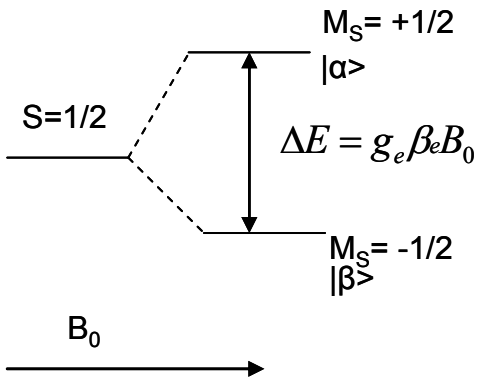

Figure 3.1 Energy diagram for S = ½ system

When two unpaired electrons are present in a system, the state depends upon the alignment of the two electrons. If the unpaired electrons are aligned antiparallel, the multiplicity is a singlet [2(0) + 1 = 1]. As the name suggests, there is only one spin state and thus no EPR transition is observed. When the spins are aligned parallel (S = 1), the multiplicity is a triplet [2(1) + 1 = 3]. According to the $\Delta M_S = \pm 1$ selection rule, there are two allowed transitions. The effective magnetic field experienced by each electron, however, is the vector sum of several magnetic fields, not just the externally applied field. The internal fields are operative in the absence of the externally applied field and are due to magnetic moments of nuclei, the other unpaired electron and possibly a contribution from each electron's own orbital angular momentum [64]. However, only the internal magnetic field associated with the spin of the other electron is considered because the magnetic moment of the electron is approximately three orders of magnitude larger than the nuclear magnetic moment. The influence of its magnetic field is significantly larger than that of the nuclei [65].

3.2 THE ZERO FIELD SPLITTING

To explain the effect of each unpaired electron's magnetic field on the other unpaired electron it is helpful to view the electrons as dipoles that experience repulsive dipole-dipole interaction due to their parallel alignment. As a consequence of this repulsive dipolar coupling the lowest energy state will be the state where the two electrons are furthest apart. Figure 3.2 depicts the energy states of three idealized triplet systems as a function of electron distribution [68]. T_Z represents a state in which the spin axes of the two electrons have been quantized so that they are confined to the *XY* plane and the component of the spin angular momentum in the *Z*-direction is zero. Likewise for T_Y the spin axes are confined to the *XZ* plane with a zero component along the *Y*-axis and for T_X the spin axes are confined to the *YZ* plane with a zero component along the *X*-axis. In (a) the electrons are spherically distributed. There is no direction in which the electrons can move to get further apart to minimize the repulsive dipole-dipole interaction and as a result the three states remain degenerate. In (b) where the spin distribution has been compressed along the *Z*-axis, the two electrons will experience a more repulsive interaction when they are aligned in either the *XZ* plane (T_Y state) or *YZ* plane (T_X state) because they will be closer together. They can stay further apart in the *XY* plane (T_Z state) which results in a lower energy state. A third scenario adds to the compression along the *Z* axis an elongation along the *X*-axis resulting in the state splitting shown in (c). Again the lowest energy state corresponds to the alignment of the spin axes in the *XY* plane for the same reason given above. The highest energy states also correspond to the alignment of the spin axes in the planes of *Z*-direction because of the major compression along the *Z*-axis, but a further splitting occurs due to the additional elongation along the *X*-direction. The spins experience the largest repulsive interaction (closest proximity) when confined to the *YZ* plane and therefore the highest energy state corresponds to alignment of the spin axes in the *YZ* plane (T_X state).

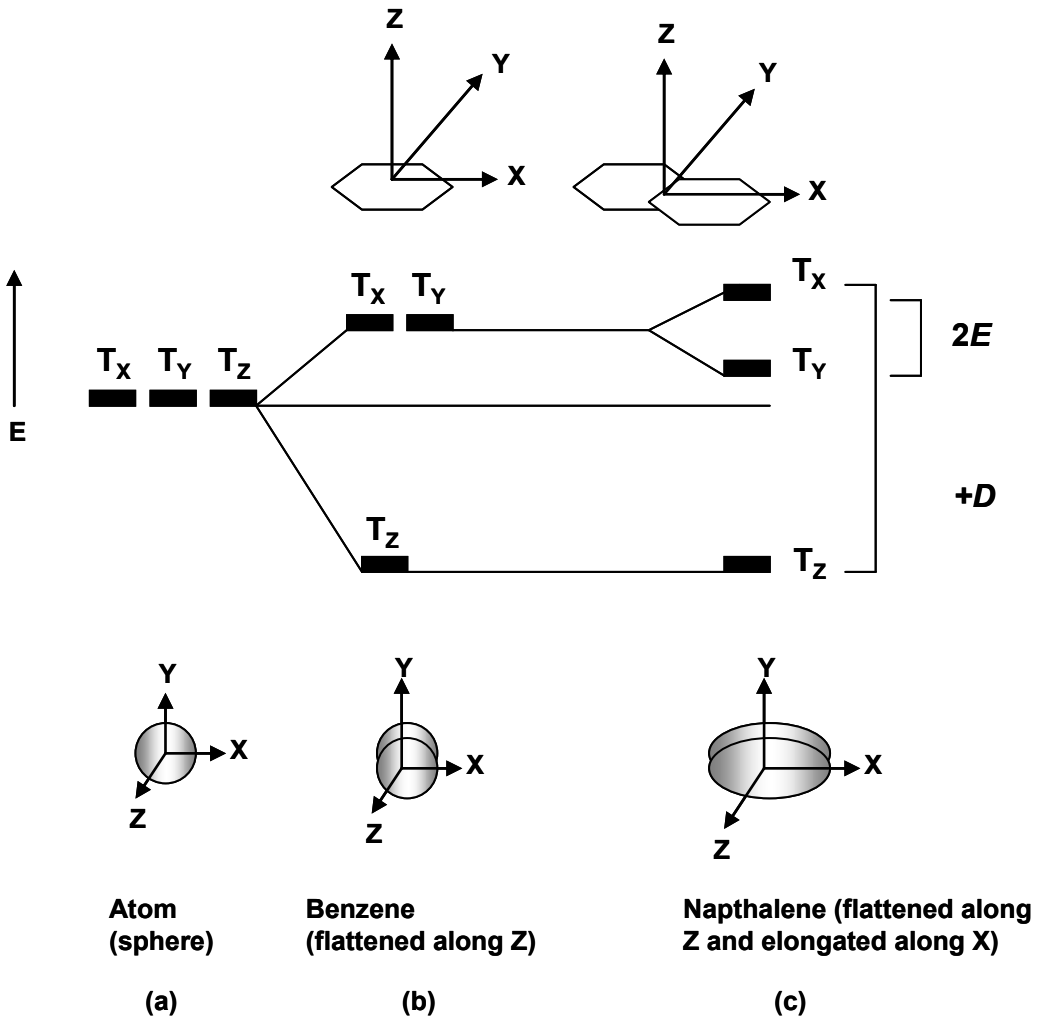

Figure 3.2 Energy states as a function of electron distribution: +***D***

As described above, the quantization of the spin states does not result from an externally applied field, but rather from the molecular geometry. This energetic effect in zero field is due to the anisotropic electron distribution and is described by the ZFS parameters ***D*** and ***E***. ***D*** is defined as the energy difference between the lower energy state and the higher degenerate energy states as in (b) or between the lowest energy state and the average of the higher two energy states as in (c). The parameter ***E*** is 1/2 the energy difference of the higher energy states. ***D*** is positive for an oblate spin distribution — a flattening in one direction (Figure 3.2). ***D*** can also be negative if the electron distribution is prolate — an elongation in one direction (Figure 3.3). Thus the geometrical shape of the spin distribution can be estimated from ***D*** and ***E*** [67].

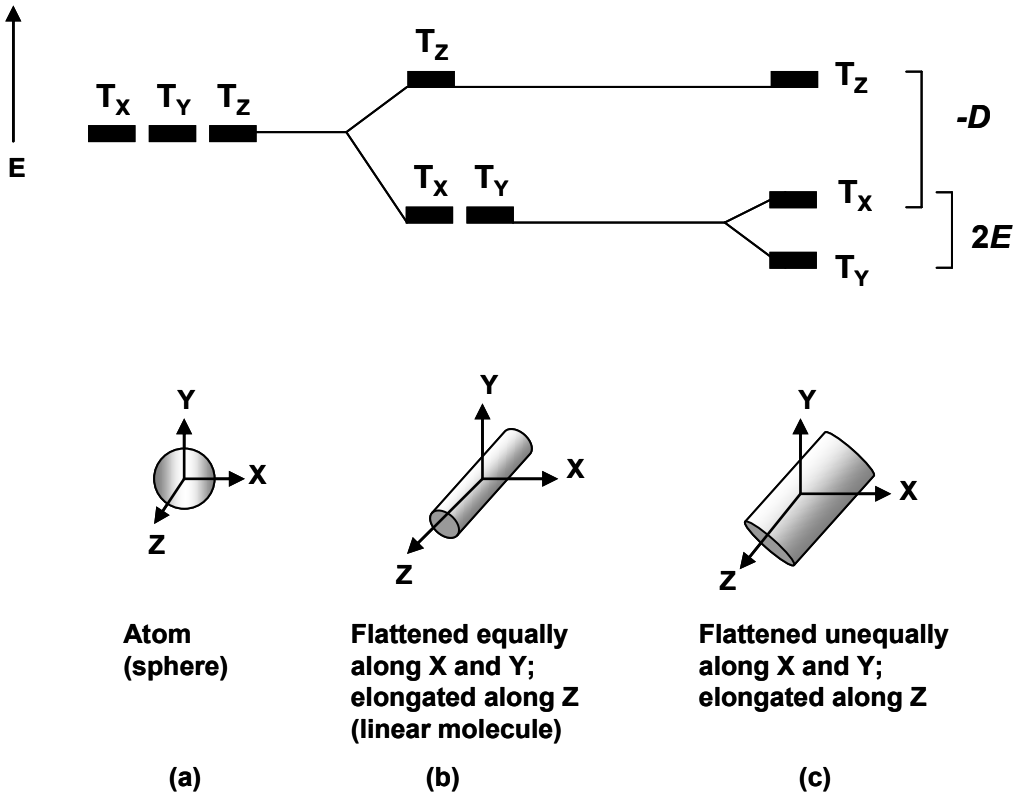

Figure 3.3 Energy states as a function of electron distribution: ***-D***

The two-fold degeneracy in (b) of Figure 3.2 is characteristic of any triplet species which possesses three-fold or higher symmetry and a magnetically isotropic plane perpendicular to the symmetry axis (axial symmetry). The zero field splitting of the energy states of such a triplet is described by ***D***. The zero field splitting of the energy states of a triplet species with lower symmetry (rhombic symmetry) are described by both ***D*** and ***E*** as in (c). For spherical electron distribution (cubic symmetry) as in (a) there is no zero-field energy state splitting. EPR is the technique used to determine the energies of ***D*** and ***E***.

The simplest triplet EPR spectrum is that of a simple atomic triplet system with cubic symmetry. When such a system is placed in an applied magnetic field with the field aligned with the molecular *Z*-axis (B_Z), the electrons whose spin vectors are in the *XY* plane will remain at the same energy (T_0 state) since their spin vectors are perpendicular to the applied field. The electrons whose spin vectors are in either the *XZ* or *YZ* planes

however will either be stabilized or destabilized depending on whether the magnetic moments are aligned with (T_{-1} state) or against (T_{+1} state) the applied field, respectively. There are two allowed transitions, but since they occur at the same field strength, only one signal is detected. Because of the spherical symmetry, the splitting pattern will be identical for all three canonical orientations, i.e., the spectra observed for B_X and B_Y applied fields will be identical to the spectrum observed for B_Z.

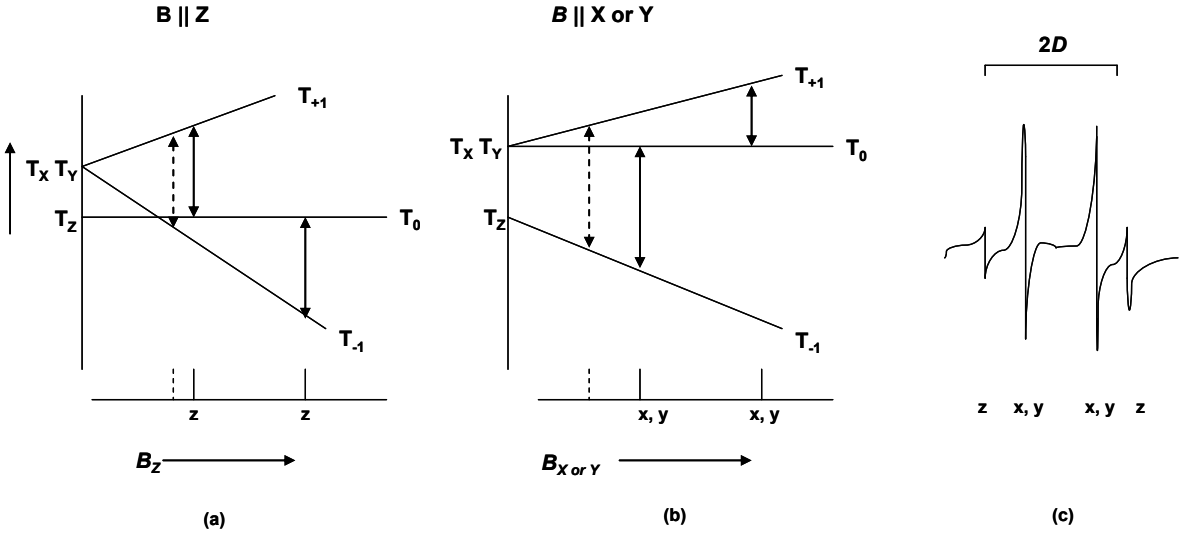

Figure 3.4 Energy diagram and absorption curves for S = 1 D > 0 axial system. (a) Applied field aligned with the molecular axis. (b) Applied field aligned with the molecular X- or Y-axis. (c) Simulated spectrum of absorptions.

Lowering the symmetry from cubic symmetry to axial and rhombic symmetry results in energy splitting similar to those depicted in Figures 3.4 and 3.5 respectively. The solid arrows represent the $\Delta M_S = 1$ allowed transitions. The dotted arrow represents the $\Delta M_S = 2$, formally forbidden transition.

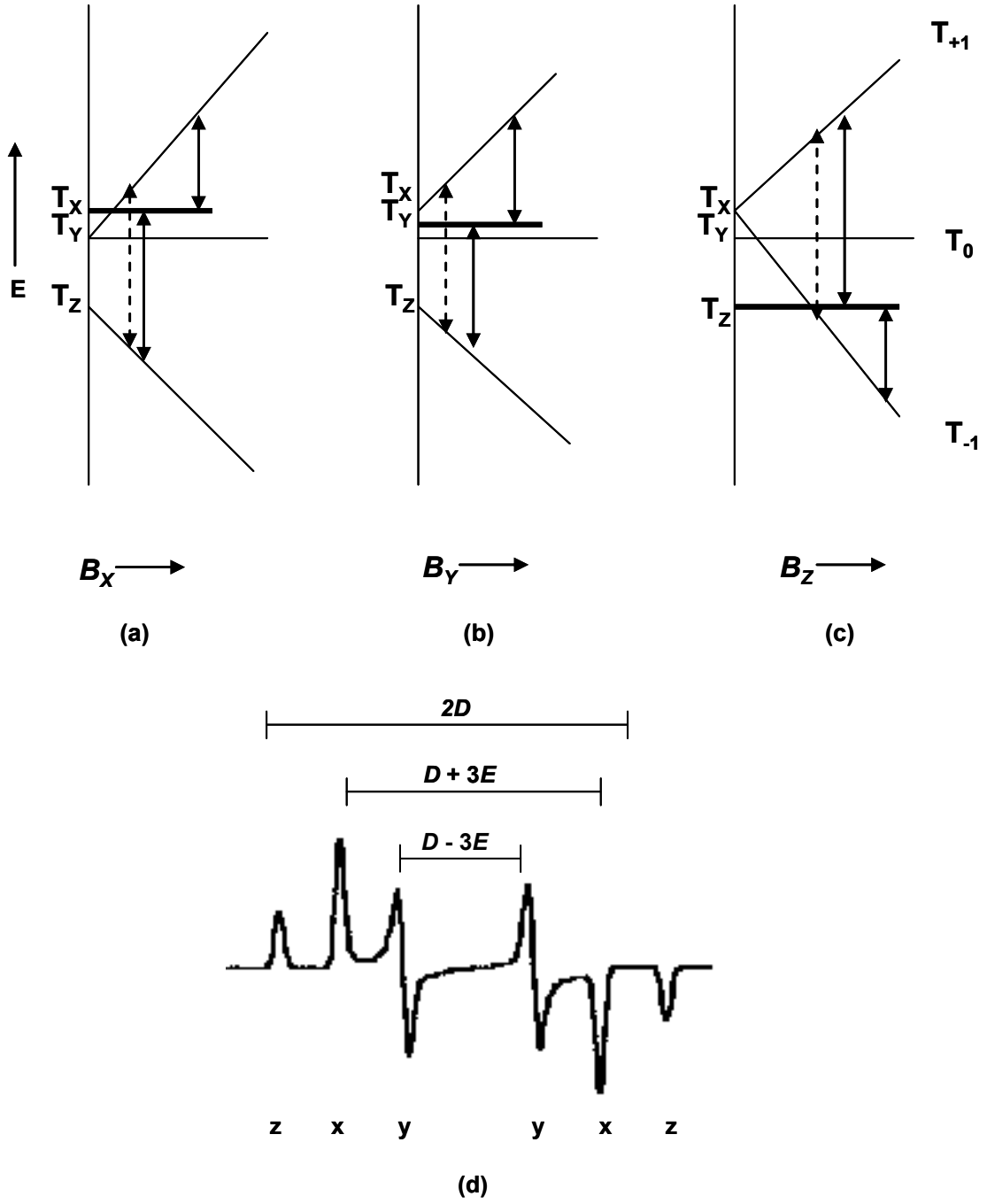

Figure 3.5 Energy diagram for absorption curves for S=1, D>0 and $|D| \neq 3|E|$ rhombic system. (a) Applied field aligned with molecular Z-axis. (b) Applied field aligned with the molecular Y-axis. (c) Applied field aligned with the molecular Z-axis. (d) Simulated spectrum and ZFS parameter determination.

As the strength of the applied field increases the major cause of the energy splitting shifts from the molecular quantization due to the spin-dipolar coupling (with eigen functions

T_X, T_Y T_Z) to the applied field quantization described by the Zeeman effect (with eigen functions T_{+1}, T_0, T_{-1}.) The zero-field triplet eigen functions, T_X, T_Y T_Z are not the same as the eigen functions of the high-field spin Hamiltonian, T_{+1}, T_0, T_{-1}. The zero-field eigen functions are rather a mixture of the high-field eigen functions.

$$T_X = 1/\sqrt{2}\,(T_{-1} - T_{+1})$$
$$T_Y = 1/\sqrt{2}\,(T_{-1} + T_{+1}) \qquad (2)$$
$$T_Z = T_0$$

The spin quantum numbers, $M_S = \pm 1, 0$, are suitable quantum numbers for the high-field eigen functions, but not for the zero-field eigen functions. The dashed arrows in Figures 3.4 and 3.5 at low fields represent the $\Delta M_S = 2$ transition which is formally forbidden. At lower fields the spin quantum numbers, $M_S = \pm 1, 0$, are not well-defined and thus the selection rule is relaxed.

Several important differences are noted between EPR spectra of cubic, axial and rhombic systems. Whereas the energy splitting pattern of a cubic system is the same regardless of the applied field orientation, the energy splitting pattern of an axial or rhombic system is dependent upon the orientation of the applied field. Therefore the $\Delta M_S = 1$ transitions for axial and rhombic systems do not occur at the same field strength as does the transitions for cubic systems. Two and three absorptions are observed for axial and rhombic systems, respectively, for each canonical orientation instead of one. For an axial system two states remain degenerate at zero field (T_X and T_Y in Figure 3.4) and application of the fields BX and BY will result in absorptions at the same field strength. The absorption due to the application of the unique field direction (B_Z), however, will occur at different field strength as seen in Figure 3.4. Therefore an axially symmetric system is generally characterized by a four line spectrum with the distance between the outermost peaks equal to $2\boldsymbol{D}$ as shown in (c) of Figure 3.4. For a rhombic system with $|\boldsymbol{D}| \neq 3|\boldsymbol{E}|$ each canonical orientation will result in a different spectrum leading to a six line spectrum shown in (d) of Figure 3.5. From the spectrum it is possible to determine the energy values of $\boldsymbol{D}$ and $\boldsymbol{E}$ by the relations given in (d). When $|\boldsymbol{D}| = 3|\boldsymbol{E}|$ (peak labels in (d) of Figure 3.5) the two innermost peaks labeled "y" collapse to one central peak and

the peaks labeled "x" coincide with the peaks labeled "z" resulting in a three line spectrum.

It should be noted that the spectra described in Figures 3.4 and 3.5 are not usually observed if the experiment is performed in solution at room temperature. The two main contributors to the effective magnetic field at one electron are the externally applied field (B_Z) and the internal field associated with the other electron described by

$$B_{eff} = B_Z + \frac{\mu_{eff}(3\cos^2\theta - 1)}{r^3} \qquad (3)$$

where r is the distance between the unpaired electrons and θ is the angle formed by the applied field and the vector connecting the unpaired electrons. If the EPR experiment is performed in solution at room temperature the rapid tumbling on the time scale of the experiment causes the angular dependence term in equation 3 to average to zero and all spectroscopic consequences of dipolar coupling are eliminated. Therefore to observe manifestations of ZFS it is necessary to perform the experiment on powders, frozen glassy samples or single crystals.

The ZFS parameters ***D*** and ***E*** provide valuable information about the electron distribution in high spin systems are used to interpret the frozen EPR spectra of these systems.

3.3 The Spin Hamiltonian Approach:

The EPR spectrum can be interpreted in terms of the effective spin Hamiltonian that describes the interactions of the electron and nuclear spins with the applied magnetic field and with each other [68]. The spins are expressed in terms of operators and the interactions as coupling coefficients and by analyzing the spectra, these interactions can be quantitatively determined.

3.3.1 The Zeeman interaction

The EPR spectrum of a free radical or coordination complex with one unpaired electron (S = ½) gives rise to a simple Lorentzian resonance signal. When an electron is placed in a magnetic field, the degeneracy of the electron levels is lifted and described by the spin Hamiltonian:

$$H_{Ze} = g_e \beta_e \vec{B}.\vec{S} \quad (4)$$

Therefore the electron spin energy levels become,

$$E_{\pm} = \pm(1/2) g_e \beta_e B \quad (5)$$

The energy levels are depicted in Fig. 3.1 together with their eigenfunctions.

The difference in energy between two levels equals:

$$\Delta E = g_e \beta_e B \quad (6)$$

When a field with frequency ν is applied, the resonance condition

$h\nu = g_e \beta_e B$ is satisfied. (7)

The same considerations are valid for nuclear spins described by the nuclear Zeeman Hamiltonian:

$$H_{Zn} = -g_n \beta_n \vec{B} \cdot \vec{I} \quad (8)$$

The nuclear energy is much smaller than the electronic energy.

3.3.2 Hyperfine coupling

The magnetic interaction between the electron spin and nuclear spin can be described with an isotropic part (H_1) and an anisotropic part (H_2) of the hyperfine interaction.

$$\text{H} = H_1 + H_2 \quad (9)$$

The magnetic moments of the unpaired electron and the nucleus are coupled by the Fermi contact interaction as

$$H_1 = a\vec{I} \cdot \vec{S} \quad (10)$$

'a' is the coupling constant and it is proportional to the squared amplitude of the wave function of the unpaired electron at the nucleus.

$$a = \frac{8\pi}{3} g_e \beta_e g_n \beta_n |\varphi(0)|^2 \quad (11)$$

The dipolar hyperfine interaction between the magnetic moments of the electron is anisotropic and if the electron cloud is spherical, it averages to zero. It can he described by the following Hamiltonian,

$$H_2 = -g_e \beta_e g_n \beta_n \{\frac{\vec{I} \cdot \vec{S}}{r^3} - \frac{3(\vec{I} \cdot \vec{r})(\vec{S}.\vec{r})}{r^5}\} \quad (12)$$

3.3.3 Nuclear quadrapole interaction

Nuclei with $I \geq 1$ can have a non-spherical charge distribution so that they have a quadrupole moment.[1] The charge distribution can either be oblate or prolate. The Hamiltonian can then be written as a tensor coupling of the nuclear spin with itself,

$$H_Q = \vec{I}.\vec{\vec{P}}.\vec{I}\ , \quad (13)$$

where $\vec{\vec{P}}$ is the quadrupole coupling tensor.

The elements of the traceless tensor $\vec{\vec{P}}$ are,

$$P_{\alpha\beta} = \frac{eQ}{2I(2I-1)} V_{\alpha\beta} \quad (14)$$

where $V_{\alpha\beta}$ is the electric field gradient at the nucleus (α, β = x, y, z).

3.3.4 Multiple electrons, the triplet state Hamiltonian

A molecule in which the total spin of the electrons is equal or more than one ($S \geq 1$) has split electron spin energy levels even without the external magnetic field. In the case of a triplet state the energy level scheme consists of three distinct sublevels or states with almost the same energy. In the triplet state two unpaired electrons are present.

The spin Hamiltonian that describes the magnetic dipole interaction between the two electrons with spins $\vec{S}_1$ and $\vec{S}_2$ is

$$H_{ZFS} = \frac{\mu_0}{4\pi} g_e^2 \beta_e^2 \{\frac{\vec{S}_1 \cdot \vec{S}_2}{r^3} - \frac{3(\vec{S}_1 \cdot \vec{r})(\vec{S}_2 \cdot \vec{r})}{r^5}\} \quad (15)$$

The above equation can be expressed in the form of total spin $\vec{S}$ as,

$$H_{ZFS} = \vec{S} \cdot \vec{\vec{D}} \cdot \vec{S} \quad (16)$$

$\vec{\vec{D}}$ is the symmetric tensor called zero field splitting tensor which has the elements,

$$D_{\alpha\beta} = \frac{1}{2}\frac{\mu_0}{4\pi} g_e^2 \beta_e^2 \left\langle \frac{r^2 \delta_{\alpha\beta} - 3\alpha\beta}{r^5} \right\rangle \tag{17}$$

The $\vec{\vec{D}}$ is symmetric and traceless and can be coupled with suitable choice of axes. The Hamiltonian for this principal axis system is

$$H_{ZFS} = D_{XX} S_X^2 + D_{YY} S_Y^2 + D_{ZZ} S_Z^2 \tag{18}$$

Where, D_{XX}, D_{YY} and D_{ZZ} are principal values of $\vec{\vec{D}}$.

The $\vec{\vec{D}}$ can be expressed as,

$$D = D_{ZZ} - \frac{1}{2}(D_{XX} + D_{YY}) \text{ and} \tag{19}$$

$$E = \frac{1}{2}(D_{XX} - D_{YY}) \tag{20}$$

and

$$H_{ZFS} = D\{S_Z^2 - \frac{1}{3}S(S+1)\} + E(S_x^2 - S_Y^2) \tag{21}$$

The eigen values of the ZFS Hamiltonian are

$$E_X = \frac{1}{3}D + E \tag{22}$$

$$E_Y = \frac{1}{3}D - E \tag{23}$$

$$E_Z = -\frac{2}{3}D \tag{24}$$

Combining all the components, we can write the Hamiltonian as,

$H = \mathrm{H_{Ze}} + \mathrm{H_{Zn}} + \mathrm{H_{HF}} + \mathrm{H_{ZFS}} + \mathrm{H_Q}$ (or)

$$H = g_e \beta_e \vec{B} \cdot \vec{S} - g_n \beta_n \vec{B} \cdot \vec{I} + \vec{S} \cdot \vec{\vec{A}} \cdot \vec{I} + \vec{S} \cdot \vec{\vec{D}} \cdot \vec{S} + \vec{I} \cdot \vec{\vec{P}} \cdot \vec{I} \tag{25}$$

Applying a strong field approximation (as a result, the terms containing the nuclear spin operator becomes negligible compared to other terms),

$$H_T = g_e \beta_e \vec{B} \cdot \vec{S} + \vec{S} \cdot \vec{\vec{D}} \cdot \vec{S} \tag{26}$$

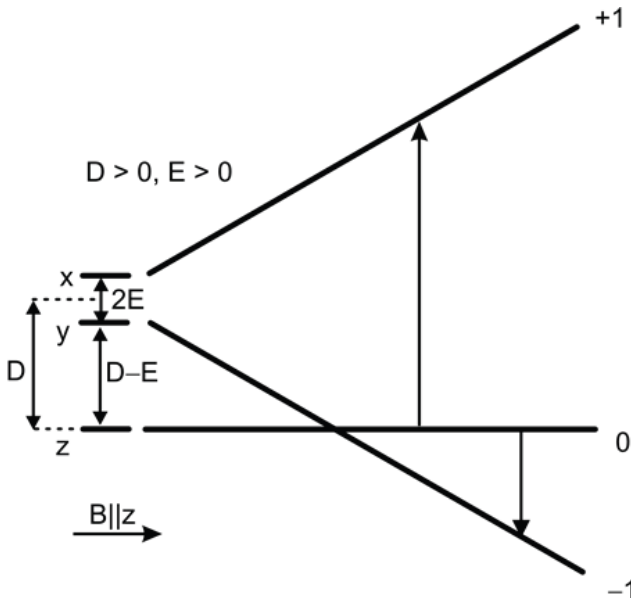

Figure 3.6 Energy level scheme of the triplet sublevels with the magnetic field direction parallel to the Z principal axis of the ZFS tensor. The zero-field-splitting parameters *D* and *E* are depicted in the figure.

The zero-field splitting of organic molecules in triplet states is dominated by the dipole-dipole interaction of the unpaired electrons. The ZFS parameters *D* and *E* are useful to characterize the electronic spin density distribution of these molecules in the triplet state. The energy level scheme for the magnetic field oriented parallel to Z is depicted in Fig. 3.2.Whether an EPR transition becomes absorptive or emissive depends on the relative populations of the energy levels, which in turn is determined by the mechanism of triplet formation. The full spin Hamiltonian for the triplet state with hyperfine interaction to one I = ½ nucleus is:

$$H_T = g_e \beta_e \vec{B}.\vec{S} - g_n \beta_n \vec{B}.\vec{I} + \vec{S}.\vec{\vec{A}}.\vec{I} + \vec{S}.\vec{\vec{D}}.\vec{S} \qquad (27)$$

This Hamiltonian is used to describe the ENDOR experiments, where a proton spin interacts with the triplet electron spin.

3.4 The Triplet state:

The triplet state is formed when the total spin of a system is 1 (S=1). There are differences between the triplet state of metal complexes and that of organic molecules. In both cases, splitting of energy level occurs without the application of an external magnetic field. This is called the zero field splitting (ZFS). In the case of metal complexes, the ZFS is dominated by the spin-orbit coupling whereas in organic molecules, dipolar interaction is predominant. In a simple molecular orbital picture the molecule in the ground state has two electrons in the HOMO and no electrons in the LUMO, the molecule in the triplet state would have an unpaired electron in both the HOMO and the LUMO orbitals with parallel spins [73]. Investigation of the triplet state will allow the HOMO and LUMO orbitals to be studied simultaneously. The energy levels in an excited triplet state are usually not populated according to the Boltzmann-law. Transitions between energy levels 0, +1 and 0, -1 may occur. This means that two EPR lines for one canonical orientation may be observable. The polarization pattern (the order of absorptive/emissive transitions observed at all 6 canonical orientations) contains general information about the mechanism of formation of the triplet state.

There are four mechanisms of triplet formation:

1. Triplet energy transfer: A molecule already in the triplet state transfers its energy to another molecule which is at a lower energy level. By this process, the energy donor reverts back to its ground state and the acceptor is lifted to its excited triplet state. This mechanism is seen in bacterial reaction centres and is called sensibilisation. [74, 75]

2. The second mechanism requires the presence of two molecules. This process is called triplet fission and involves the transfer of energy from a high energy singlet to a pair of low energy triplets over two separate molecules [76]. The transition to the triplet state is possible only if the vibronic singlet levels are higher in energy by twice the lowest electronic triplet state [76]. This mechanism has been observed in crystals of molecules like anthracene, stilbene, teracene and perylene [77, 78].

3. Intersystem crossover (ISC) [80-82]: This mechanism happens in individual molecules, i.e. a proximal molecule is not required to initiate the triplet formation. In the excited singlet state, there is a spin inversion which leads to the formation of a triplet [79]. This process is spin dependent and most notably spin orbit coupled. This mechanism is common in porphyrins (eg – zinc protoporphyrin IX) and can be identified with its polarisation pattern, AAAEEE.

4. Radical pair (RP) mechanism: In this mechanism, an electron leaves the molecule after excitation which results in formation of a radical pair in the donor and acceptor. Since the unpaired electrons are on different molecules, they experience different effective magnetic fields [83]. Since the singlet state remains virtually degenerate with the T_0 sublevel of the triplet radical pair state, a significant mixing of the S and T_0 levels occurs, in which the radical pair state oscillates back and forth between S and T_0. The T_0 radical pair state can then recombine to form the triplet state of the molecule that was excited. This mechanism is also called the S-T_0 mechanism [84]. In the radical pair mechanism the $M_S = 0$ sublevel of the molecule is exclusively populated. This implies that shortly after the laser flash and before decay processes play a role, all $T_0 \rightarrow T_{+1}$ transitions are absorptive and $T_0 \rightarrow T'_1$ are emissive and it also implies that the amplitudes of the absorptive and emissive signals are identical.

From the EPR spectrum of the triplet state, the zero field splitting parameters which describes the geometry of the triplet wave function can be read. However, only the absolute value of the tensors can be determined by this method.

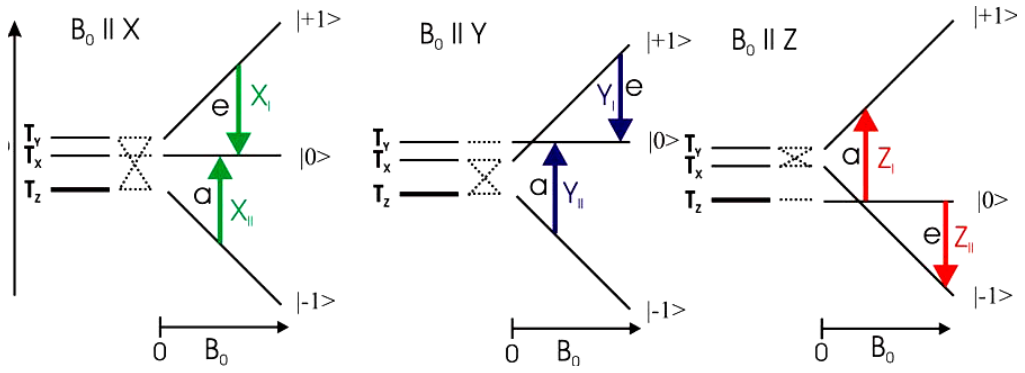

Figure 3.7 Representation of the energy levels of a triplet state (D> 0, E> 0). Sublevel Tx, Ty and Tz, due to the zero-field splitting are no longer energetically degenerate. Their occupancy depends on the spin-orbit coupling and does not follow Boltzmann distribution. In an external magnetic field, the levels, |+1> and |-1> are formed due to mixing of the sublevels. Depending upon the orientation of the molecule in the magnetic field, absorption and emission take place (which have been indicated by colored arrows). A spectrum which results from such a sub level occupation has a polarization pattern AAA EEE (zinc protoporphyrin IX and zinc chlorin).

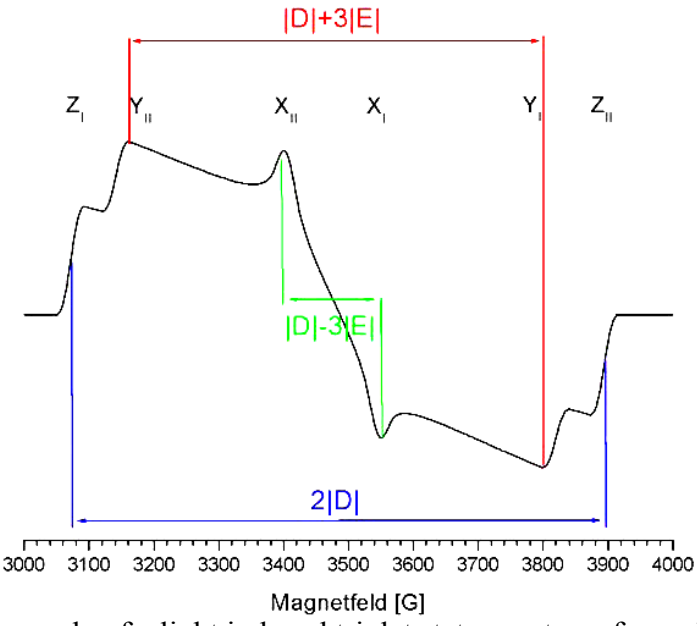

Figure 3.8 Example of a light induced triplet state spectrum formed due to the ISC mechanism. The value of the zero field splitting parameters can be read directly from the line spacing.

3.5 Pulsed EPR techniques

Pulsed EPR methods such as Fourier transform (FT) EPR and electron spin echo (ESE) spectroscopy are now the more commonly used techniques. In these techniques, the magnetization along the external field direction (z magnetization) associated with formation and decay of transient radicals is monitored by the magnetization vector in the transverse (xy) plane with one or more short microwave pulses, followed by the detection of EPR responses in the absence of the excitation magnetic field.

In pulsed EPR, the detection happens without incident microwave power. Thus the noise signal in pulsed experiments is determined by background noise of the spectrometer and is stable in the experimental conditions. The noise becomes independent of the noise of the microwave source. The measured EPR response is directly proportional to the z magnetization existing at the moment of microwave excitation. Since the excitation microwave field doesn't need to be included in the analysis model, the data analysis is simplified.

In the state of thermal equilibrium, the magnetization vector (M_z) is oriented along the z axis. A $\pi/2$ pulse along the x axis rotates M_z through $\theta = \gamma_e B_1 t_p$ (γ_e is the gyromagnetic ratio of the electron spin, 1.78×10^{11} rad S^{-1} T^{-1} , B_1 is the intensity of the microwave pulse and t_p is the pulse duration) and transforms the original longitudinal magnetization into a transverse y magnetization.

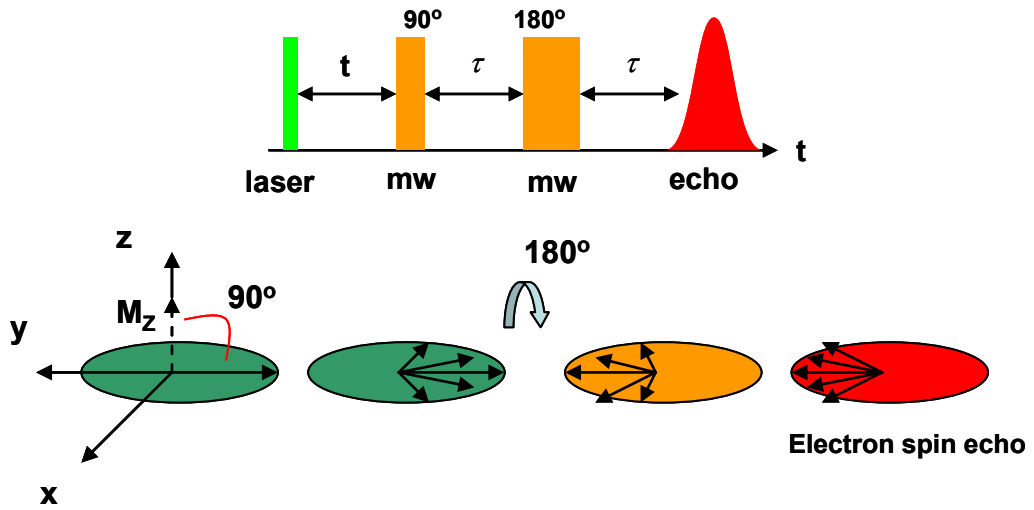

Figure 3.9 Formation of electron spin echo

The oscillating signal which decays owing to transverse relaxation is called the free induction decay (FID). The rapid decay of FID can be reversed in the spin echo experiment. This was first described by Hahn by means of non linear behaviour of a set of oscillators with different frequencies [Hahn, 1950].

3.6 Electron Nuclear Double Resonance (ENDOR)

The attraction of electron nuclear double resonance (ENDOR) spectroscopy is the possibility to measure unresolved hyperfine interactions in electron paramagnetic resonance (EPR) spectra. The ENDOR spectra not only allow for an identification of the paramagnetic center but also supply detailed information about its electronic structure. This technique combines the high resolution and nuclear selectivity of the nuclear magnetic resonance with the sensitivity of an EPR experiment. The first ENDOR experiment was described by George Feher in 1956.

In a classical CW ENDOR, a selected EPR transition is excited buy the microwave field and the radio frequency field induces nuclear transitions. These are detected by observing the desaturation of the EPR transition as a function of the radio frequency. Unfortunately, CW ENDOR is often restricted to narrow temperature ranges due to relaxation effects.

The first pulsed ENDOR was proposed by Mims and further developed by Davies. The Davies ENDOR used in this study is based on selective microwave pulses and is represented in Figure 3.11 along with the population of energy levels.

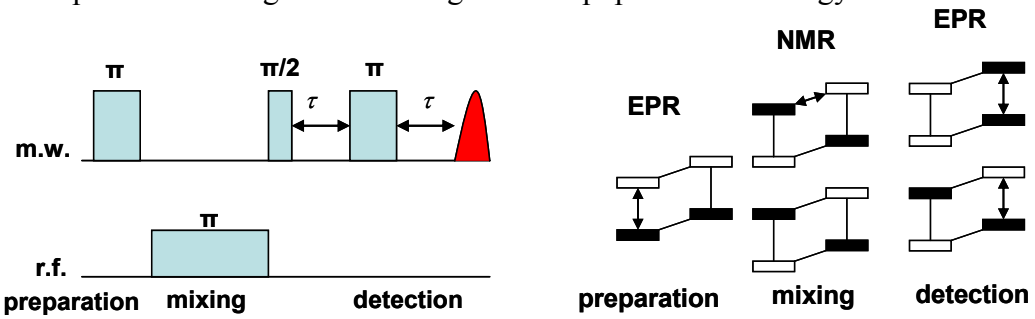

Figure 3.10 Pulse sequences of Davies ENDOR and population levels at different sequences

The polarization of EPR transition is first inverted by a microwave pulse. During the subsequent mixing period, a selective RF pulse changes the nuclear polarization. The polarization of this transition changes accordingly if the RF pulse is resonant with one of the nuclear frequencies. The nuclear polarization is transferred to electron coherence and measured via ESE during the detection period.

Applying the strong field approximation for a molecule in the triplet state, the spin Hamiltonian gives the frequency of the nuclear transitions

$$\nu_{ENDOR}^{T} = \nu_n - M_S A_T \,, \tag{28}$$

where ν_n is the nuclear Zeeman frequency and A_T is the hyperfine interaction of the triplet state. In this work, ENDOR has been measured on a laser pulse generated triplet (in situ).

3.6.1 ENDOR on triplet states

The spin Hamiltonian for a triplet state is described as,

$$H = g_e \beta_e \vec{B} \cdot \vec{S} - g_n \beta_n \vec{B} \cdot \vec{I} + \vec{S} \cdot \vec{\vec{A}} \cdot \vec{I} + \vec{S} \cdot \vec{\vec{D}} \cdot \vec{S} \tag{29}$$

β_e and β_n are the Bohr and nuclear magnetons, g_e and g_n are the g values of the electron and nucleus, $\vec{S}$ is the total electron spin, $\vec{I}$ is the nuclear spin, $\vec{\vec{A}}$ is the nuclear hyperfine tensor and $\vec{\vec{D}}$ is the zero field tensor.

In conditions of strong field approximation, the terms involving the nuclear spin operator can be neglected in comparison to the other terms. The nuclear spin transitions for a nuclear spin (I = ½), coupled to a triplet electron spin (S=1) are determined by the nuclear Zeeman and hyperfine terms of the spin Hamiltonian. For a molecule in its triplet state,

$\nu_{ENDOR}^{T} = \nu_n - M_S A_T$ (parameters explained in equation 28)

The energy levels for a proton coupled to the triplet electron are shown in Figure 3.11

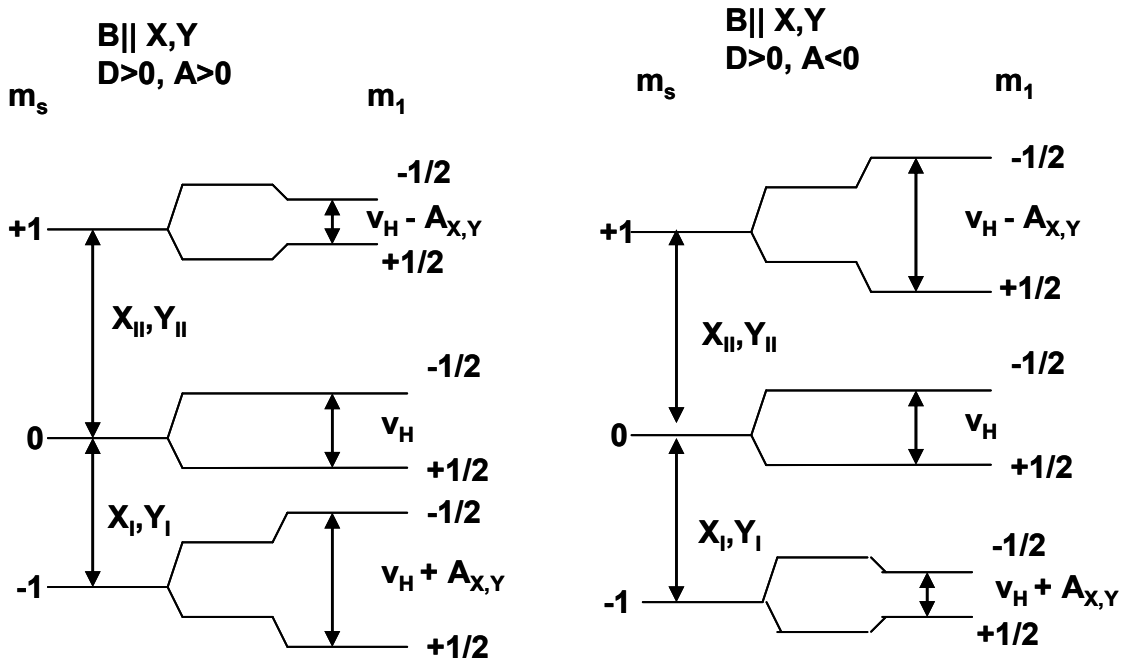

Figure 3.11Energy levels for proton coupled to the triplet electron

The frequencies of the nuclear transitions observed in ENDOR spectroscopy in the presence of hyperfine interaction with respect to nuclear Zeeman frequency can be read from the spectra according to equation (19).If $A_T > 0$, the larger nuclear transition frequency occurs in the $M_S = -1$ triplet sublevel and the smaller transitions occur in the $M_S = +1$ sublevel. No hyperfine interaction is present in the $M_S = 0$ triplet sublevel and the ENDOR frequency occurs at the nuclear Zeeman frequency $\nu_n(^1H)$. For triplet ENDOR measurements with a magnetic field resonant with the $M_S = 0 \leftrightarrow -1$ transition a sharp band from the $M_S = -1$ manifold is thus expected at $\nu_n(^1H)+A_T$ for $A_T > 0$ and vice versa for $A_T < 0$. An opposite hyperfine shift is observed for the $M_S = +1$ manifold. The sign of the hyperfine coupling A_T with respect to that of the zero field splitting parameter D is therefore directly obtained from the ENDOR spectrum.

The signs of the hyperfine couplings are essential information about the spin system. Especially important is the sign of the isotropic coupling (a_{iso}), which depends on the mechanism of the hyperfine interaction. For α-protons in π-radicals, which are coupled by the exchange mechanism (π-σ spin polarization), a negative sign of A_{iso} is typically observed, while a positive sign is an indication of the hyperconjugation mechanism and characteristic for β−protons as found in methyl or methylene groups. Hence, the sign of the hyperfine couplings does not only contain important information for an in-depth analysis of the ENDOR spectra, it gives important structural information.

3.6.2 Goutermann orbitals

The Q and B bands in the absorption spectra of chlorophylls belong to the chlorin base and they are similar for many porphyrins. They can be described theoretically in a simple way by only four orbitals as originally proposed in a model by Gouterman. [106, 107] The four MOs that are principally involved in these transitions are the two highest occupied MOs (HOMO-1, HOMO) and the two lowest unoccupied MOs (LUMO, LUMO+1) in the ground state molecule. The Gouterman orbitals are shown in Fig. 3.12A and an energy level scheme is shown in Fig. 3.12B. In D_{4h} symmetry, valid for protoporphyrin without ring substituents, the HOMO orbitals have symmetry a_{1u} and a_{2u} and the LUMO orbitals have symmetry e_g. Upon symmetry lowering towards approximate C_{2v} symmetry, the orbitals a_{1u} and a_{2u} transform as a_2 and b_1 and by taking appropriate linear combinations of the e_g orbitals, two new unoccupied orbitals are constructed that also transform as a_2 and b_1. Especially the two LUMO orbitals become non-degenerate and thus give rise to the B band and Q band in the visible absorption spectrum. [104, 105, 107]

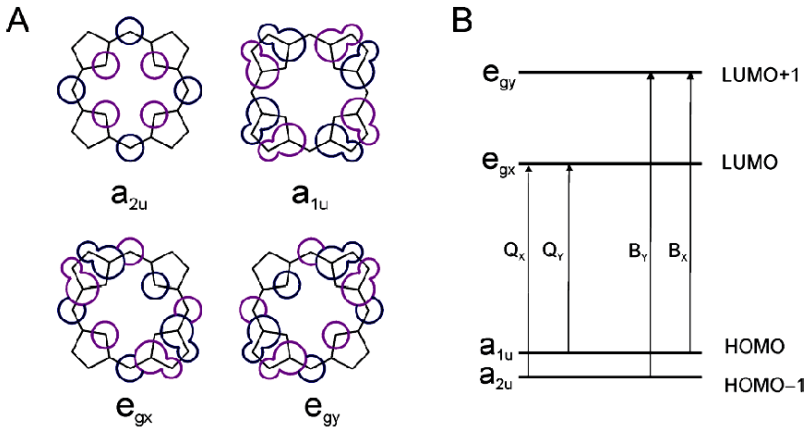

Figure 3.12 (A) Schematic representation of Goutermann orbitals (B) Energy levels

3.6.3 Electron spin density distribution and hyperfine couplings in the triplet state

The triplet state in a simple model is described via HOMO → LUMO excitation and one unpaired electron is present in each of the HOMO and LUMO orbital. However, the HOMO-1 orbital is also nearby in energy, and the triplet state may also contain contributions from HOMO-1 → LUMO excitation. Because of the near-degeneracy of the HOMO and HOMO-1 orbitals, DFT cannot be expected to reproduce the mixing to these orbitals. In order to theoretically investigate the triplet wave function with respect to participation of the HOMO, HOMO-1 and LUMO, unpaired electrons have been redistributed over the set of frontier orbitals (HOMO-1, HOMO, and LUMO, LUMO + 1). The spin density ρ_π for any combination of HOMO → LUMO and HOMO-1 → LUMO excitation can be then calculated using the equation

$$\rho_\pi = \cos^2\varphi\rho_{H,L} + \sin^2\varphi\rho_{H-1,L} \qquad (30)$$

where $\rho_{H,L}$ and $\rho_{H-1,L}$ are the spin densities from calculations with pure HOMO → LUMO and HOMO-1 → LUMO excitation, respectively, and φ determines the amount of mixing; φ=0 corresponds exclusively to HOMO → LUMO excitation, φ=90 to a HOMO-1→LUMO excitation. Due to the proportionality of isotropic hyperfine coupling constants of methyl group protons and β protons to the electron spin density on the adjacent carbon atom, [108] the calculation of hyperfine coupling constants for any

combination of HOMO → LUMO and HOMO-1 → LUMO excitation is performed using a similar equation,

$$A(^1H) = \cos^2\varphi A_{H,L} + \sin^2\varphi A_{H-1,L}(^1H) \quad (31)$$

For the in-plane methine protons, spin polarization is responsible for the isotropic hyperfine coupling constants. It also plays a minor role for the hyperfine couplings of the other protons, but it is the dominant effect for the methine (meso) protons. Since spin polarization involves the polarization of the orbitals of an electron pair in a doubly occupied orbital of lower energy, it is not taken into account correctly in calculations upon mixing of the frontier orbitals. In order to calculate the isotropic couplings for the methine protons, additional calculations have been performed using spin-unpolarized orbitals derived from a calculation of the singlet ground state. The triplet π spin density for HOMO → LUMO and HOMO-1 → LUMO excitation was then recalculated from the spin-unpolarized molecular orbitals by computing the spin densities based on the unpolarized orbitals. Subsequently, equation (1) was used to obtain the unpolarized triplet spin density for an arbitrary mixture of HOMO → LUMO and HOMO-1 → LUMO excitation. Finally, isotropic hyperfine coupling constants for the methine protons, a_H, were calculated using McConnell's relation [108, 109]

$$a_H = Q\rho_\pi \quad (32)$$

where Q is a proportionality factor and has a value of -63 MHz, [48, 49] and ρ_π is the spin density on the adjacent carbon atom.

CHAPTER 4: CRYSTALLIZATION OF RECONSTITUTED MYOGLOBIN

Extensive research has been carried out to obtain single crystals of reconstituted myoglobin. Since single crystal EPR forms an integral part of this thesis work, several myoglobins have been subjected to extensive screening techniques to obtain single crystals. In this chapter, a comprehensive introduction to protein crystallization, screening methods and crystallization of horse heart myoglobin reconstituted with the zinc protoporphyrin IX cofactor are described.

4.1 Introduction to protein crystallography

A detailed description of protein crystallography is beyond this thesis and can be found in relevant textbooks [Blundel and Johnson, 1994; Drenth, 1994; Massa, 1994].

4.1.1 Theoretical background

The maximum attainable resolution of any microscopic technique is limited by the applied wavelength. The radiation needed to analyze atomic distances lies in the range of X-rays. Electron microscopy uses an array of lenses to merge the waves diffracted by an object to enlarge it. However, there is no such set up available for magnification of the X-rays. Max von Laue in 1912 realized that the three dimensional ordered lattice arrangements in crystals will cause interference of the diffracted photons resulting in discrete maxima whose intensity can be measured with an appropriate experimental setup.

4.1.2 Crystal growth

The process of crystal formation is in principle thermodynamically favoured, driven by the gain of entropy through the loss of the proteins ordered hydration shell. A solution of the protein is slowly brought into a state of supersaturation (usually by evaporation of water) until ordered crystals are formed.

Mechanistically, the crystallization process can be divided into two stages, seed formation and crystal growth. Supersaturation of the system – defined as the difference of the chemical potentials of solution and crystal – is a prerequisite for both the stages. Seed formation occurs in equilibrium of formation and dissolving of small aggregates, determined by the free energy ΔG. It will have a maximum at critical radius, meaning that aggregates with a radius smaller than the critical radius will redissolve, while for those bigger than the critical radius, further crystal growth means a decrease of ΔG. The critical cluster size for a protein crystal is between 10 and 200 molecules.

4.1.3 Crystals

A crystal can be regarded as a three dimensional repetition of a single building block, the unit cell. Within the unit cell, a crystal can further contain further symmetry elements, dividing it into several asymmetric units, which form the most basic structural element within the crystal. The geometry of the unit cell together with the possible symmetry operations defines the space group of the crystal. Although there are 230 space groups in seven crystal systems (triclinic, monoclinic, orthorhombic, tetragonal, trigonal, hexagonal and cubic), only 65 are enantiomorphic and thus feasible for molecules such as proteins. Identification of the correct space group is essential for correct indexing of the diffraction patterns and therefore the first step to understand a crystal structure.

4.2 Materials and methods

4.2.1 Protein samples

Native horse heart myoglobin was purchased from Sigma and used without further purification. Myoglobin from Porpoise (*Phocoena phocoena)*, Atlantic white sided dolphin (*Lagenorhynchus acutus*) and Bottle nose dolphin (*Tursiops truncatus*) was extracted by procedures mentioned in chapter 2 of this thesis. The proteins were not stored for a long time and immediately after purification they were subjected to reconstitution with various chlorophyll model systems. The reconstituted protein was prepared by protocols mentioned earlier and samples in various buffers were prepared by dialysis with the respective buffer and further by using a spin membrane apparatus with molecular weight cut off smaller than the protein size. The reconstituted myoglobins were

purified using pre packed PD-10 columns and used immediately for crystallization without freezing or lyophyllization.

4.2.2 Chemicals

All the chemicals used for crystallization were of highest purity. Triple distilled water was used to make the ammonium sulfate solutions and buffers for screening were purchased from Hampton research. The micro batch plates, hanging drop set ups and sitting drop plates were all purchased from Hampton research.

4.2.3 Vapor diffusion

The most commonly used methods for protein crystallization are the hanging drop and the sitting drop methods which fall under the category of vapour diffusion. Both entail a droplet of the purified protein, buffer and precipitant being allowed to equilibrate with a larger reservoir containing the similar buffer and precipitant in higher concentrations.

Initially the protein droplet contains insufficient concentration of the precipitant that is required for crystallisation, but as water vaporizes from the drop and transfers to the reservoir, the precipitant concentration increases to a level that is optimal for crystallisation.

Diagram of hanging drop:

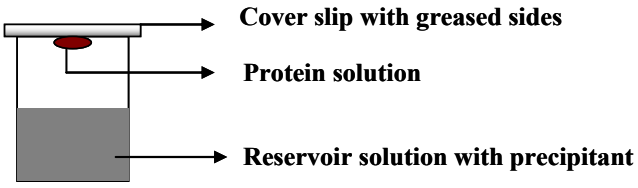

Diagram of sitting drop:

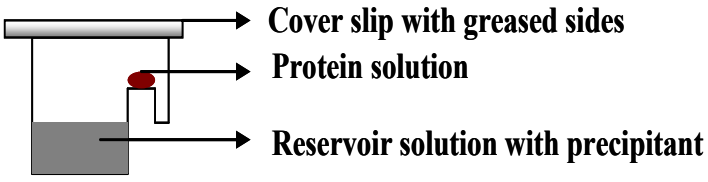

Fig 4.2 Representation of hanging drop and sitting drop technique of crystallization

The reservoir solution (blue) contains the buffer and the precipitant. The protein solution (red) contains the same compounds but in a lower concentration.

4.2.4 Data collection and analysis

A preliminary X-ray diffraction experiment was carried out using a CCD detector (Bruker AXS X8 Proteum) and a Cu K_ rotating anode source with Montel mirror optics (2.4 kW). Diffraction images were indexed and integrated with the PROTEUM program and subsequently scaled and truncated using the CCP4 suite (Collaborative Computational Project, Number 4, 1994). A complete native data set was collected at 100 K using beamline BL14.1 at BESSY II (Berlin, Germany). The detector was a MAR Mosaic 225. 843 frames were collected with 10 s exposure time and 0.2^{o} oscillation. The distance between the crystal and the detector was maintained at 190 mm. In order to collect the data at cryogenic temperature, the crystal was frozen in liquid nitrogen and mounted on the goniostat under a nitrogen-gas stream at 100 K. The data set was indexed and integrated using the program MOSFLM (Leslie, 1992). Scaling was carried out with SCALA (Collaborative Computational Project, Number 4, 1994).

4.3 Dynamic light scattering (DLS)

To arrive at the optimum conditions for growing the crystals, it is first essential to know the physical properties of the protein in the solution. These properties highly depend on the pH of the residing buffer which in turn affects the aggregation of the protein. A pH close to the pI value of a protein will cause protein aggregation. For crystal formation, it is essential that the protein resides in a homogenous mono dispersed phase. All myoglobins do not crystallize in the same conditions as reported for the sperm whale myoglobin. Hence, it is essential to screen these proteins for their behavior in various pH ranges. Since the dolphin myoglobins have a very close amino acid sequence resemblance with the sperm whale myoglobin, these were chosen for screening by the DLS method.

4.3.1 Introduction to DLS

When a beam of light passes through a colloidal dispersion, the particles or droplets scatter some of the light in all directions. When the particles are very small compared with the wavelength of the light, the intensity of the scattered light is uniform in all directions (Rayleigh scattering); for larger particles (above approximately 250nm diameter), the intensity is angle dependent (Mie scattering).

If the light is coherent and monochromatic, as from a laser for example, it is possible to observe time-dependent fluctuations in the scattered intensity using a suitable detector such as a photomultiplier capable of operating in photon counting mode.

These fluctuations arise from the fact that the particles are small enough to undergo random thermal (Brownian) motion and the distance between them is therefore constantly varying. Constructive and destructive interference of light scattered by neighboring particles within the illuminated zone gives rise to the intensity fluctuation at the detector plane which, as it arises from particle motion, contains information about this motion. Analysis of the time dependence of the intensity fluctuation can therefore yield the diffusion coefficient of the particles from which, via the Stokes Einstein equation,

knowing the viscosity of the medium, the hydrodynamic radius or diameter of the particles can be calculated [88, 89].

Particle size distributions can be calculated either assuming some standard form such as log-normal or without any such assumption. In the latter case, it becomes possible, within certain limitations, to characterize multimodal or skewed distributions. The size range for which dynamic light scattering is appropriate is typically submicron with some capability to deal with particles up to a few microns in diameter. The lower limit of particle size depends on the scattering properties of the particles concerned (relative refractive index of particle and medium), incident light intensity (laser power and wavelength) and detector / optics configuration [89, 90].

4.3.2 DLS on dolphin myoglobins

DLS experiments on myoglobins (Atlantic white head dolphin: UT 59 and Bottle nose dolphin: UT 60) was carried out in DESY, Hamburg. A laser spectroscatter 201 instrument was used to measure the proteins in a cuvette and a laser spectroscatter 501 was employed to measure DLS directly on the hanging drop. Samples of myoglobin were prepared in different pH buffers and the concentration was maintained at an optimum 20mg/ml. The protein concentration and buffer was a resultant of previous screening results. 20mM Tris buffer in pH (7.0, 7.5, 8.0, 8.5 and 9.0) was used for both the myoglobins.

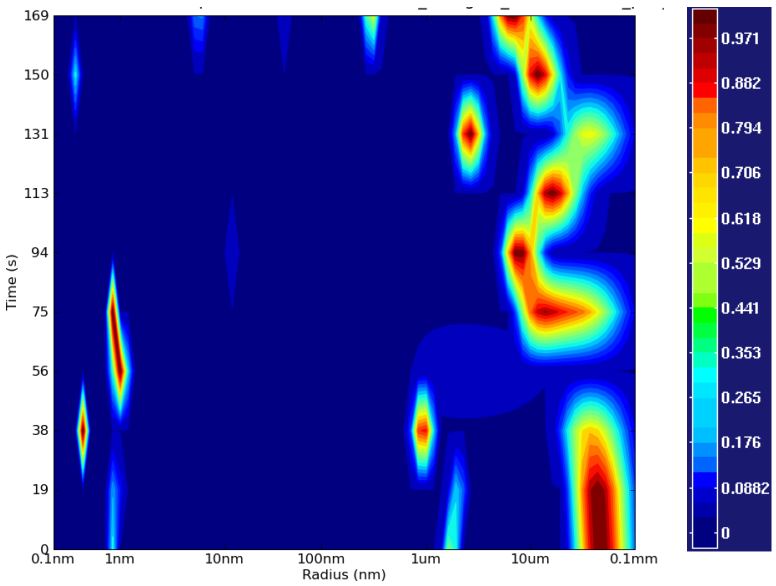

Figure 4.3 Non centrifuged sample of UT 59, pH 7.0 and density reference

Fig 4.3 is the radius distribution versus time plot of UT 59 and the density of the different particles are indicated by colors. This measurement indicates the presence of particles of size 0.1mm which are probably dust. This can be eliminated by centrifuging the sample for 20 minutes at 14500 RPM.

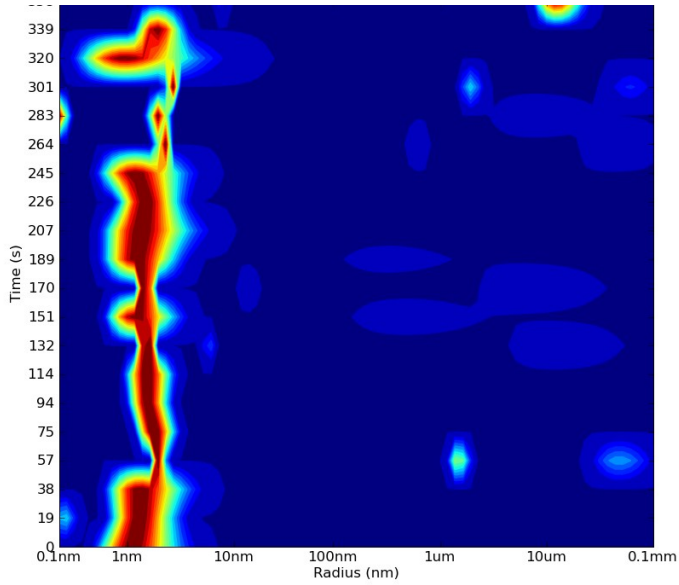

Figure 4.4 UT 59, pH 7.0, centrifuged for 20 minutes.

The presence of protein in the mono dispersed phase is indicated by a clean deep red band without much variation in radius distribution with respect to time. Figure 4.4 already indicates a better condition when compared to Figure 4.3.

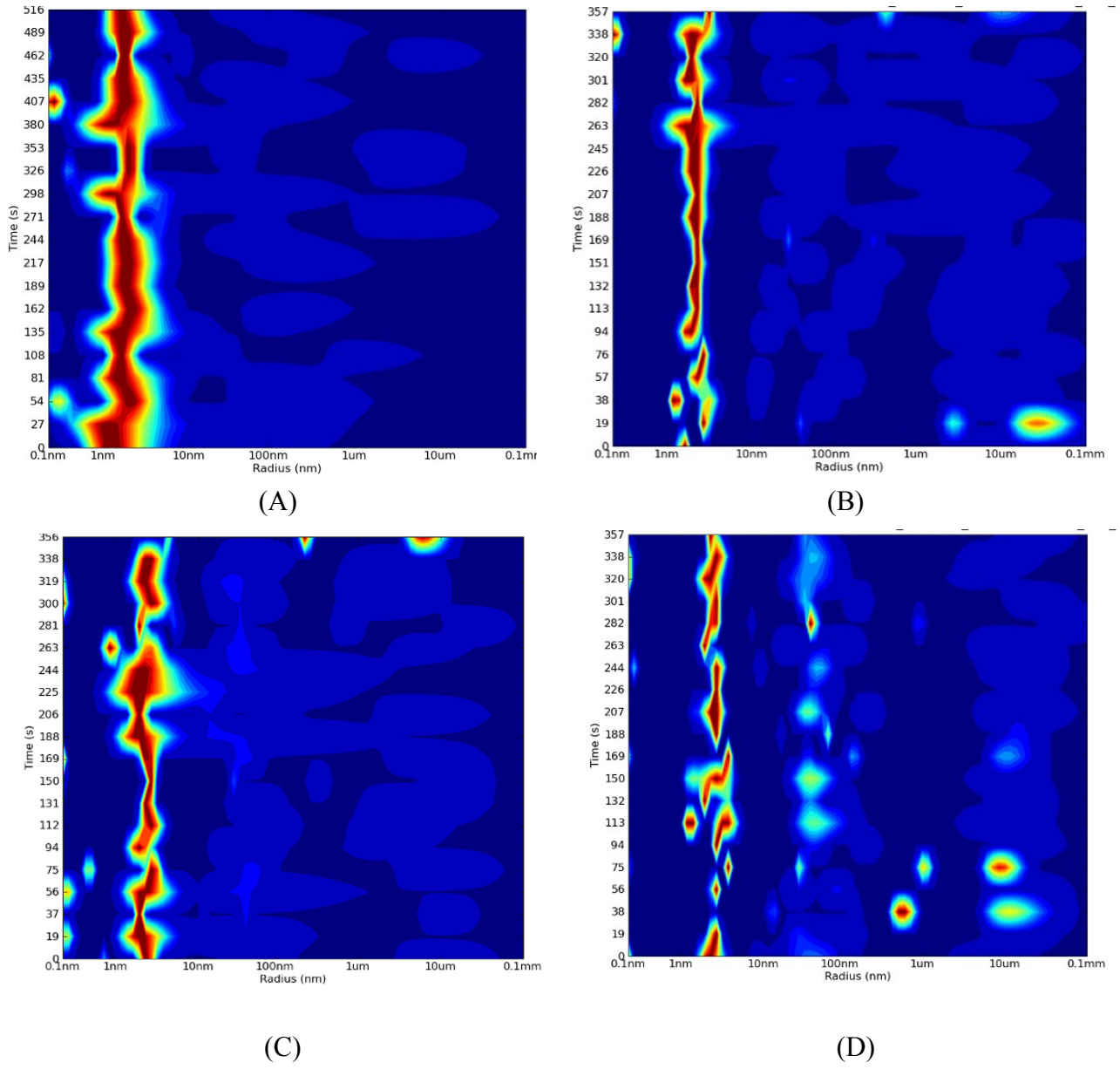

Figure 4.5 Myoglobin UT 59, (A) – pH 7.5, (B) – pH 8.0, (C) – pH 8.5, (D) – pH 9.0

From Figure 4.5 it is evident that myoglobin UT 59 is present in its mono dispersed homogenous phase at pH 7.5. When the pH increases close to the pI value, one can clearly the see the formation of aggregates with bigger particle radius coexisting with the initial mono dispersed band.

DLS studies were also carried out on myoglobin UT 60. The results are shown in Figure 4.6.

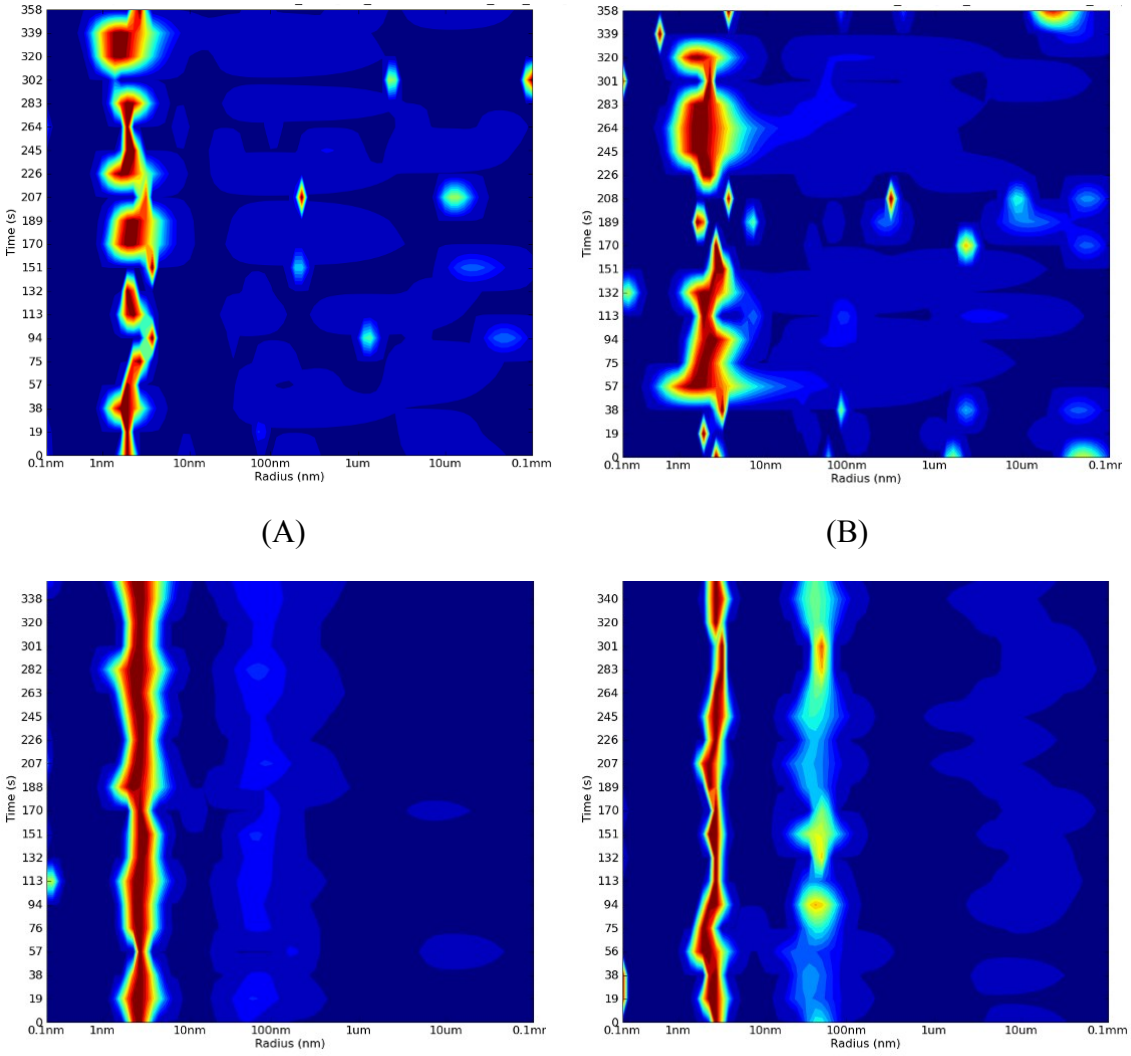

Figure 4.6 Myoglobin UT 60, (A) – pH 7.0, (B) – pH 7.5, (C) – pH 8.0, (D) – pH 9.0

From figure 4.6 it is evident that myoglobin UT 60 starts to form aggregates between pH 7.5 and 8.0 and at pH 8.0 there is a consistent aggregate band with respect to time. Comparing these results with myoglobin UT 59, it can be concluded that UT 59 in pH 7.5 is in perfect mono dispersed homogenous condition. Using these conditions we were able to get micro crystals of UT 59 in its native form.

4.4 Crystal structure of zinc protoporphyrin IX-myoglobin

We were able to obtain crystals of zinc protoporphyrin IX-myoglobin by the hanging drop method of crystallization. Well ordered crystals were formed in 20 µl drops against a reservoir solution of 3.5 M ammonium sulphate. The drop contained 10 µl of the protein (20 mg/ml) and 10 µl of the reservoir solution. The crystals were grown at 4 degree Celsius and in dark.

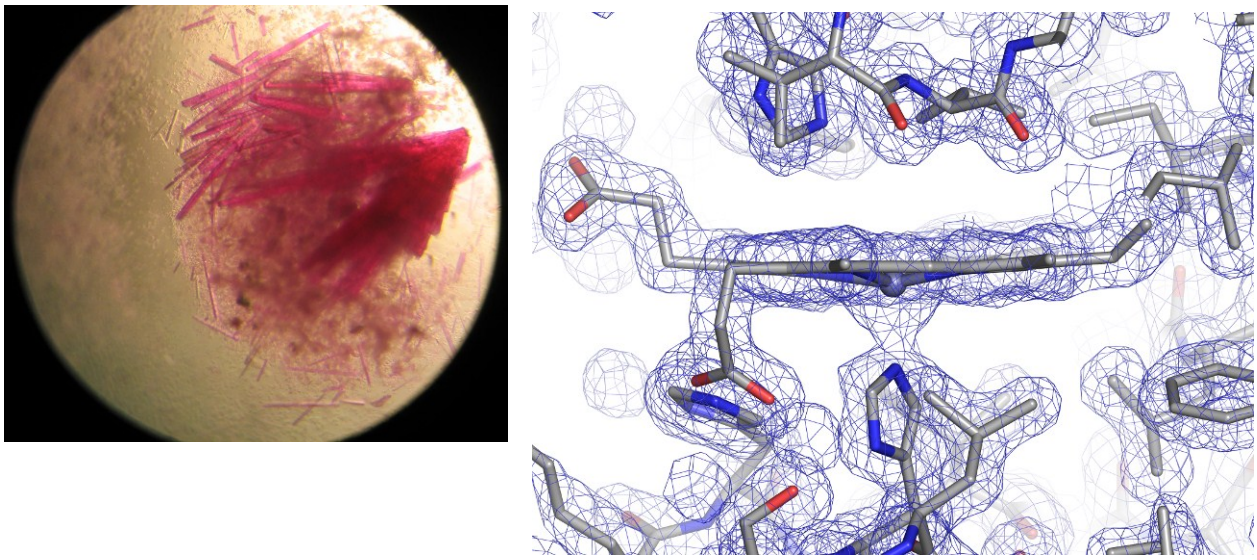

(A) (B)

Figure 4.7 (A): Crystals of ZnPPIX-Mb as seen under the microscope. Crystals of nearly 700 µm could be obtained. (B) The electron density fitting of diffraction data, showing the orientation of ZnPPIX in the protein matrix.

The crystals diffracted to 1.8 Å at the synchrotron facility at BESSY II, Berlin. The diffraction data is given in table 4.1

	Zn-Mb
Data collection	
X-ray source	BESSYII BL14.2
Wavelength (Å)	0.91841
Space group	P21
Unit-cell parameters (Å)	42.76, 30.49, 56.54
β (°)	98.40
Resolution (Å)	31.59-1.80 (1.85-1.80)
No. of observed reflections	52608
No. of unique reflections	13611
Rmerge	0.042 (0.177)
Completeness (%)	99.6 (99.6)
<I/σ(I)>	22.2 (7.0)
Refinement	
Resolution	31.59-1.80
R (%)	15.6
Rfree (%)	22.6
No. of water in ASU	146
No. of Sulfate molecule	2
Rmsd bond lengths (Å)	0.023
Rmsd angles (°)	2.01
Ramachandran plot	
favoured region (%)	96.0
allowed region (%)	4.0
outlier region (%)	0.0

Table 4.1 Diffraction data for ZnPPIX-Mb

The unit cell dimension was $P2_1$ and this was found to be the same as the unit cell of native horse heart myoglobin crystals. The native horse heart myoglobin was also crystallized in similar conditions and its until cell was determined with X-ray diffraction. The protein folding and the orientation of the ZnPPIX cofactor in the reconstituted myoglobin were also same as compared to the native horse heart myoglobin structure published earlier [32].From the unit cell, we can conclude that there are two orientations of ZnPPIX present, both being 180^o to each other. The structure of ZnPPIX-Mb is shown in figure 4.8.

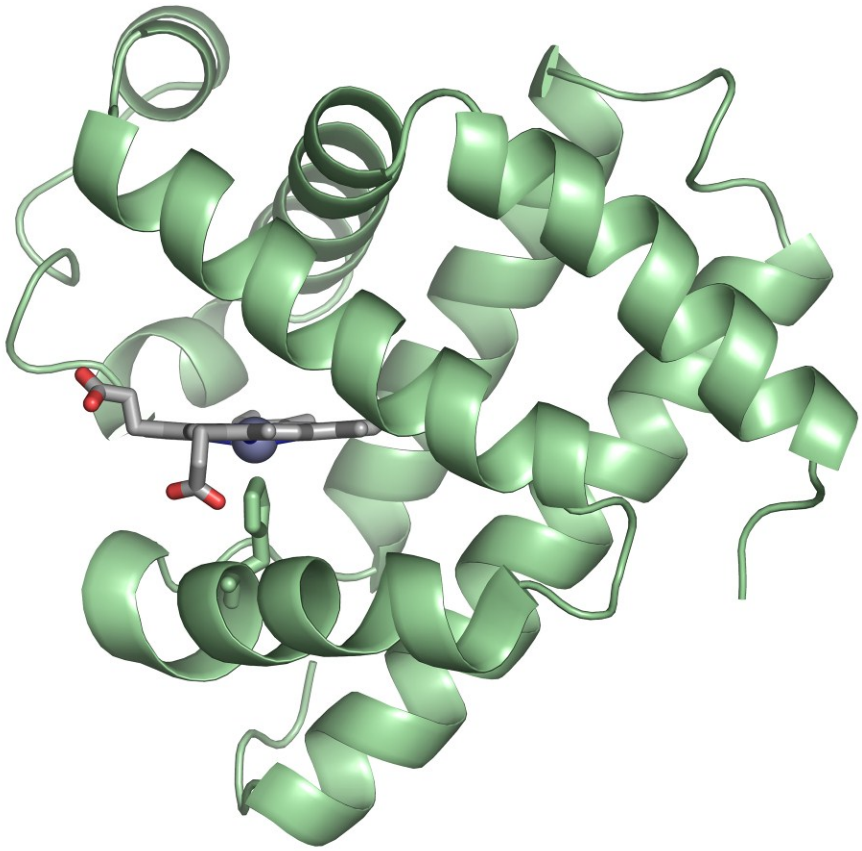

Figure 4.8 Structure of ZnPPIX-Mb showing the folding of α helices and the orientation of ZnPPIX cofactor.

CHAPTER 5: RESULTS AND DISCUSSION

5.1 Zinc protoporphyrin IX

5.1.1 Pulsed EPR

The echo detected pulsed EPR spectrum of zinc protoporphyrin IX has been obtained under three different conditions and the results are compiled below. The EPR spectrum of zinc protoporphyrin IX in DMSO is shown in Fig 5.1a and has a polarization pattern of AAA EEE and ZFS tensors |D| = 1049 MHz and |E| = 190 MHz. These results are consistent with the previously published values by Hoffmann et.al [91] (|D| = 1049 MHz, |E| = 198 MHz). Fig 5.1b represents the EPR spectrum of zinc protoporphyrin IX in pyridine. The polarization pattern remains unaffected but one can see a change in the resolution of the polarization pattern. The transitions are well defined in pyridine than in DMSO. However, there is a persistent radical signal in the pyridine spectrum. The radical signal increases with time and the triplet echo intensity is decreased. Simulation could not reproduce the spectrum exactly and hence the g-values could not be read with accuracy.

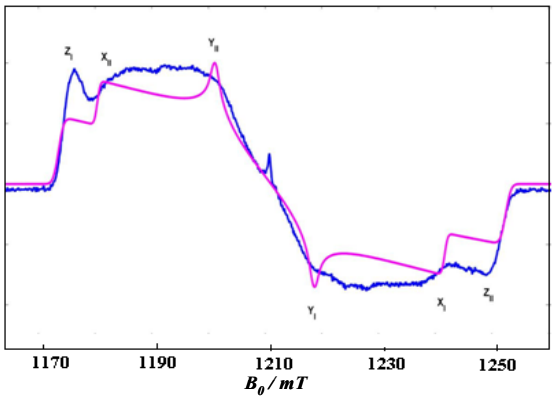

5.1a

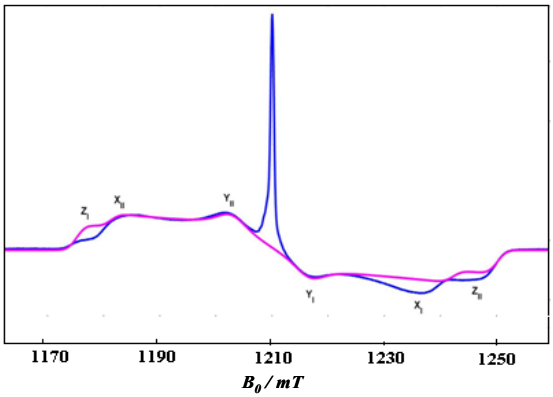

5.1b

Figure 5.1a – Pulsed EPR spectrum of ZnPPIX – DMSO and Figure 5.1b – Pulsed EPR spectrum of ZnPPIX in pyridine. The microwave frequency was 33.383 ± 0.05 GHz and microwave attenuation was 8 dB. The length of the π/2 pulse was 40 ns and the π pulse was 80 ns. Laser power was 10 mJ/pulse at 532 nm and temperature was 30 K. The accumulation time was 30 minutes per spectra.

When zinc protoporphyrin IX is reconstituted with myoglobin and then subjected to pulsed EPR, the spectrum displays well resolved spin polarization of AAA EEE. The spectrum is shown in Fig 5.1c and has a small radical signal which does not increase with time. The simulations fit well and the ZFS tensors |D| = 1081 MHz and |E| = 216 MHz fall in the range of the published values by Hoffmann et.al [91] (|D| = 1046 MHz, |E| = 207 MHz). Due to field dependent perturbation of ESE intensity originating from the interaction between nuclear spin and electron spin (similar to ESEEM effect), the polarization intensities cannot be reproduced exactly in the simulations.

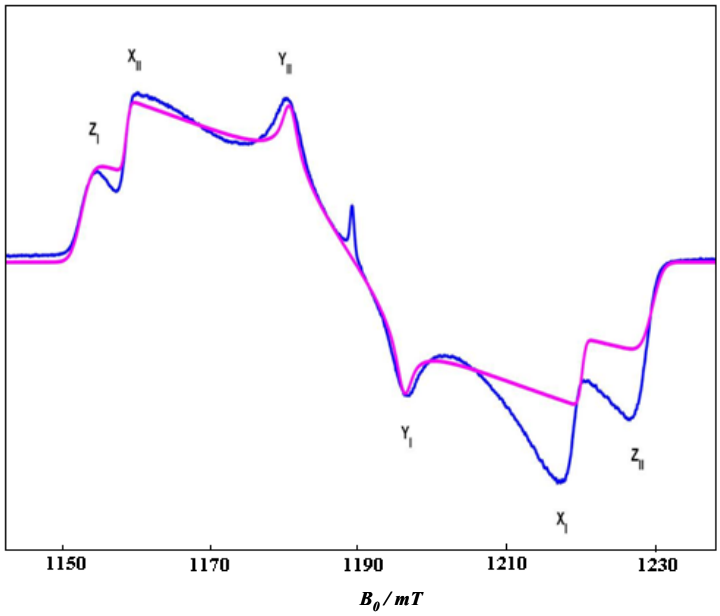

5.1c – Pulsed EPR spectrum of ZnPPIX-Mb. The microwave frequency was 33.383 ± 0.05 GHz and microwave attenuation was 10 dB. The length of the π/2 pulse was 40 ns and the π pulse was 80 ns. Laser power was 10 mJ/pulse at 532 nm and temperature was 30 K.

5.5.2 Davies ENDOR

Figures 5.1d and 5.1e show a comparison between the ENDOR spectra obtained at single crystal like positions from zinc protoporphyrin IX in pyridine and horse heart myoglobin. All traces were accumulated for 4 hours and one can observe the remarkable change in resolution and intensity of the ENDOR spectra when the cofactor is inside myoglobin.

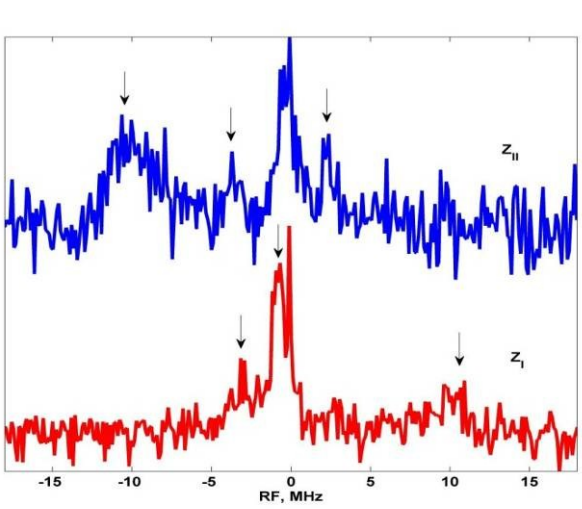

5.1d

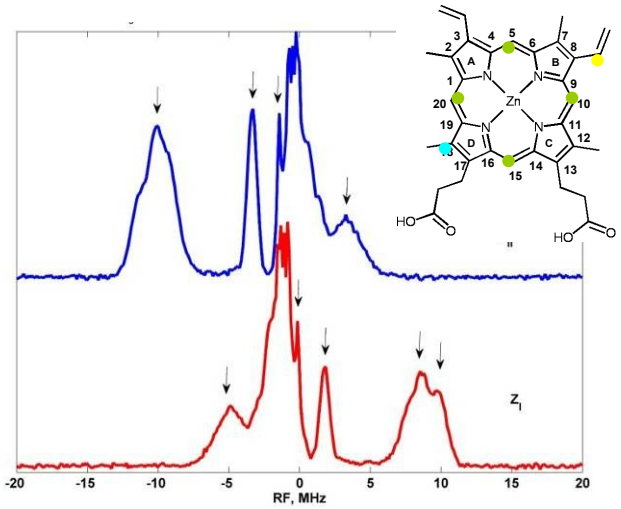

5.1e

5.1d – Davies ENDOR spectra of single crystal like positions of ZnPPIX in pyridine and 5.1e – Davies ENDOR spectra of single crystal like positions of ZnPPIX-Mb. A weak selective microwave pulse was used for preparation (pulse length 300 ns, t = 1μs) and a standard Hahn echo scheme was used for detection (pulse sequence π/2 - π with pulse lengths 150 and 300 ns, τ = 440 ns). The detection pulses were applied 2 μs after the end of the radio frequency π pulse of 20μs length. Microwave attenuation was 10 dB for the pyridine sample and 14 dB for the Mb sample. Temperature was 30 K and excitation was with laser at 532 nm and 10 mJ/pulse.

Differences in hyperfine couplings are not apparent, however. The hyperfine couplings have been assigned with the help of DFT calculations, tabulated in table 5.2. The large negative couplings, typically in the range of -9 to -10.5 MHz, arise from the in plane *meso* hydrogens in position 5, 10, 15 and 20 of the zinc protoporphyrin IX. The large positive coupling, +3.3 and +4.9 MHz in this case, arises from the free rotating methyl group at position 7 and position 18 respectively. The hyperfine couplings of 2-CH_3 and 12-CH_3 have been identified as -1.0 MHz and -0.7 MHz respectively. The ENDOR spectra from other orientations of ZnPPIX-Mb are shown in figure 5.1f. Hyperfine couplings from the Y and X orientations were taken into account for the calculation of A_{iso}, which was then assigned to respective protons based on DFT calculations.

Position	Assigned coupling (A_{iso}), MHz
5-H, 10-H, 15-H, 20-H	-9.8, -9.6, -10.3 -10.5
8^2-CH_2	-2.9
2-CH_3, 12-CH_3	-1.0, -0.7
3^2-CH_2	+0.4
18-CH_3	+4.9
7-CH_3	+3.3

Table 5.2 – Assigned hyperfine couplings of various protons of ZnPPIX in myoglobin matrix.

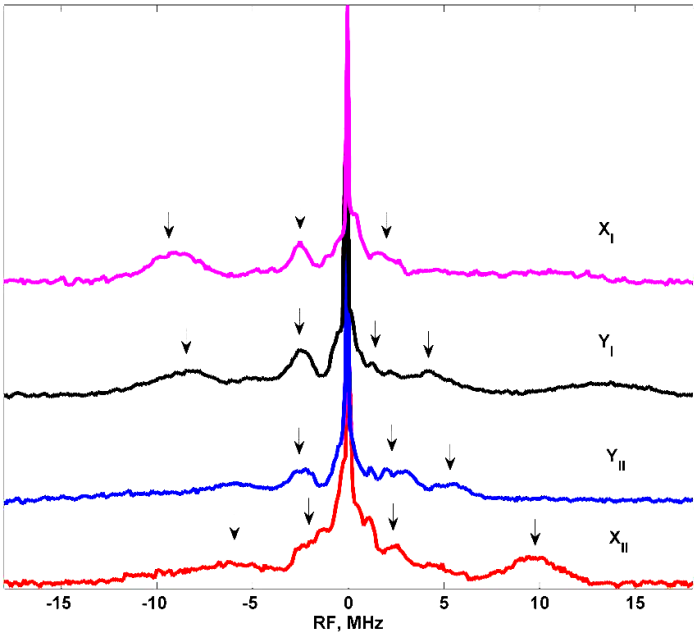

Figure 5.1f – ENDOR spectra from other polarization positions in the EPR spectrum of ZnPPIX-Mb

5.2 Zinc chlorin

5.2.1 Pulsed EPR

Zinc chlorin is the only water soluble model system that has been investigated. The solubility arises from the presence of three carboxylic groups which increase the polarity of the molecule. Echo detected EPR spectra of zinc chlorin in various environments have been summarised below and one can observe a steady increase in the |D| with change in environment from non polar to polar to protein. The g values however show close resemblance. Figure 5.2a and 5.2b represent the spectrum of zinc chlorin in pyridine and aqueous MES buffer respectively. The polarisation pattern is unaffected (AAA EEE) and the solvent plays no role in polarisation resolution in comparison with the zinc protoporphyrin IX system.

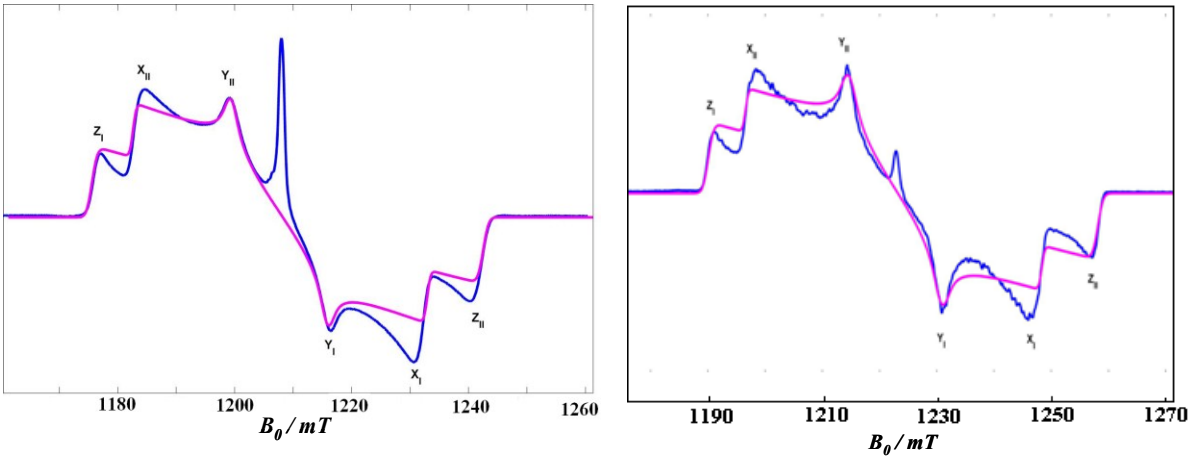

5.2a 5.2b

Figure 5.2a – Pulsed EPR spectrum of Zn Chlorin in pyridine and 5.2b – Pulsed EPR spectrum of Zn Chlorin in aqueous MES buffer-glycerol. The microwave frequency was 33.383 ± 0.05 GHz and microwave attenuation was 4 dB. The length of the π/2 pulse was 40 ns and the π pulse was 80 ns. Laser power was 10 mJ/pulse at 532 nm and temperature was 30 K. The accumulation time was 30 minutes per spectra.

The radical signal in 5.2a behaves similar to the condition described above for the ZnPPIX system. In aqueous MES buffer, though there is a persistent radical signal, it does not increase with time and interfere with the triplet echo intensity. When zinc chlorin is inserted into myoglobin, there is absolutely no formation of the radical signal. There is however a marked increase in the |D| value compared to other environments. The EPR spectrum of zinc chlorin in horse heart myoglobin is shown in figure 5.2c.

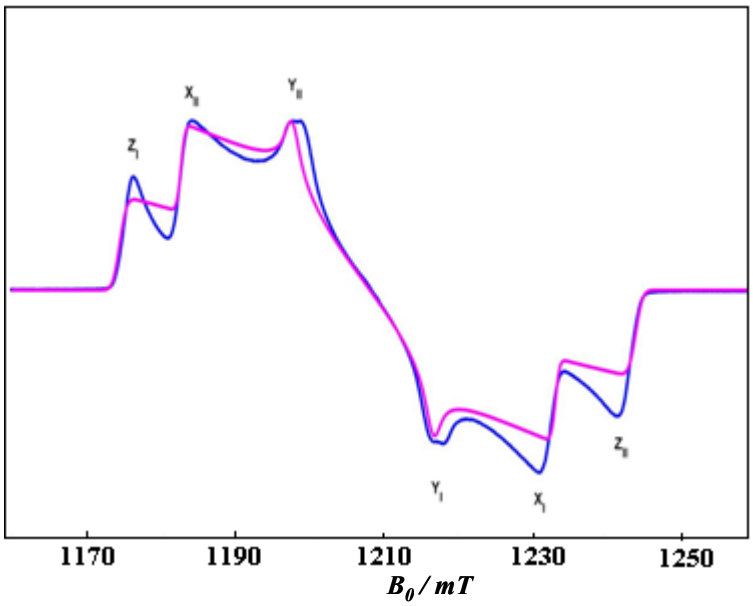

Figure 5.2c – Pulsed EPR spectrum of Zn Chlorin-Mb The microwave frequency was 33.383 ± 0.05 GHz and microwave attenuation was 8 dB. The length of the π/2 pulse was 40 ns and the π pulse was 80 ns. Laser power was 10 mJ/pulse at 532 nm and temperature was 30 K. The accumulation time was 30 minutes for this spectrum.

It has previously been published that the chlorophyll molecules tend to form aggregates in organic solvents [93], which explains the decreased value of |D|. The aqueous system lies in between the two values indicating a lesser aggregation number as compared to pyridine.

Zn Ce_6	|D| MHz	|E| MHz	g_x	g_y	g_z
Pyr	**938**	**158**	**2.0045**	**2.0044**	**2.0027**
MES	**954**	**166**	**2.0043**	**2.0042**	**2.0025**
Mb	**974**	**147**	**2.0044**	**2.0043**	**2.0027**

Table 5.3 ZFS parameters and the g tensors of Zn Chlorin in various systems.

5.5.2 Davies ENDOR

The ENDOR spectra of zinc chlorin in pyridine and in horse heart myoglobin are show in figures 5.2d and 5.2e respectively.

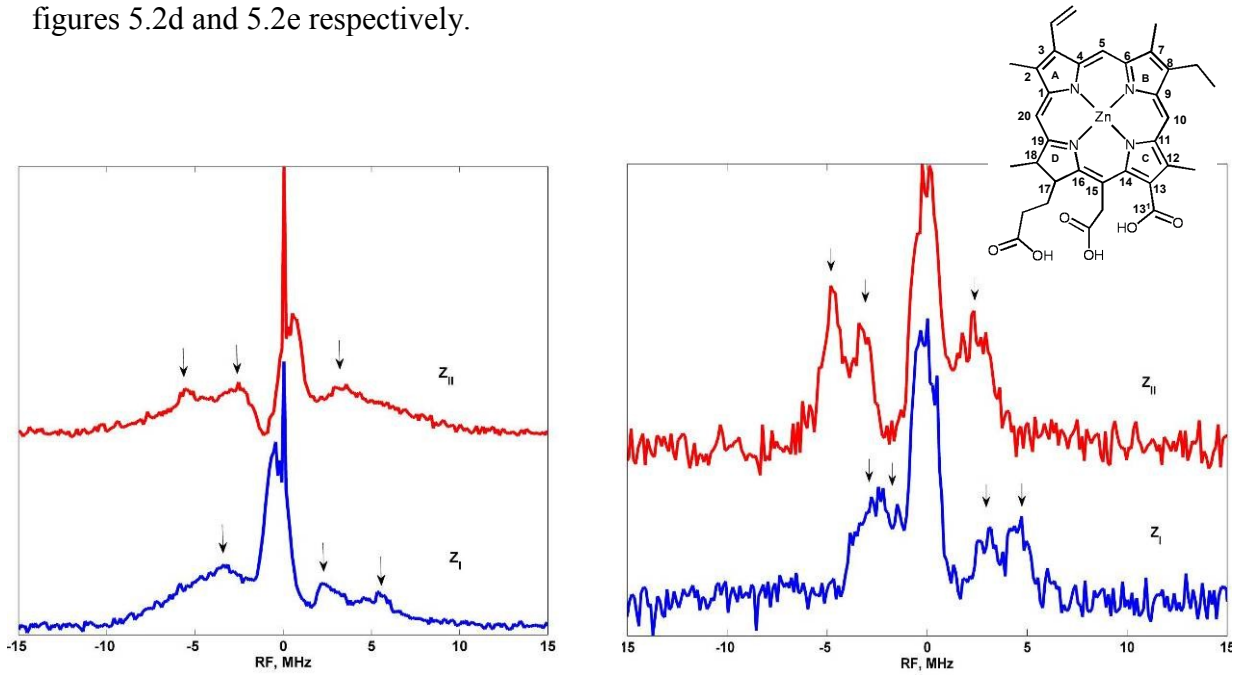

5.2d 5.2e

Figure 5.2d – Davies ENDOR spectra of Zn Chlorin in pyridine and 5.2e – Davies ENDOR spectra of Zn Chlorin-Mb. Preparative mw pulse: length 300 ns, t = 1 μs. Detection sequence: pulse sequence π/2 - π with pulse lengths 150 and 300 ns, τ = 440 ns. The detection pulses were applied 2 μs after the end of the radio frequency π pulse of 20 μs length. Microwave attenuation was 10 dB for the pyridine sample and 14 dB for the Mb sample. Temperature was 30 K and excitation was with laser at 532 nm and 10 mJ/pulse.

The spectra from single crystal like orientations are taken for comparison and one can observe that the position of hyperfine couplings do not differ but an increase in spectral resolution is seen when the model system is inserted into the myoglobin matrix. The hyperfine couplings have been assigned with the help of DFT calculations. They are summarised in table 5.4.

Position	Assigned hyperfine coupling, A_{iso} MHz
5-H	-5.6
7-CH_3	+3.3
18-CH_3	+0.5
2-CH_3	+4.8

Table 5.4 Assigned hyperfine couplings for various protons of Zn Chlorin in myoglobin

The large negative coupling, -5.6 MHz originates from the in plane *meso* hydrogen at position 5. The largest positive coupling that can be observed in this case is +4.8 MHz that originates from the free rotating methyl group at position 2. Several conditions were tried to obtain other hyperfine coupling, but none of them yielded any positive result.
ENDOR spectra from other canonical orientations of the triplet spectrum of zinc chlorin in horse heart myoglobin are shown in figure 5.2f.

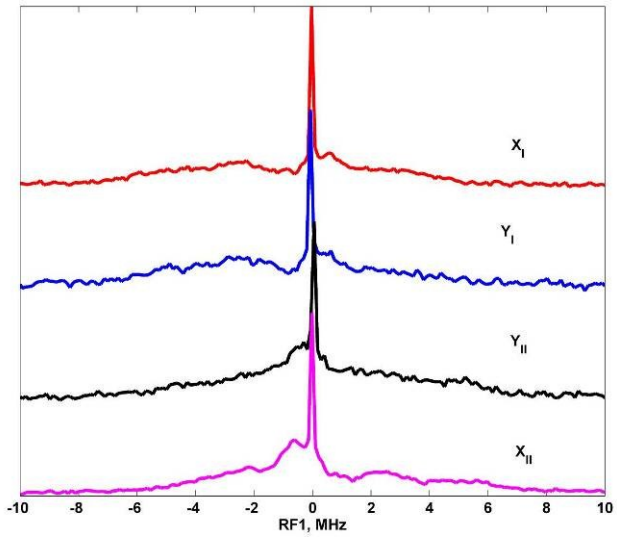

Figure 5.2f – Davies ENDOR spectra from other polarization positions in Zn Chlorin-Mb

5.3 Zinc chlorophyllide

5.3.1 Pulsed EPR

The EPR spectrum of zinc chlorophyllide in pyridine and in horse heart myoglobin matrix is shown in figures 5.3a and 5.3b, respectively. The EPR spectra of zinc chlorophyllide inside and outside myoglobin matrix have been obtained in similar experimental conditions. The microwave frequency was 33.383 ± 0.05 GHz and microwave attenuation was 8 dB. The length of the π/2 pulse was 40 ns and the π pulse was 80 ns. Laser power was 10 mJ/pulse at 532 nm and temperature was 30 K. The accumulation time was 30 minutes per spectra. The polarisation pattern is different from the previously described systems. It is EA EA EA and is similar to the polarisation pattern observed for Chl a in MTHF [94]. The ZFS parameters of the zinc chlorophyllide are also in close agreement with the values published for chlorophyll a [94].

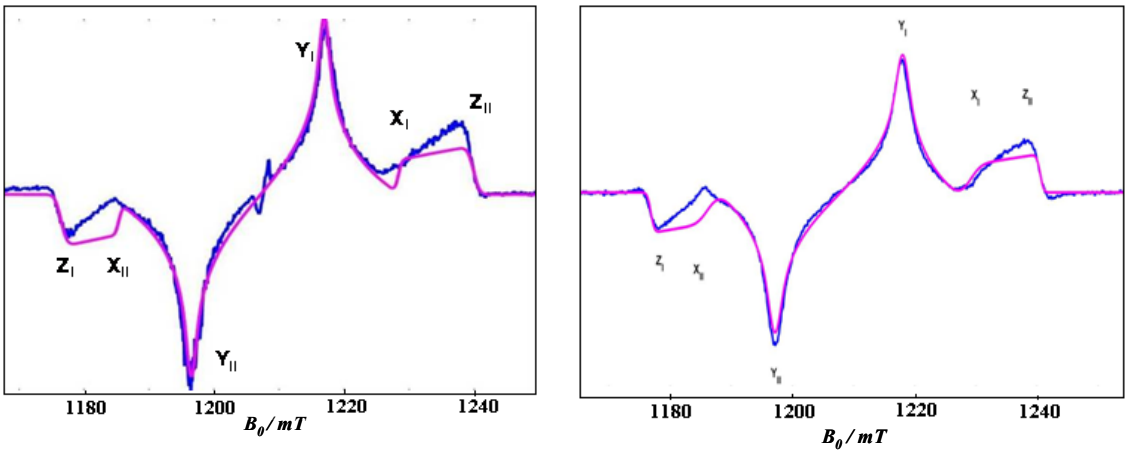

5.3a 5.3b

Figure 5.3a Pulsed EPR spectrum of Zn chlorophyllide in pyridine and 5.3b – Pulsed EPR spectrum of Zn chlorophyllide in myoglobin

Zn chl	|D| MHz	|E| MHz	g_x	g_y	g_z
Pyr	**890**	**105**	**2.0033**	**2.0032**	**2.0017**
Mb	**892**	**101**	**2.0034**	**2.0032**	**2.0015**
^{3}Chl a	**845**	**114**	**-**	**-**	**-**

Table 5.5 ZFS parameters of zinc chlorophyllide in pyridine and myoglobin.

5.3.2 Davies ENDOR

The ENDOR spectra of zinc chlorophyllide in pyridine and myoglobin in shown in figure 5.3c and 5.3d respectively. The ENDOR spectra of zinc chlorophyllide in other organic solvents could not be obtained easily owing to aggregation properties. The increasing radical signal causes decrease in triplet intensity and adds more noise to the spectrum with increase in accumulation time. However, the myoglobin bound cofactor yields spectra with better resolution and hyperfine coupling could be assigned with the help of DFT calculations

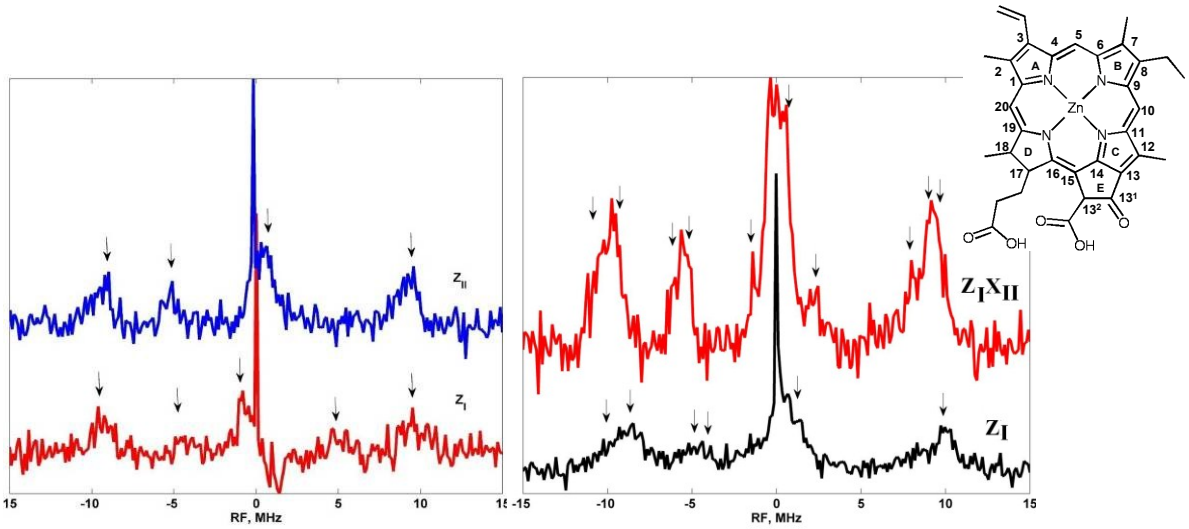

5.3c 5.3d

Figure 5.3c – Davies ENDOR spectra of zinc chlorophyllide in pyridine and 5.3d – Davies ENDOR spectra of zinc chlorophyllide in myoglobin. Preparative mw pulse: length 300 ns, t = 1 μs. Detection sequence: pulse sequence π/2 - π with pulse lengths 150 and 300 ns, τ = 440 ns. The detection pulses were applied 2 μs after the end of the radio frequency π pulse of 20 μs length. Microwave attenuation was 10 dB for the pyridine sample and 14 dB for the Mb sample. Temperature was 30 K and excitation was with laser at 532 nm and 10 mJ/pulse.

The spectra from the single crystal like position are displayed for comparison and it can be read from the spectrum that there are no changes in the hyperfine couplings. The ENDOR spectra from other canonical orientations from the Zn chlorophyllide-myoglobin EPR are shown in figure 5.3e. The prominent hyperfine couplings visible in the ENDOR spectra are tabulated in table 5.6. The large positive couplings of magnitude +9.4 MHz and +5.4 MHz arise from the methyl protons from position 12 and 2 respectively and the large negative couplings of magnitude -8.2 MHz, -7.4 MHz and -5.9 MHz arise from the in plane *meso* protons from positions 10, 20 and 5 respectively. A comparison with the hyperfine couplings of triplet chlorophyll a is done later in the discussions part of this chapter.

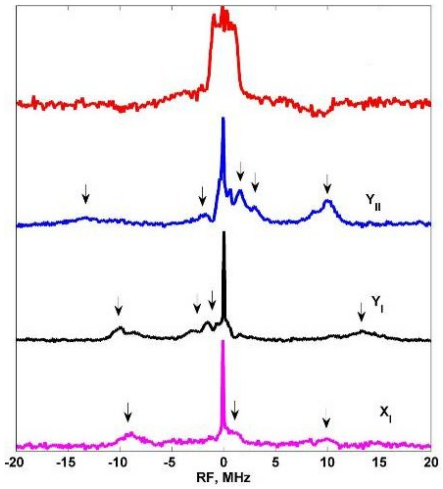

Figure 5.3e – Davies ENDOR spectra from other canionical orientations of zinc chlorophyllide in myoglobin (top most red spectrum corresponds to ENDOR from central field position)

Position	Assigned coupling, A_{iso} MHz
10-H, 20-H	**-8.2, -7.4**
5-H	**-5.9**
18-CH_3, 7-CH_3	**+0.5, +0.6**
2CH_3	**+5.4**
12-CH_3	**+9.4**

Table 5.6 Assigned hyperfine couplings of various protons of zinc chlorophyllide-Mb

5.4 Zinc pyrochlorophyllide

5.4.1 Pulsed EPR

The EPR spectra of zinc pyrochlorophyllide in pyridine and myoglobin are shown in figure 5.4a and 5.4b. It was very difficult to obtain an EPR spectrum of zinc pyrochlorophyllide in pyridine owing to its aggregation properties but it was possible to obtain a transient X-band spectrum. The transient spectrum could be simulated perfectly since the ESEEM relaxation effects are absent.

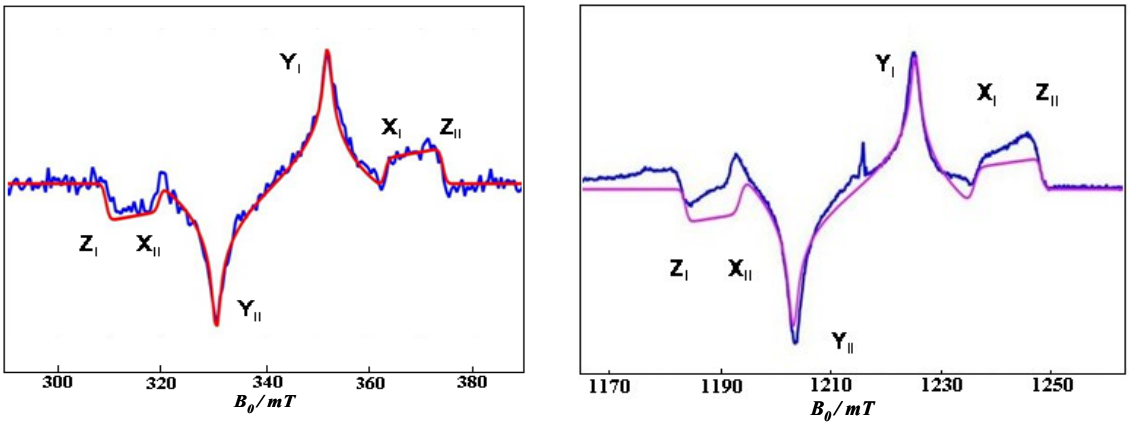

5.4a 5.4b

Figure 5.4a – Transient X band spectrum of zn pyrochlorophyllide in pyridine and 5.4b – Pulsed EPR spectrum of zn pyrochlorophyllide in myoglobin

The ZFS parameters are tabulated in table 5.6 and it can be seen that |D| and |E| values of zinc pyrochlorophyllide in pyridine and those of zinc chlorophyllide in myoglobin are in close agreement. The g-values are also similar indicating that there is no apparent change in electron configuration. The polarization pattern is the same as that of zinc chlorophyllide and chlorophyll a (EA EA EA).

ZnPyro	|D| MHz	|E| MHz	g_x	g_y	g_z
Pyr	**903**	**91**	**2.0041**	**2.0042**	**2.0025**
Mb	**905**	**94**	**2.0042**	**2.0039**	**2.0022**

Table 5.6 ZFS parameters of zinc pyrochlorophyllide in pyridine and myoglobin.

5.4.2 Davies ENDOR

Since an EPR spectrum of zinc pyrochlorophyllide in pyridine in a pulsed Q band spectrometer could not be obtained without much noise, ENDOR could not be measured on similar conditions. But we were able to obtain well resolved ENDOR spectra from zinc pyrochlorophyllide-myoglobin and the hyperfine couplings have been assigned with the help of DFT calculations. Figures 5.4c shows the ENDOR spectra of zinc pyrochlorophyllide-myoglobin from single crystal like position and 5.4d shows the spectra from other canonical positions.

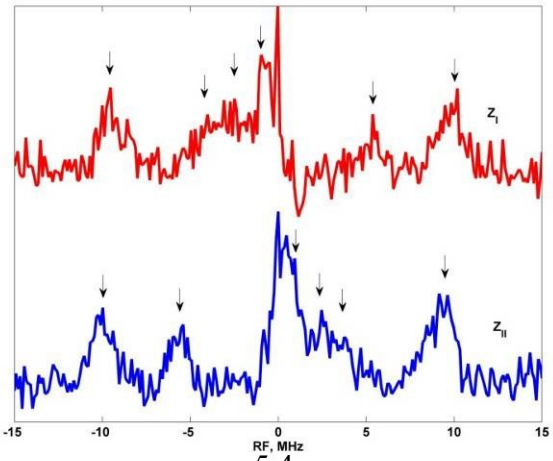

5.4c

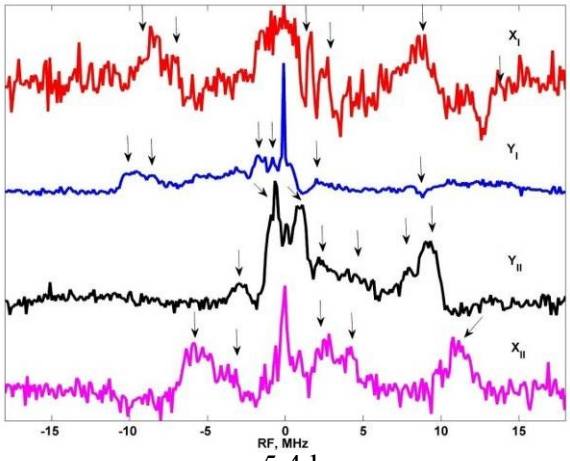

5.4d

Figure 5.4c – Davies ENDOR spectra from the single crystal like positions of zn pyrochlorophyllide-Mb EPR spectrum and 5.4d – Davies ENDOR spectra from other polarization positions of zinc pyrochlorophyllide-Mb. Preparative mw pulse: length 300 ns, t = 1 μs. Detection sequence: pulse sequence π/2 - π with pulse lengths 150 and 300 ns, τ = 440 ns. The detection pulses were applied 2 μs after the end of the radio frequency π pulse of 20 μs length. Microwave attenuation 14 dB. Temperature was 30 K and excitation was with laser at 532 nm and 10 mJ/pulse.

The hyperfine couplings are tabulated and displayed in table 5.7. The large positive couplings of magnitude +10.1MHz and +5.8MHz arise from methyl protons from position 12 and 2 respectively. The large negative couplings arise from the in plane *meso* protons. An extensive comparison between the hyperfine couplings of the various model systems with triplet chlorophyll a is done in the discussions part of this chapter.

Position	Assigned hyperfine coupling, A_{iso}, MHz
2-CH_3	**+5.8**
12-CH_3	**+10.1**
7-CH_3	**+0.7**
13^2-H	**-1.9**
5-H	**-6.3**
10-H	**-9.9**
20-H	**-10.1**

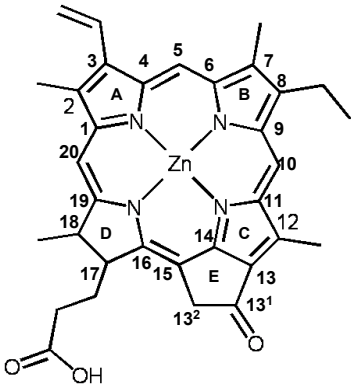

Table 5.7 Assigned hyperfine couplings of various protons of zinc pyrochlorophyllide in myoglobin

5.5 Electron spin density calculations on the triplet state of model systems

Electron density calculations were performed on the triplet states of the model systems in an attempt to understand the spin density distribution. Calculations were performed on the model systems with the central metal Zn coordinated to pyridine and to the proximal histidine residue of the myoglobin. But no difference in electron density distribution was seen on the pyridine or the histidine. Hence the results presented here are spin density calculation on the model systems without any additional coordination to the central metal Zn. Electron spin density calculations performed on triplet states of chlorophylls [95] and bacteriochlorophylls [96] are shown for comparison of results.

5.5.1 Zinc protoporphyrin IX

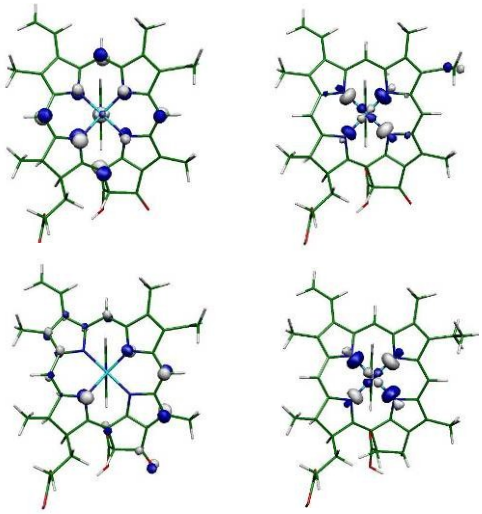

Figure 5.5 Representation of spin densities in the various orbitals of ZnPPIX. Top Left – HOMO-1, TOP RIGHT – HOMO, Bottom Left – LUMO, Bottom Right – LUMO+1

The HOMO-1 orbital of zinc protoporphyrin IX shows a symmetric electron density distribution with almost equal densities distributed over the meso protons, nitrogens and the central metal Zn. In contrast the HOMO orbital shows a much more localised electron density distribution with trace densities over the 8^{1} CH_2. However, the LUMO orbital shows an electron density distribution that is nearly consistent with observed ENDOR hyperfine couplings. The distribution is completely delocalized over the π bond electron conjugation of the porphyrin ring which explains the broad negative couplings from protons in position 5, 10, 15 and 20. The LUMO+1 orbital also show a much localised density distribution primarily around the 4 nitrogens in the porphyrin.

5.5.2 Zinc chlorophyllide

The HOMO-1 orbital of zinc chlorophyllide shows a very delocalized electron spin density distribution much similar to zinc protoporphyrin IX and similar to a_{2u} distribution as predicted by Gouterman. The HOMO orbital has a localized distribution primarily over the nitrogens and the central metal Zn and an umbrella like distribution can be seen over the nitrogens.

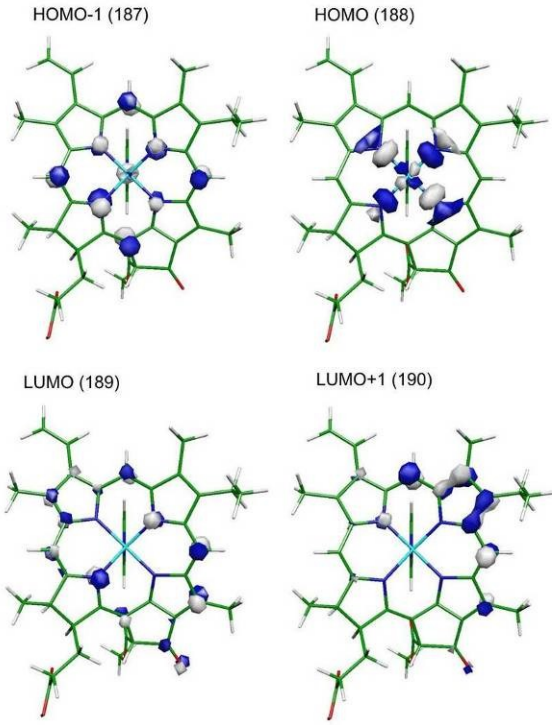

Figure 5.6 Electron spin density distribution in the various orbitals of zinc chlorophyllide

The LUMO orbital shows a delocalized distribution with spin densities over the meso protons and near the free rotating methyl groups at positions 2 and 12. The LUMO+1 orbital shows a highly localised distribution but only over the B ring of the porphyrin. The LUMO orbitals show no electron density over the zinc metal atom and the nitrogens also do not hold any electron density.

5.5.3 Zinc pyrochlorophyllide

The HOMO-1 orbital of zinc pyrochlorophyllide exhibits an asymmetric electron density distribution in contrast to the previously described systems. There is not an even distribution over the nitrogens but more favourable over the meso protons. The HOMO orbital shows symmetric delocalised distribution over the entire porphyrin π system.

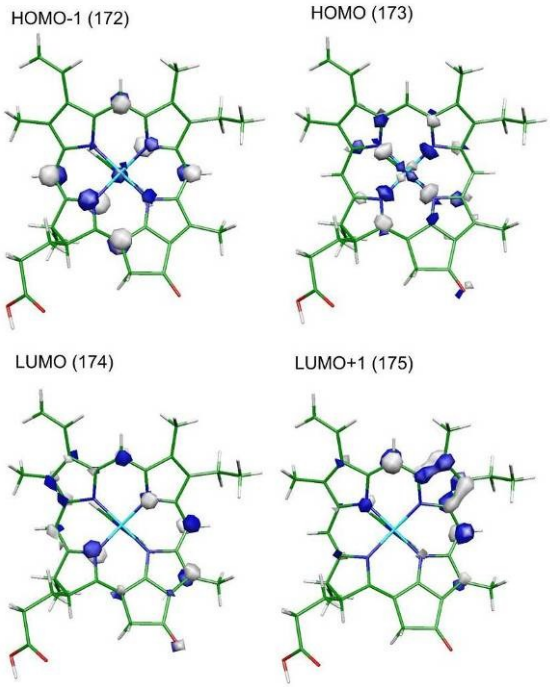

Figure 5.7 Electron spin density distribution in the various orbitals of zinc pyrochlorophyllide

The electron density distribution in the LUMO orbital is more localized on ring A and the meso protons which explain the prominent hyperfine couplings from meso protons and methyl group at position 2. The LUMO+1 orbital shows a localized electron density over ring B which is very similar to the zinc chlorophyllide system.

5.5.4 Zinc chlorin

Though the electron density distribution over the HOMO-1 orbital in zinc chlorin looks symmetric, the distribution is denser near the carboxylic acid groups due to its electron withdrawing effects. The electron density distribution in the HOMO and LUMO orbitals is delocalized and similar to the other model systems. LUMO+1 exhibits a much more localized distribution around the B ring of the porphyrin but there is some distribution around the D ring.

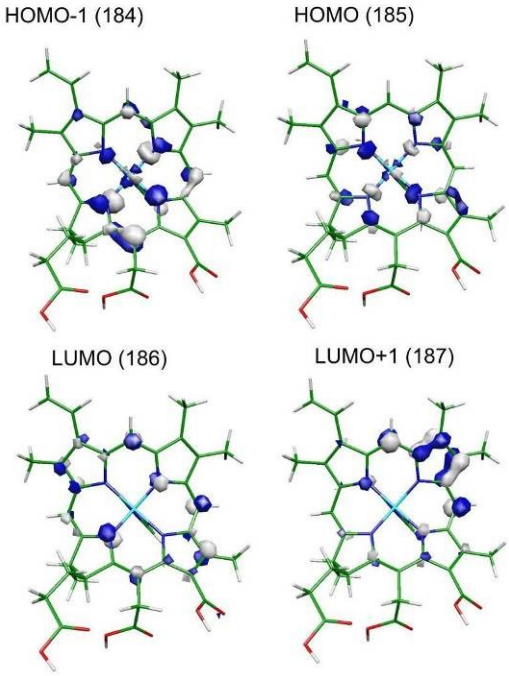

Figure 5.8 Electron spin density distribution in the various orbitals of zinc chlorin

5.6 Discussions

The four chlorophyll model systems have been analyzed by EPR and ENDOR spectroscopy in order to understand their electronic structure. From analyzing the polarization patterns and the |D| value, certain conclusions can be made. Insertion of the model systems into myoglobin does not affect the ZFS parameters or the g-values. This indicates that the triplet wave function is unaffected by the myoglobin matrix. However on analyzing the magnitude of |D|, it is observable that it increases when the model systems are inserted into myoglobin. Table 5.8 presents a comparison between the ZFS tensors of the various model systems compared with those of the photosystems and chlorophyll a [116]. From analyzing the polarization pattern, it is evident that all the model systems exhibit only the intersystem crossing mechanism of triplet formation. Native chlorophyll a and zinc substituted chlorophyll a also exhibit the same triplet formation mechanism. The polarization pattern AAAEEE and EAEAEA both correspond to the intersystem crossing mechanism.

System	|D| MHz	|E| MHz	g_x	g_y	g_z	Polarization pattern
ZnPPIX-Pyr	1054	212	-	-	-	AAAEEE
ZnPPIX-DMSO	1049	190	2.0040	2.0042	2.0024	AAAEEE
ZnPPIX-Mb	1081	216	2.0043	2.0042	2.0025	AAAEEE
Zn chlorophyllide - Pyr	890	105	2.0033	2.0032	2.0017	EAEAEA
Zn chlorophyllide - Mb	892	101	2.0034	2.0032	2.0015	EAEAEA
Zn pyrochlorophyllide - Pyr	903	91	2.0041	2.0042	2.0025	EAEAEA
Zn pyrochlorophyllide - Mb	905	94	2.0042	2.0039	2.0022	EAEAEA
Zn Chlorin - pyr	938	158	2.0045	2.0044	2.0027	AAAEEE
Zn Chlorin – aqueous	954	166	2.0043	2.0042	2.0025	AAAEEE
Zn Chlorin – Mb	974	147	2.0044	2.0043	2.0027	AAAEEE
$^3P_{680}$ [116]	863	126	-	-	-	AEEAAE
$^3P_{700}$ [117]	833	114	-	-	-	AEEAAE
Chl a – MTHF (monomeric)[94]	845	114	-	-	-	EAEAEA
^{3}Chl a [116]	854	123	2.0034	2.0038	2.0026	EAEAEA
Zn-Chl a [115]	918	126	-	-	-	EAEAEA

Table 5.8 Comparison of ZFS of various chlorophyll systems

However, the photosystems $^3P_{680}$ and $^3P_{700}$ exhibit only the radical pair mechanism of triplet formation which has the characteristic polarization pattern of AEEAAE. The photosystems are surrounded by acceptor molecules which make the radical pair mechanism possible. But the model systems and chlorophyll a (in organic solvents and myoglobin) are devoid of other acceptor molecules and hence can form triplet only via the ISC mechanism. The EPR spectra of the model systems in an organic solvent exhibit a radical signal which increases with time. This radical signal possibly originates from radical cations or anions that are formed between the model system and the solvent molecules because of their proximity in the π stacking distance. This radical signal does not interfere with the mechanism of triplet formation, but reduces the triplet intensity with time. This is one of the major factors affecting the ENDOR intensity of the model systems in an organic solvent.

The |D| value does not show much difference either. The largest deviation of the |D| value of the model systems when compared to the Zn-Chl a [115] is only 6% and the average deviation of the |D| value between organic solvent and myoglobin matrix of the various systems is only 2%. This shows that the triplet wave function is unaffected by the myoglobin matrix and it does not have any major influence on the ZFS tensors. The very small differences in |D| values compared to inside and outside myoglobin can be explained by minor variations in porphyrin ring conformation (puckering), elimination of the π stacking and changes in polarity of the environment. The g values are consistent with each other and do not provide further arguments to discuss at this stage.

Furthermore, pilot EPR experiments were done on the single crystals of ZnPPIX-Mb. The details of the crystallization and crystal structure have been described in detail in Chapter 4 of this thesis. The best and long crystals measuring 700 x 1 x 0.5 μm were selected for EPR measurements. Pulsed EPR measurements were carried on the single crystals frozen in liquid nitrogen with a cryo-protectant (3.5 M Ammonium sulphate with 30% Glycerol). The pulsed Q band spectra obtained from the various angles are shown in Figure 5.9a. The measurements were performed at 10 K and laser with wavelength 532 nm and 5 mJ/pulse was used to create the triplets. Microwave frequency was 34.001 GHz with variations of 0.05 during sample rotation and microwave attenuation was 2 dB. The π pulse was 20 ns and the π/2 pulse was 40 ns. The signal to noise ratio is weak but one can clearly see 4 signals and the displacement of the signals when the crystal is rotated. The final error in rotating the crystals was calculated to be around 10^0 which can be seen in Fig 5.9a. Each unit cell contains two proteins and two zinc protoporphyrin IX cofactors that are 180^0 to each other about the porphyrin axis as illustrated in Figure 5.9b. This explains the origin of the four signals that can be observed in the spectrum. However to analyze more in detail, it becomes essential to know the orientation of the crystal in the magnetic field. Owing to the very fine thickness of the crystals (0.5 μm), it was very difficult to determine the orientation of the crystal in the magnetic field. There are also visual limitations in observing the crystals when they are frozen owing to the use of cryo protectants which form an opaque layer.

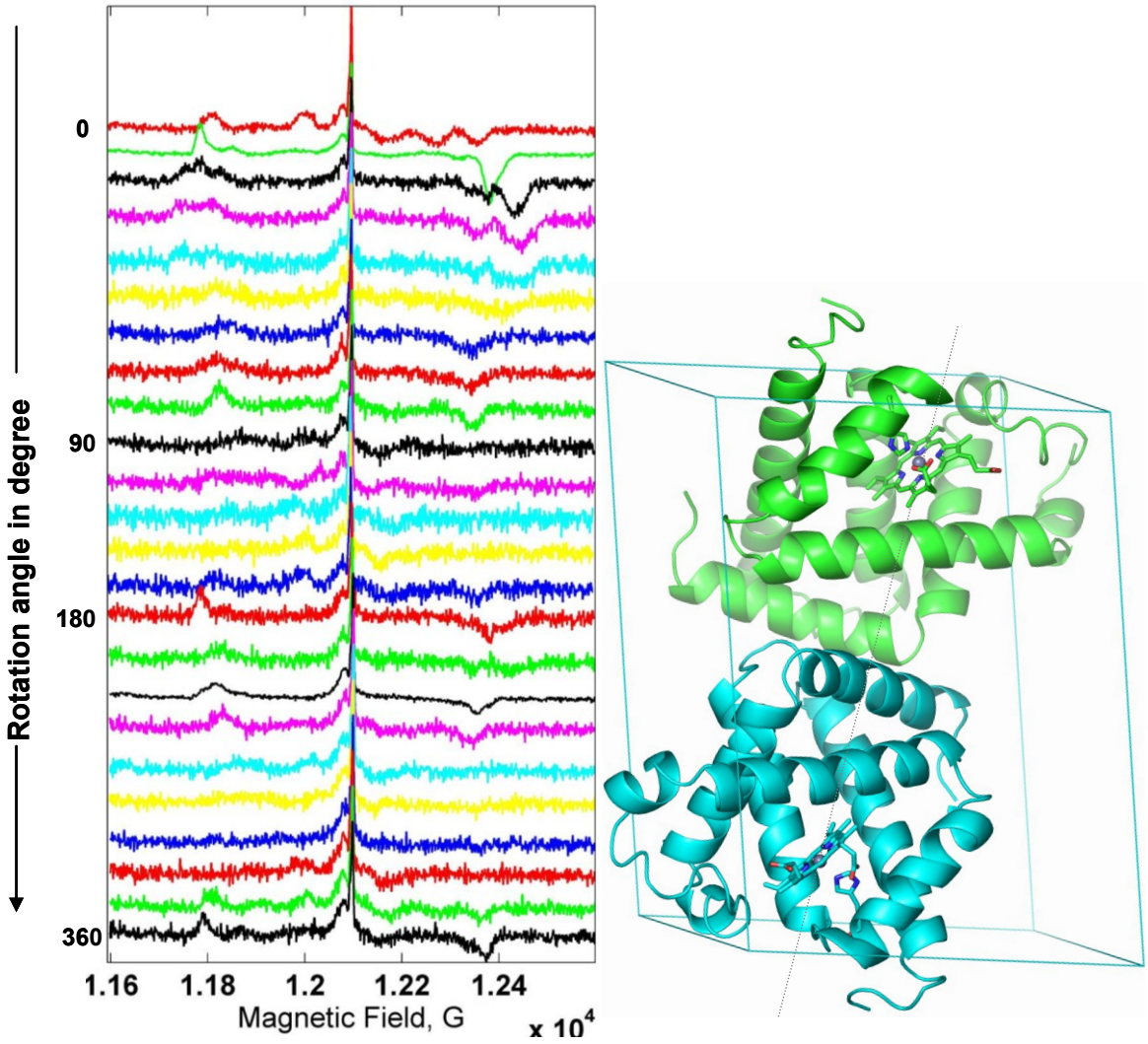

(a) (b)

Figure 5.9 (a) EPR spectra from various angles of ZnPPIX-Mb single crystal. (b) Illustration of the two possible porphyrin orientations in an unit cell of ZnPPIX-Mb single crystal

W band measurements were also tried using the crystals which were much smaller in size (100 x 1 x 0.5 μm). Fine capillaries, having a diameter similar to the width of the crystals were chosen and the crystals were inserted inside. In the case of Q band measurements, the crystal is first frozen and then inserted into the resonator. However, in the case of W band, this is not possible. The capillary is inserted into the resonator and the crystal is carefully positioned in the path of the laser which is a window of 1mm. The resonator is

now cooled down to 10 K. During this cooling process, there is expansion of the liquid surrounding the crystal which leads to its displacement from the laser window. Hence it is very difficult to position the micro crystals for W band measurements. Overcoming these limitations, we could still not observe strong signals from such small crystals.

ENDOR and spin density distribution:

In a simple molecular orbital (MO) picture, the neutral molecule comprises two electrons in the highest-occupied molecular-orbital (HOMO) followed by an empty lowest-unoccupied-molecular-orbital (LUMO). Studies of the radical cation allow investigation of the spin density distribution of the HOMO and studies of the radical anion give information about the LUMO. The triplet state would have an unpaired electron in both the HOMO and LUMO in this simple MO picture, and thus allows a simultaneous study of both orbitals.

The radical cation and anion of Chl *a* have been extensively studied by EPR and ENDOR spectroscopy. Isotropic proton hyperfine coupling constants have been measured and assigned to specific molecular positions, and the assignments were corroborated by quantum chemical calculations. Less information is available for the triplet state. The triplet state in the chlorophylls is formed after optical excitation *via* the intersystem crossing mechanism. Though chlorophyll triplet states have been investigated using EPR spectroscopy by many groups and polarization patterns and zero field splitting parameters have been obtained, no ENDOR study has been reported so far for triplet Chl model systems. The number of observed signals in the triplet ENDOR of the model systems is much smaller than that observed in the cation and anion radicals of chlorophylls. The difficulty with ENDOR experiments of the triplet state is related to the small spin polarization after intersystem crossing, which gives rise to weak signals [97, 101].

Atom position	Zinc chlorophyllide (Assigned hyperfine)	Zinc pyrochlorophyllide (Assigned hyperfine)	Zinc chlorin (Assigned hyperfine)	Chlorophyll a (Published hyperfine)	Zinc protoporphyrin IX (Assigned hyperfine)
5-H	-5.9	-6.3	-5.6	-2.3	-9.8
10-H	-8.2	-9.9	-	-5.8	-9.6
15-H	-	-	-	-	-10.3
20-H	-7.4	-10.1	-	-2.2	-10.5
2-CH3	+5.4	+5.8	+5.4	+4.2	-1.0
7-CH3	+0.6	+0.7	+3.3	+0.8	+3.3
12-CH3	+9.4	+10.1	-	+8.9	-0.7
18-CH3	+0.5	-	+0.5	-	+2.9
3”-CH2	-	-	-	+0.6	+0.4
17-H	-	-	-	+5.0	-
18-H	-	-	-	+5.9	-

Table 5.9 Comparison of hyperfine couplings from model systems inside myoglobin to that of Chlorophyll a [100] and with ZnPPIX-Mb. The hyperfine couplings are to be read in MHz

The prominent hyperfine couplings of the various systems have been tabulated for comparative reasons. It can be seen that the three systems, zinc chlorophyllide, zinc pyrochlorophyllide and zinc chlorin do not show much difference in the hyperfine coupling values for the same proton. The slight difference can be explained in terms of increase or decrease in electron density distribution near the proton in the triplet state of the atom. However, in comparison to these systems, there is visible change in the hyperfine coupling values of zinc protoporphyrin IX. The meso protons are in close agreement with each other. The 5-H of zinc protpporporphyin IX has a much higher value than the other systems. On comparing the hyperfine couplings of the reconstituted model systems with that of the native chlorophyll a, one can observe some similarities and some huge differences. The hyperfine couplings of H at positions 5 and 10 show nearly double the difference while a five fold increase in the hyperfine coupling of 10-H is visible in the model systems compared to that of chlorophyll a. The methyl protons at positions 2, 7 and 12 however fall in the same range. The hyperfine couplings of the methyl groups are lesser than expected due to its free rotation. The difference in the meso couplings could be the direct result of difference in electron density distribution.

The ENDOR spectra have been evaluated with the help of DFT calculations and electron density distribution in the various orbitals has been plotted. From the electron density distribution results it can be seen that the four model systems have similar distribution with subtle differences in the HOMO and LUMO orbitals. The chlorophyll derivatives: zinc chlorophyllide, zinc pyrochlorophyllide and zinc chlorin show much more similarity to each other and the zinc protoporphyrin (which resembles the native heme) stands out in its LUMO+1 orbital with respect to the others. In the chlorophyll model systems, the electron spin density in the LUMO+1 orbital is more localised around the ring B of the porphyrin whereas in zinc protoporphyrin IX, it is localised inside the porphyrin ring (around the nitrogens). The set of orbitals HOMO-1, HOMO, LUMO and LUMO+1 from the DFT calculations of zinc protoporphyrin IX, zinc chlorophyllide, zinc pyrochlorophyllide and zinc chlorin are shown in Figures 5.5, 5.6, 5.7 and 5.8. The orbitals are similar to the ones used by Gouterman to explain the spectroscopic properties of porphyrins. The HOMO-1 (a_{2u}) has a four fold symmetric axis perpendicular to the chlorin (tetrapyrrole) plane and large wave function coefficients are present at the nitrogen atoms and meso carbons. The HOMO is distributed evenly over the four pyrrole rings and is very similar to the a_{1u} Gouterman orbital. The spin density distribution has been compared to that of the bacteriochlorophyll a triplet and has been found similar [96]. It can be concluded that the triplet formation is not a simple HOMO → LUMO excitation but there is sufficient contribution from the HOMO-1 and LUMO+1 orbitals. The origin of the hyperfine couplings can be explained only when the HOMO-1 and LUMO+1 orbitals are taken into consideration.

A HOMO → LUMO excitation results in too little spin density at the *meso* carbons, and thereby too small hyperfine couplings for the methine protons. Upon inspection of the orbitals for the various model systems (see Fig. 5.5, 5.6, 5.7 and 5.8), the HOMO-1 orbital does have large wavefunction coefficients at the *meso* carbons. The energy difference between HOMO and HOMO-1 is only 4000 cm^{-1}, calculated from the UV/VIS spectrum. Since the energy gap is small and equivalent to a weak hydrogen bond of about 3 kcal/mol,[114] the HOMO-1 may actually significantly contribute to the triplet wavefunction, *e.g.*, through configurational mixing, bending of the chlorin macrocycle or fluctuations of the hydrogen bonding network.

At this stage it is also essential to discuss the conformation of the model system inside the myoglobin matrix. As how a coin can be inserted into a slot machine in two ways, the cofactors can also assume two conformations when they are inserted into the myoglobin matrix, each 180^0 to each other. However, extensive studies have been made on these conformational anomalies in the reconstituted myoglobin and it has been ascertained that the conformation of the cofactor is predominantly 90% in one single orientation and it is that orientation that will also be seen in the single crystal of the same specie [102]. Studies show that even after 30 minutes of reconstitution, the cofactors assume the one most favourable conformation. All EPR and ENDOR measurements on reconstituted myoglobin samples have been recorded only after at least 60 minutes after reconstitution. EPR and ENDOR measurements made immediately after reconstitution also do not yield any additional or different spectral information than those reported here. One can conclude that though there is inhomogeneity in the cofactor conformation it does not affect the EPR and ENDOR on frozen liquid samples. A detailed study on the conformation of artificial myoglobins have been published by S.F Andres and M.Z. Atassi [102]

5.7 Conclusion

In this work, zinc chlorophyll derivatives have been synthesised from chlorophyll a and along with zinc protoporphyrin IX, chosen to be model systems under investigation. They have been successfully inserted into myoglobin and their EPR and ENDOR spectra have been compared with themselves outside myoglobin and also with chlorophyll a.

1. Various zinc chlorophyll model systems have been synthesised and characterized using UV-Vis and NMR techniques. The zinc chlorophyllide compounds serve as the perfect model systems since the Zn is in its +2 oxidation state and does not interfere with the triplet signal.
2. The zinc model systems have been successfully inserted into myoglobin by replacing its native heme and the reconstituted myoglobin have been characterized by their UV-Vis absorption spectra.

3. EPR and ENDOR spectroscopy has been performed on the model systems in organic solvents and on the reconstituted myoglobin samples in an attempt to understand their triplet states.
4. Comparing the ZFS tensors of the model systems inside and outside myoglobin, it can be concluded that the myoglobin does not affect the triplet state of the model systems. The polarization pattern indicates that the triplet is formed via the intersystem crossing mechanism which is consistent with that of chlorophyll a and zinc chlorophyll a.
5. The myoglobin matrix isolates the chlorophyll model systems and prevents them from forming aggregates. Since the π stacking distance is reduced, the triplet originating from the reconstituted myoglobin is from the model system without any interference from organic solvents and aggregates.
6. There are no changes in the ENDOR hyperfine couplings when the model systems are measured inside and outside the myoglobin matrix. It is also evident that the resolution of the hyperfine couplings of the chlorophyll model systems inside the myoglobin matrix is much enhanced compared to its corresponding spectra in organic solvents.
7. From the electron density distribution calculations, it can be concluded that the triplet formation is not just a simple HOMO $\rightarrow$ LUMO process, but it also involves the participation of the HOMO-1 and the LUMO+1 orbitals.
8. The myoglobin matrix further serves as a protection against oxidation from external oxidants including atmospheric oxygen. The samples of reconstituted myoglobin can be handled under normal laboratory conditions and even when exposed to light, there is no decomposition or modification of the EPR-ENDOR signals. Samples have been purposely left to thaw over night and measurements were carried out. There was still no occurrence of radical signal or any other modification.
9. Further, electrochemical experiments carried out on reconstituted myoglobin samples also yielded no oxidised or reduced products. Even addition of moderators in an attempt to oxidise or reduce the chlorophyll model systems

inside the myoglobin matrix did not yield any results. The cofactors are shielded by the myoglobin matrix thus preventing any modification.

10. The crystallization of native and reconstituted myoglobin has been exclusively carried out in this work. Several myoglobins have been screened and reconstituted with chlorophyll model systems in an attempt to crystallize them. DLS studies have provided the right pH conditions to obtain crystals of native myoglobin which was then used to obtain the optimum conditions for crystallization of reconstituted myoglobin.
11. We have been successfully able to crystallize and reproduce crystals of zinc protoporphyrin IX in horse heart myoglobin. Crystals as large as 0.7mm were obtained and the crystal structure has been determined at a resolution of 1.8 Å. The unit cell is $P2_1$ which is consistent with the native horse heart myoglobin unit cell structure.
12. Pilot EPR experiments have been carried out on these crystals but due to very thin faces of the crystal, its orientation in the magnetic field could not be ascertained with accuracy. The origin of the EPR signals have been explained by the until cell structure. However to get more detailed information, larger and thicker crystals have to be grown and then subjected to EPR and ENDOR. These experiments are a successful stepping stone for further complicated work.
13. Overall it can be concluded that the myoglobin serves as a perfect host for studying the triplet properties of chlorophyll model systems and single crystals of reconstituted myoglobin can be obtained to accurately determine the orientation of the ZFS tensors.

REFERENCES

1. Barber J, Chapman DJ, Telfer A. 1987. Characterisation of a photosystem II reaction centre isolated from chloroplasts of Pisum sativum. FEBS Lett. 220:67-73

2. Nanba O, Satoh K. 1987. Isolation of a photosystem II reaction center consisting of D-1 and D-2 polypeptides and cytochrome b-559. Proc. Natl. Acad. Sci. USA. 84:109-12

3. Tang XS, Fushimi K, Satoh K. 1990. D1-D2 complex of the photosystem II reaction center from Spinach: Isolation and partial characterization. FEBS Lett. 273:257-60

4. Erickson JM, Rochaix JD. 1992. The molecular biology of photosystem II. In: The Photosystems: Structure, Function and Molecular Biology. J. Barber, Vol. 11, pp. 101-77. Amsterdam: Elsevier

5. Green BR, Pichersky E. 1994. Hypothesis for the evolution of three-helix Chl a/b and Chl a/c light-harvesting antenna proteins from two-helix and four-helix ancesters. Photosynth. Res. 39:149-162

6. Jansson S. 1994. The light-harvesting chlorophyll a/b-binding proteins. Biochim. Biophys. Acta 1184:1-19

7. Bricker TM. 1990. The structure and function of CPa-1 and CPa-2 in photosystem II. Photosynth. Res. 24:1-13

8. Bricker TM, Ghanotakis DF. 1996. Introduction to oxygen evolution and the oxygen-evolving complex. In Oxygenic Photosynthesis: The Light Reactions, eds. DR Ort, CF Yocum, pp. 113-36. Dordrecht: Kluwer Academic Publishers

9. Bassi R, Dainese P. 1992. A supramolecular light harvesting complex from chloroplast photosystem-II membranes. Eur. J. Biochem. 204:317-26

10. Bassi R, Hoyer-Hansen G, Barbato R, Giacometti GM, Simpson DJ. 1987. Chlorophyll-proteins of the photosystem II antenna systems. J. Biol. Chem. 262:13333-41

11. Bassi R, Wollman FA. 1991. The chlorophyll-a/b proteins of photosystem-II in Chlamydomonas reinhardtii isolation, characterization and immunological cross-reactivity to higher plant peptides. Planta 183:423-33

12. Rögner M, Boekema EJ, Barber J. 1996. How does photosystem 2 split water? The structural basis of efficient energy conversion. Trends Biochem. Sci. 21:44-49

13. Alfonso M, Montoya G, Cases R, Rodriguez R, Picorel R. 1994. Core antenna complexes, CP43 and CP47, of higher plant photosystem II. Spectral properties, pigment stoichiometry and amino acid composition. Biochemistry 33:10494-500

14. Bassi R, Pineau B, Dainese P, Marquardt J. 1993. Carotenoid-binding proteins of photosystem-II. Eur. J. Biochem. 212:297-303

15. Barbato R, Race HL, Friso G, Barber J. 1991a. Chlorophyll levels in the pigment binding proteins of photosystem II. FEBS Lett. 268:86-90

16. de Vitry C, Wollman FA, Delepelaire P. 1984. Function of the polypeptides of the photosystem II reaction center in Chlamydomonas. Localisation of the primary reactants. Biochim. Biophys. Acta 767:415-22

17. Tang XS, Satoh K. 1984. Characterization of a 47-kilodalton chlorophyll-binding polypeptide (CP-47) Isolated from a photosystem II core complex. Plant Cell Physiol. 25:935-45

18. Hankamer B, Morris E, Zheleva D, Barber J. 1995. Biochemical characterisation and structural analysis of monomeric and dimeric photosystem II core preparations. In Photosynthesis: from Light to Biosphere, ed. P Mathis, Vol. 3, pp. 365-68. The Netherlands: Kluwer Academic Publishers

19. Zheleva D, Znarmuchameaov S, Barber J. 1996b Isolation and characterization of monomeric and dimeric CP47-RC photosystem II complexes. In From Molecular Mechanisms to the Plant: An Integrated Approach. Plant Physiol. Biochem.10th FESPP Congress Proc. Florence, Italy: pp. 89

20. Goldbeck J.H (1987) Structure, Function and Organization of the photosystem I reaction center complex. Biochimica st Biophysica Acta, 895 167-204

21. Jordan P., Fromme P., Witt H.T., Klukas O., Saenger W., Krauss N. (2001) Three dimensional structure of cyanobacterial photosystem I at 2.5 Å resolution. Nature, 411, 909-917.

22. Fromme P., Schlodder E. and Jansson S. (2003) Structure and function of the antenna system in photosystem I. In: Green B.R. and Parson W.W. (eds) Light-harvesting antennas in photosynthesis. Advances in photosynthesis and respiration. Vol 13, 253-279, Publishers: Springer, Dordrecht

23. Brettel K. (1997) Electron transfer and arrangement of the redox cofactors in photosystem I. Biochimica et Biophysica Acta, 1318, 322-373

24. Brettel K., Leibl W. (2001) Electron transfer in photosystem I. Biochimica et Biophysica Acta, 1507, 1-15.

25. Setif P (2006) Electron transfer from the bound Iron-sulfur clusturs to Ferridoxin/flavodoxin: Kinetic and structural properties of Ferridoxin/flavodoxin reduction by photosystem I. In: Goldbeck JH (ed) Photosystem I: The light driven plastocyanin: Ferridoxin oxidoreductase. Advances in photosynthesis and respiration, vol 24, 439-454, Publishers: Springer, Dordrecht.

26. Adsorption analysis and chromatographic method. Application to the chemistry of chlorophyll, M Tswett - Ber. Deut. Botan. Ges, 1906

27. Jensen et al. Chlorophylls of photosynthetic bacteria. Biochimica et Biophysica Acta Volume 88, Issue 3, 29 November 1964, Pages 466-479

28. Govindjee (1999) Carotenoids in photosynthesis: A historical perspective. In: Frank H.A., Young A.J., Britton G., and Codgell R.J. (eds). The photochemistry of carotenoids. Advances in photosynthesis and respiration. Vol. 8, 1-19. Publishers: Springer, Dordrecht.

29. Cogdell R.J., Frank H.A. (1987) How carotenoids function in photosynthetic bacteria. Biochimica et Biophysica Acta, 895, 63-79.

30. Buckley C.E., Houghton J.A. (1976) Study of effects of near UV-radiation on pigmentation of blue-green alga *Gloeocapsa Alpicola*. Arch. Microbiology, 107, 93-97.

31. J. C. Kendrew, R. E. Dickerson, B. E. Strandberg, R. G. Hart, D. R. Davies, D. C.Phillips, and V. C. Shore. Structure of myoglobin: A three-dimensional Fourier synthesis at 2 Angstrom resolution. Nature, 185:422–427, 1960.

32. M. F. Perutz, M. G. Rossmann, A. F. Cullis, H. Muirhead, G . Will, and A. C. T. North. Structure of myoglobin: A three-dimensional fourier synthesis at 5.5 angstrom resolution, obtained by x-ray analysis. Nature, 185:416–422, 1960.

33. L. Stryer. Biochemistry. W. H. Freeman and Co., New York, 4th edition, 1995.

34. Jordi Cohen, Kwiseon Kim, Paul King, Michael Seibert, and Klaus Schulten. Finding gas diffusion pathways in proteins: Application to O2 and H2 transport in CpI [FeFe]- hydrogenase and the role of packing defects. Structure, 13:1321–1329, 2005.

35. A. V. Zatovskii, V. Lisy, and T. Yu. Tchesskaya. Effect of moisture content of globular proteins on the parameters of Mössbauer spectra. Optics and Spectroscopy, 84:201–206, 1998.

36. M. Brunori, D. Bourgeoisb, B.Vallonea, The structural dynamics of myoglobin. Journal of Structural Biology, Volume 147, Issue 3, September 2004, Pages 223-234

37. Biophysical Techniques in Photosynthesis, Amesz, J. and Hoff, A. J. (Eds.), Advances in Photosynthesis, Vol. 3, Govindjee (Series Ed.), Dordrecht, Kluwer Academic Publishers 1996

38. Lubitz, W., Electron Paramagnetic Resonance, A Specialist Periodical Report.Vol. 19, Gilbert, B. C., Davies, M., and Murphy, D., The Royal Society of Chemistry, 174-242 2004

39. Schweiger, A. and Jeschke, G., Principles of pulse electron paramagnetic resonance, New York, Oxford University Press 2001

40. Kevan, L. and Kispert, L. D., Electron Spin Double Resonance Spectroscopy, New York, John Wiley & Sons 1976

41. J.R. Durrant , L.B. Giorgi, J. Barber, D.R. Klug, G. Porter Characterisation of triplet states in isolated Photosystem II reaction centres: Oxygen quenching as a mechanism for photodamage. Biochimica et Biophysica Acta (BBA) – Bioenergetics Volume 1017, Issue 2, 1 June 1990, Pages 167-175

42. A.W Rutherford, D.R. Paterson, J.E. Mullet. A light-induced spin-polarized triplet detected by EPR in Photosystem II reaction centers. Biochimica et Biophysica Acta (BBA) - Bioenergetics Volume 635, Issue 2, 13 April 1981, Pages 205-214

43. Haim Levanon, Avigdor Scherz. EPR study of electron spin polarization in the photoexcited triplet state of chlorophyll a and b. Chemical Physics Letters Volume 31, Issue 1, 15 February 1975, Pages 119-124

44. John S. Leigh Jr, P.Leslie Dutton. Reaction center bacteriochlorophyll triplet states: Redox potential dependence and kinetics. Biochimica et Biophysica Acta (BBA) - Bioenergetics Volume 357, Issue 1, 25 July 1974, Pages 67-77

45. The chlorophylls. Edited by Vernon and Seely. (1966) Academic press Inc.

46. R.Willstatter and L. Forsen, Ann. Chem. 396, 180 (1913)

47. H. Fischer and H. Siebel, Ann. Chem. 499, 84 (1932)

48. H. Fischer and A. Stern. The chemistry of Pyrroles. Vol II. Part 2. Akad. Verlagsges, Leipzig, 1940.

49. Iriyama K. et al, J. Biochemistry, 76, 901-904

50. Fatima L. Canjura, Steven J. Schwartz, Separation of chlorophyll compounds and their polar derivatives by high-performance liquid chromatography. J. Agric. Food Chem., 1991, 39 (6), pp 1102–1105

51. Parriott D. (1993). A practical guide to HPLC detection. Acad. Pr., San Diego

52. Harper et. al. Comparison of Myoglobins from Harbor Seal, Porpoise, and Sperm Whale, , The Journal of Biological Chemistry, 243, 683-689.

53. Teale, F.W., J. Biochim. Biophys. Acta 1959, 35, 543.

54. Steven G. Boxer, Karen A. Wright Preparation and Properties of a Chlorophyllide-Apomyoglobin complex, , Journal of American Chemical Society, 101:22, 1979

55. Neese, F., Solomon, E. I. (1998) Calculation of zero-field splittings, g-values, and the relativistic nephelauxetic effect in transition metal complexes. Application to highspin ferric complexes, *Inorg. Chem., 37*, 6568-6582.

56. Neese, F. (2006) Importance of direct spin-spin coupling and spin-flip excitations for the zero-field splittings of transition metal complexes: A case study, *J. Am. Chem. Soc., 128*, 10213-10222.

57. Neese, F. ORCA – An *ab initio,* Density Functional and Semiempirical program package, Version 2.6, revision 63, 2008, Universität Bonn., 2008.

58. Ganyushin, D., Neese, F. (2006) First-principles calculations of zero-field splitting parameters, *J. Chem. Phys., 125*, 024103-

59. Schafer, A., Horn, H., Ahlrichs, R. (1992) Fully Optimized Contracted Gaussian-Basis Sets for Atoms Li to Kr, *J. Chem. Phys., 97*, 2571-2577.

60. Weigend, F., Haser, M. (1997) RI-MP2: first derivatives and global consistency, *Theor. Chem. Acc., 97*, 331-340.

61. Frisch, M. J.; Trucks, G. W.; Schlegel, H. B.; Scuseria, G. E.; Robb, M. A.;Cheeseman, J. R.; Montgomery, Jr. J. A.; Vreven, T.; Kudin, K. N.; Burant, J. C.; Millam, J. M.; Iyengar, S. S.; Tomasi, J.; Barone, V.; Mennucci, B.; Cossi, M.;Scalmani, G.; Rega, N.; Petersson, G. A.; Nakatsuji, H.; Hada, M.; Ehara, M.; Toyota, K.; Fukuda, R.; Hasegawa, J.; Ishida, M.; Nakajima, T.; Honda, Y.; Kitao, O.; Nakai, H.; Klene, M.; Li, X.; Knox, J. E.; Hratchian, H. P.; Cross, J. B.; Bakken, V.; Adamo, C.; Jaramillo, J.; Gomperts, R.; Stratmann, R. E.; Yazyev, O.; Austin, A. J.; Cammi, R.; Pomelli, C.; Ochterski, J. W.; Ayala, P. Y.; Morokuma, K.; Voth, G. A.; Salvador, P.; Dannenberg, J. J.; Zakrzewski, V. G.; Dapprich, S.; Daniels, A. D.; Strain, M. C.; Farkas, O.; Malick, D. K.; Rabuck, A. D.; Raghavachari, K.; Foresman, J. B.; Ortiz, J. V.; Cui, Q.; Baboul, A. G.; Clifford, S.; Cioslowski, J.; Stefanov, B. B.; Liu, G.; Liashenko, A.; Piskorz, P.; Komaromi, I.; Martin, R. L.; Fox, D. J.; Keith, T.; Al- Laham, M. A.; Peng, C. Y.; Nanayakkara, A.; Challacombe, M.; Gill, P. M. W.; Johnson, B.; Chen, W.; Wong, M. W.; Gonzalez, C.; Pople, J. A. Gaussian 03, Gaussian Inc., 2004.

62. Neese, F. (2003) Metal and ligand hyperfine couplings in transition metal complexes:The effect of spin-orbit coupling as studied by coupled perturbed Kohn-Sham theory, *J. Chem. Phys., 118*, 3939-3948.

63. MatlabTM, Natick, MA, The Mathworks, Inc., 2004

64. Atherton, N. M. *Principles of Electron Spin Resonance*; Ellis Horwood PTR Prentice Hall: New York,1993.

65. Berson, J. A. *The Chemistry of the Quinonoid Compounds, Vol. II*; Patai, S. R., Z., Ed.; John Wiley & Sons: New York, 1988, pp 482.

66. Hanna, M. *Quantum Mechanics in Chemistry*; Hanna, M. Quantum Mechanics in Chemistry; The Benjamin/Cummings Publishing Company, Inc.: Menlo Park, CA, 1981: Menlo Park, CA, 1981.

67. Bersohn, M.; Baird, J. C. *An Introduction to Electron Paramagnetic Resonance*; W. A. Benjamin, Inc.: New York, 1966.

68. Atherton, N. M. Principles of Electron Spin Resonance; Ellis Horwood Limited: 1993.

69. Abragam, A.; Bleaney, B. Electron Paramagnetic Resonance of Transition Ions; Dover Publication Inc: New York, 1970.

70. Schweiger, A.; Jeschke G. Priniciple of pulse electron paramagnetic resonance; Oxford University Press: New York, 2001.

71. Bencini, A.; Gatteschi, D. EPR of Exchange coupled systems; Springer-Verlag: 1990.

72. Pilbrow, J. R. Transition Ion Electron Paramagnetic Resonance; Oxford University Press: New York, 1990

73. Budil, D. E., Thurnauer, M. C. (1991) The Chlorophyll Triplet-State As A Probe of Structure and Function in Photosynthesis, Biochim. Biophys. Acta, 1057, 1-41.

74. Frank, H. A., Bolt, J. D., Costa, S. M. D. B., Sauer, K. (1980) Electron-Paramagnetic Resonance Detection of Carotenoid Triplet-States, J. Am. Chem. Soc., 102, 4893-4898.

75. Frank, H. A., Cogdell, R. J. (1996) Carotenoids in photosynthesis, Photochem. Photobiol., 63, 257-264.

76. Klein, G., Voltz, R. (1975) Formation and Decay of Superexcited States in Dense Organic-Matter Under High-Energy Radiation, Intern. J. Radiat. Phys. Chem., 7, 155- 174.

77. Klein, G. (1983) Production of Pairs of Singlet Excitons and Triplet Excitons in Anthracene-Crystals, Chem. Phys. Let., 97, 114-118.

78. Swenberg, C. E., Stacy, W. T. (1968) Bimolecular radiationless transitions in crystalline tetracene, Chem. Phys. Let., 2, 327-328.

79. Neese, F. (2006) Importance of direct spin-spin coupling and spin-flip excitations for the zero-field splittings of transition metal complexes: A case study, J. Am. Chem. Soc., 128, 10213-10222.

80. Thurnauer, M. C. (1979) ESR study of the photoexcited triplet state in photosynthetic bacteria, Rev. Chem. Int., 100, 197-231.

81. Lubitz, W., Lendzian, F., Bittl, R. (2002) Radicals, radical pairs and triplet states in photosynthesis, *Acc. Chem. Res., 35*, 313-320.

82. Lendzian, F., Bittl, R., Lubitz, W. (1998) Pulsed ENDOR of the photoexcited triplet states of bacteriochlorophyll a and of the primary donor P-865 in reaction centers of *Rhodobacter sphaeroides* R-26, Photosynth. Res., 55, 189-197.

83. Hore, P.J. Analysis of polarized EPR spectra. In Advanced EPR in biology and biochemistry; Hoff, A., Ed.;Elsevier: Amsterdam, 1990; pp 405-440.

84. Frank, H. A., Friesner, R., Nairn, J. A., Dismukes, G. C., Sauer, K. (1979) Orientation of the Primary Donor in Bacterial Photosynthesis, Biochim. Biophys. Acta, 547, 484-501.

85. Boris W. Batterman, Henderson Cole, Dynamical diffraction of X Ray by perfect crystrals, Rev. Mod. Phys. 36, 681–717 (1964)

86. The Structure of Haemoglobin. IV. Sign Determination by the Isomorphous Replacement Method, Proc. R. Soc. Lond. A 14 September 1954, vol. 225 no. 1162 287-307

87. W A Hendrickson et al .Crystal structure of core streptavidin determined from multiwavelength anomalous diffraction of synchrotron radiation, PNAS April 1, 1989 vol. 86 no. 7 2190-2194

88. Berne and Pecora, "Dynamic Light scattering" John Wiley, 1975

89. Pecora, R. Dynamic Light Scattering: Applications of Photon Correlation Spectroscopy, Plenum Press, 1985

90. Johnson, C.S. Jr. and Gabriel, D.A. Laser Light Scattering, Dover Publications, Inc., New York 1981

91. Hoffmann, B. M.; "Triplet-State Electron-Paramagnetic Resonance Studies of Zinc Porphyrins and Zinc-Substituted Hemoglobins and Myoglobins", J. Am. Chem. Soc., 1975, 97, 1688-1694.

92. H.Levanon and J.R. Norris, Chemical Reviews, 1978, Vol 78, No.3

93. F. C. Pennington, H. H. Strain, W. A. Svec, J. J. Katz *J. Am. Chem. Soc.*, 1964, 86, pp 1418–1426

94. D.E Budil, M.C. Thurnauer, Triplet state of Chl a in MTHF. The chlorophyll triplet state as a probe of structure and function in photosynthesis BBA 1057 (1991) 1-41

95. Wolfgang Lubitz, Pulse EPR and ENDOR studies of light-induced radicals and triplet states in photosystem II of oxygenic photosynthesis Phys. Chem. Chem. Phys., 2002, 4, 5539-5545

96. Alexander Marchanka, Maurice van Gastel, Wolfgang Lubitz, Spin Density Distribution of the Excited Triplet State of Bacteriochlorophylls. Pulsed ENDOR and DFT Studies, J. Phys. Chem. B 2009, 113, 6917–6927

97. Kinichi Obi and Takashi Imamura ,Time Resolved ESR of intersystem crossing and energy transfer process, Reviews of Chemical Intermediates, 7 (1986) 225-242, Elsevier Science Publishers.

98. Huber, M., Lendzian, F., Lubitz, W., Tränkle, E., Möbius, K., Wasielewski, M. R.; "ENDOR and TRIPLE Resonance in Solutions of the Chlorophyll-a and Bis(chlorophyll)cyclophane Radical Cations", Chem. Phys. Lett., 1986, 132, 467-473.

99. Hoff, A. J., Lendzian, F., Möbius, K., Lubitz, W.; "Proton and Nitrogen Electron Nuclear Double and Triple Resonance of the Chlorophyll-*a* Anion in Liquid Solution", Chem. Phys. Lett., 1982, 85, 3-8.

100. DiValentin, M., Kay, C. W. M., Giacometti, G., Möbius, K.; "A time-resolved electron nuclear double resonance study of the photoexcited triplet state of P680 in isolated reaction centers of photosystem II", Chem. Phys. Lett., 1996, 248, 434- 441.

101. V. Lawetz, G. Orlandi and W. Siebrand. Theory of intersystem crossing in aromatic hydrocarbons. J.Chem.Phy. Vol 56, 8 (1972)

102. S. F. Andres, M. Z. Atassi Conformational studies on modified proteins and peptides. Artificial myoglobins prepared with modified and metalloporphyrins, , Biochemistry, 1970, 9 (11), pp 2268–2

103. Porra R.J, et al, Biochimica et Biophysica Acta, 975, 384-394

104. Longuet-Higgins, H. C., Rector, C. W., Platt, J. R. (1950) Molecular Orbital Calculations on Porphine and Tetrahydroporphine, *J. Chem. Phys., 18*, 1174-1181.

105. Platt, J. Electronic structure and excitation of polyens and porphyrins. In *Radiation Biology*; Hollaender, A., Ed.;McGraw Hill: New York, 1956; pp 71-124.

106. Gouterman, M. (1959) Study of the Effects of Substitution on the Absorption Spectra of Porphin, *J. Chem. Phys., 30*, 1139-1161.

107. Gouterman, M. (1961) Spectra of Porphyrins, *J. Mol. Spectrosc., 6*, 138-163.

108. Carrington, A.; McLachlan, A.D. *Introduction to magnetic resonance;* Harper & Row; John Weatherhill Inc.: New York, Evanston, London, Tokyo, 1967.

109. McConnell, H. M., Chesnut, D. B. (1958) Theory of Isotropic Hyperfine Interactions in Pi-Electron Radicals, *J. Chem. Phys., 28*, 107-117.

110. Michael Kammel, Jan Kern, Wolfgang Lubitz , Robert Bittl. Photosystem II single crystals studied by transient EPR: the light-induced triplet

state..Biochimica et Biophysica Acta (BBA)-Bioenergetics, Volume 1605, Issues 1-3, 18 August 2003, Pages 47-54

111. Zouni A., Witt H.T., Kern J., Fromme P., Krauss N., Saenger W., Orth P. (2001) Crystal strructure of Photosystem II from Synechococcus elongatus at 3.8 A Resolution. Nature, 409, 739-743.

112. Guskov A., Kern J., Gabdulkhakov A., Broser M., Zouni A., Saenger W. (2009) Cyanobacterial Photosystem II at 2.9 A resolution and the role of quinones, lipids, channels and chloride. Nature Struct. And Molec. Biology, 16, 334-342.

113. Lindberg K., Vanngard T., Andereasson L.E. (1993) Studies of the slowly exchanging chloride in photosystem II of higher plants. Photosynth. Res., 38, 401-408.

114. Steiner, T. (2002) The hydrogen bond in the solid state, *Angew. Chem. Int. Ed., 41*, 48-76.

115. Levanon, H., Norris, J. R.; "Photoexcited Triplet-State and Photosynthesis", Chem. Rev., **1978**, 78, 185-198.

116. DiValentin, M., Kay, C. W. M., Giacometti, G., Möbius, K.; "A time-resolved electron nuclear double resonance study of the photoexcited triplet state of P680 in isolated reaction centers of photosystem II", Chem. Phys. Lett., **1996**, 248, 434-441.

117. Poluektov, O. G., Utschig, L. M., Schlesselman, S. L., Lakshmi, K. V., Brudvig, G. W., Kothe, G., Thurnauer, M. C.; "Electronic structure of the P-700 special pair from high-frequency electron paramagnetic resonance spectroscopy", J. Phys. Chem. B, **2002**, 106, 8911-8916.

118. Kamiya N. and Shen J.R. (2003) Crystal structure of Oxygen evolving photosystem II from *Thermosynechococcus vulcanus* at 3.7 Å resolution. PNAS, 100, 98-103.

119. Loll B., Kern J., Saenger W., Zouni A., Biesiadka J. (2005) Towards complete cofactor arrangement in the 3.0 Å resolution structure of photosystem II. Nature, 438, 1040-1044.